

**Titre:** Low-cost RF and microwave source design using substrate  
Title: integrated waveguide technique

**Auteur:** José Fernando Mojica  
Author:

**Date:** 2004

**Type:** Mémoire ou thèse / Dissertation or Thesis

**Référence:** Mojica, J. F. (2004). Low-cost RF and microwave source design using substrate  
Citation: integrated waveguide technique [Mémoire de maîtrise, École Polytechnique de  
Montréal]. PolyPublie. <https://publications.polymtl.ca/7502/>

 **Document en libre accès dans PolyPublie**  
Open Access document in PolyPublie

**URL de PolyPublie:** <https://publications.polymtl.ca/7502/>  
PolyPublie URL:

**Directeurs de  
recherche:** Ke Wu  
Advisors:

**Programme:** Non spécifié  
Program:

# NOTE TO USERS

This reproduction is the best copy available.

**UMI<sup>®</sup>**



**UNIVERSITÉ DE MONTRÉAL**

**LOW-COST RF AND MICROWAVE SOURCE DESIGN USING SUBSTRATE  
INTEGRATED WAVEGUIDE TECHNIQUE**

**JOSÉ FERNANDO MOJICA**

DÉPARTEMENT DE GÉNIE ÉLECTRIQUE  
ÉCOLE POLYTECHNIQUE DE MONTRÉAL

MÉMOIRE PRÉSENTÉ EN VUE DE L'OBTENTION  
DU DIPLÔME DE MAÎTRISE ÈS SCIENCES APPLIQUÉES  
(GÉNIE ÉLECTRIQUE)

JUIN 2004





Library and  
Archives Canada

Bibliothèque et  
Archives Canada

Published Heritage  
Branch

Direction du  
Patrimoine de l'édition

395 Wellington Street  
Ottawa ON K1A 0N4  
Canada

395, rue Wellington  
Ottawa ON K1A 0N4  
Canada

*Your file    Votre référence*

*ISBN: 0-612-97970-9*

*Our file    Notre référence*

*ISBN: 0-612-97970-9*

#### NOTICE:

The author has granted a non-exclusive license allowing Library and Archives Canada to reproduce, publish, archive, preserve, conserve, communicate to the public by telecommunication or on the Internet, loan, distribute and sell theses worldwide, for commercial or non-commercial purposes, in microform, paper, electronic and/or any other formats.

The author retains copyright ownership and moral rights in this thesis. Neither the thesis nor substantial extracts from it may be printed or otherwise reproduced without the author's permission.

#### AVIS:

L'auteur a accordé une licence non exclusive permettant à la Bibliothèque et Archives Canada de reproduire, publier, archiver, sauvegarder, conserver, transmettre au public par télécommunication ou par l'Internet, prêter, distribuer et vendre des thèses partout dans le monde, à des fins commerciales ou autres, sur support microforme, papier, électronique et/ou autres formats.

L'auteur conserve la propriété du droit d'auteur et des droits moraux qui protègent cette thèse. Ni la thèse ni des extraits substantiels de celle-ci ne doivent être imprimés ou autrement reproduits sans son autorisation.

---

In compliance with the Canadian Privacy Act some supporting forms may have been removed from this thesis.

Conformément à la loi canadienne sur la protection de la vie privée, quelques formulaires secondaires ont été enlevés de cette thèse.

While these forms may be included in the document page count, their removal does not represent any loss of content from the thesis.

Bien que ces formulaires aient inclus dans la pagination, il n'y aura aucun contenu manquant.

UNIVERSITÉ DE MONTRÉAL  
ÉCOLE POLYTECHNIQUE DE MONTRÉAL

Ce mémoire intitulé:

LOW-COST RF AND MICROWAVE SOURCE DESIGN USING SUBSTRATE  
INTEGRATED WAVEGUIDE TECHNIQUE

présenté par : MOJICA José Fernando

en vue de l'obtention du diplôme de : Maîtrise ès sciences appliquées

a été dûment accepté par le jury d'examen constitué de :

M. BOSSISIO Renato G., M.Sc.A., président

M. GHANNOUCHI Fadhel, Ph.D., membre

M. WU Ke, Ph.D., membre et directeur de recherche

## DEDICATION

To my father's memory, and  
Juliana and Shima for their love.

## ACKNOWLEDGEMENTS

I would like to express my deepest gratitude to my director Dr. Ke Wu for having accepted me as master student, for his support, and his guidance during this project. I would like to thank Dr. Iñigo Molina and Mr. Galo Nuño too for many helpful discussions.

I would also like to thank Mr. Jules Gauthier, Mr. Steve Dubé and Mr. Roch Brassard for their patience during the construction of the prototypes and their technical assistance, and Mr. René Archambault for his software support.

I would also like to thank to Ms. Emilia Moldovan and Mr. Serioja Tatu for their support and their friendship.

A special thanks is also extended to Mr. Simon Germain, Mr. Dominic Deslandes, Mr. Traian Antonescu, Mr. Yves Cassivi for many helpful discussions and suggestions, as well as to all researchers at POLY-GRAMES.

Finally, I would like to extend my gratitude to my wife and to my parents and sister for their endless love and moral support.

## ABSTRACT

The purpose of this research is to design a Ka-band low-cost microwave power source using Substrate Integrated Waveguide (SIW) components.

This thesis presents the theoretical and experimental study of an oscillator and a power combiner as part of the microwave power source. The oscillator is designed and constructed using, as an active device, a medium power commercial amplifier that provides the RF energy to the circuit. The passive device of the oscillator is built on the basis of a SIW resonant cavity to obtain a high Q factor.

Several SIW passive components have already been discussed in the literature; the beginning of this thesis includes the operating principle and basic characteristics of such devices. Then, for a better understanding of the properties and the difficulties in designing and constructing a SIW resonant cavity, two types of cavities (single cavity and dual cavity) are presented in detail.

Additionally, some theoretical aspects essential to the design of oscillators are discussed: the Van der Pol analysis of electrical oscillators, the resonant frequency, the oscillator stability and the temperature response.

The power combiner is constructed with the SIW scheme, thus allowing the system to reduce the loss inherent to the transition between components, and also to decrease the manufacturing cost. The analysis of the simulation and measurements presented in this work offers an insight about the performance of the power combiner; the advantages of using an inter-injection-locked topology to interconnect the oscillators and to provide an in-phase that improves the overall response become then clear.

To further explore the possibility of combining two or more oscillators we have studied the  $90^\circ$  Hybrid coupler and its flexibility to work as a power combiner.

A comparison between the T-junction power combiner and the  $90^\circ$  Hybrid combiner is presented, as well as design considerations and experimental results. The analysis shows an improvement in the performance of the power source by using the Hybrid combiner: while the phase noise was improved by 40 dB/Hz, the injection locking bandwidth went from 4 MHz in the T-junction power source to 8 MHz in the Hybrid power source.

## RÉSUMÉ

Le but de ce projet de recherche est de concevoir une source de puissance micro-onde, peu coûteuse, dans la bande de fréquence Ka en utilisant la technologie des guides d'ondes à substrat intégré (SIW).

Cette thèse détaille l'étude théorique et expérimentale de cette source de puissance composée d'un oscillateur et d'un combineur de puissance. L'oscillateur est conçu à partir d'un amplificateur commercial de puissance moyenne qui fournit l'énergie RF au circuit. La composante passive de l'oscillateur est obtenue à partir d'une cavité résonante SIW capable de fournir un facteur de qualité élevé.

Plusieurs composants passifs SIW ont déjà été étudiés dans la littérature; la première partie de ce rapport inclut une description du principe de fonctionnement et des caractéristiques de base de ces dispositifs. Puis, afin de donner un meilleur aperçu des techniques de réalisation des circuits SIW, deux cavités résonnantes SIW (cavité simple et cavité double) font l'objet d'une étude détaillée.

De plus, certains aspects théoriques relatifs à la conception des oscillateurs sont abordés : l'analyse de Van der Pol, la fréquence de résonance, la stabilité d'oscillation ainsi que l'étude en température.

Le combineur de puissance est aussi réalisé en technologie SIW, permettant de diminuer la perte inhérente aux transitions entre composants et de réduire le coût de fabrication. Les simulations et les mesures expérimentales donnent un aperçu des performances du combineur de puissance et illustrent clairement les avantages d'utiliser une topologie à verrouillage inter-injection (*inter-injection-locked topology*) pour connecter les oscillateurs et améliorer la réponse globale en fournissant un signal en phase.

Afin de combiner deux ou plusieurs oscillateurs de façon plus efficace ; nous avons étudié un coupleur hybride  $90^\circ$  et la possibilité de s'en servir comme combineur de puissance. Une étude comparative (portant aussi bien sur la conception que sur les résultats expérimentaux), entre le combineur de puissance de type jonction en T et le combineur hybride  $90^\circ$ , est présentée. Les résultats montrent une nette amélioration des performances avec le combineur hybride : tout en améliorant le bruit de phase de 40 dB/Hz, la largeur de bande d'injection de la source de puissance est passé de 4 MHz avec la jonction en T à 8 MHz avec la source d'énergie hybride.



## TABLE OF CONTENTS

DEDICATION.....	iv
AKNOWLEDGEMENTS.....	v
ABSTRACT.....	vi
RÉSUMÉ.....	viii
INTRODUCCTON.....	1
CHAPTER 1. SUBSTRATE INTEGRATED WAVEGUIDE TECHNIQUE (SIW)	3
1.1 Introduction.....	3
1.2 Fundamental theory on traditional waveguide.....	3
1.3 SIW historic development.....	7
1.4 SIW fundamental theory .....	8
1.5 Substrate considerations.....	9
1.6 Micro strip transition.....	10
1.7 Measurements .....	12
CHAPTER 2. MICROWAVE CAVITIES .....	13
2.1 Resonant frequency.....	14
2.2 Energy considerations in a resonant cavity.....	17
2.3 Q factor definition.....	19
2.4 Cavity design.....	22
2.4.1 Resonant frequency.....	22
2.4.2 Coupling factor.....	26
2.4.3 Q factor.....	31

2.5	Measurements and results .....	33
2.5.1	Single cavity resonator .....	33
2.5.2	Dual cavity resonator .....	36
CHAPTER 3. MICROWAVE OSCILLATOR.....		38
3.1	Fundamental theory.....	38
3.2	Active and passive devices considerations .....	40
3.3	Design Procedure .....	42
3.3.1	Measurement and results.....	47
3.4	Oscillator stability .....	48
3.4.1	Spurious oscillations .....	49
3.4.2	Frequency pushing .....	49
3.4.3	Temperature .....	49
3.4.4	Phase noise .....	54
3.5	Injection Locking .....	55
CHAPTER 4. POWER SOURCE .....		58
4.1	Fundamental theory.....	58
4.2	Power combiner using a T junction based on SIW technology .....	61
4.3	Power source design.....	63
4.3.1	Measurement results.....	64
4.3.2	Power combiner phase noise.....	67
4.3.3	Temperature performance .....	68
4.4	Coupling effects over power combiner performance.....	74

4.5	Power combiner using a 90° Hybrid coupler .....	77
4.5.1	The 90° Hybrid coupler as a combiner .....	77
4.5.2	Mathematical derivation.....	83
4.5.3	SIW Hybrid combiner design and simulations results.....	84
4.5.4	SIW Hybrid combiner measured results .....	86
4.5.5	Power source using the SIW Hybrid combiner.....	88
4.5.6	Measurements results .....	88
CONCLUSION .....		95

## TABLE OF TABLES

Table 1-1: Substrate specifications .....	9
Table 3-1: Temperature performance of the oscillator. ....	50
Table 4-1: T-junction Power combiner temperature performance.....	69
Table 4-2: Hybrid power source temperature performance. ....	93

## TABLE OF FIGURES

Figure 1-1: A typical waveguide.....	4
Figure 1-2: Rectangular waveguide .....	5
Figure 1-3: TE <sub>10</sub> field configurations ( <i>Source</i> : [8].).....	7
Figure 1-4: Configuration of the on-substrate integrated waveguide synthesized using metallized via-hole arrays. ( <i>Source</i> [19])......	8
Figure 1-5: Transition of microstrip line to rectangular waveguide on the same substrate. <i>Source</i> [8]......	10
Figure 1-6: Simulated results for a microstrip to SIW transition a) Insertion loss. b) Return loss.....	11
Figure 2-1: Resonant cavities from a waveguide.....	14
Figure 2-2: Rectangular cavity electric field pattern.....	17
Figure 2-3: Rectangular cavity with short circuit .....	23
Figure 2-4: Resonant cavity using SIW .....	24
Figure 2-5: Electric field inside a SIW resonant cavity.....	25
Figure 2-6: a) Plots of $S_{11}$ , $S_{13}$ , b) Electric and magnetic fields inside the cavity .....	25
Figure 2-7: Coupling probe.....	27
Figure 2-8: K inverter.....	29
Figure 2-9: J inverter.....	29
Figure 2-10: T equivalent.....	30
Figure 2-11: $\pi$ equivalent .....	30

Figure 2-12: Plot of $S_{11}$ to calculate the Q factor.....	32
Figure 2-13: SIW resonant cavity with coupling vias.....	34
Figure 2-14: Simulated and measured results a) $S_{11}$ , b) $S_{12}$ .....	35
Figure 2-15: Photo of the single cavity resonator .....	36
Figure 2-16: Dual cavity .....	36
Figure 2-17: $S_{11}$ performance of the dual cavity resonator .....	37
Figure 3-1: Amplifier Layout.....	41
Figure 3-2: Amplifier measured gain.....	41
Figure 3-3: Oscillator analysis using an open loop.....	44
Figure 3-4: Open loop simulation results.....	45
Figure 3-5: Oscillator layout with tuning stubs. ....	46
Figure 3-6: Measurements setup: a) General setup. b) Single oscillator on the test.....	47
Figure 3-7: RF Oscillator output.....	48
Figure 3-8: Temperature measurements setup .....	50
Figure 3-9: Frequency variation with temperature on a single oscillator .....	51
Figure 3-10: Temperature measurements results .....	53
Figure 3-11: Phase noise oscillator's performance .....	55
Figure 3-12: Phase noise performance using Injection locking.....	57
Figure 4-1: Different combining techniques ( <i>Source: [6]</i> ) .....	59
Figure 4-2: Power combiner using a T-junction structure .....	61

Figure 4-3: Insertion loss of the T power combiner. a) The inductive post diameter is 0.58 mm, and is located in the center of the T junction $(x,y)=(0,0)$ ; b) The inductive post diameter is 0.78 mm, and is located at $(x,y)=(0,9)$ .....	62
Figure 4-4: T junction power combiner S parameters. ....	63
Figure 4-5: Power source layout .....	63
Figure 4-6: Resonant frequency: a) Oscillator 1, b) Oscillator 2 .....	65
Figure 4-7: Output power combiner.....	66
Figure 4-8: Power source phase noise.....	67
Figure 4-9: Temperature set up for the power combiner .....	68
Figure 4-10: Frequency variation with temperature on the T-junction power combiner	70
Figure 4-11: Power combiner temperature measurements results. ....	72
Figure 4-12: Phase noise behavior with temperature variation.....	73
Figure 4-13: Power source without tuning.....	74
Figure 4-14: Adaptation of a 3-ports device .....	75
Figure 4-15: 90° Hybrid coupler. ....	77
Figure 4-16: 90° Hybrid power combiner.....	77
Figure 4-17: ADS schematic of the 90° Hybrid power combiner.....	79
Figure 4-18: 90° Hybrid power combiner simulation results .....	80
Figure 4-19: Power combiner efficiency of Hybrid-coupler combiner. <i>Source: [6]</i> .....	81
Figure 4-20: 90° Hybrid power combiner simulation results with 20° mismatch between oscillators. ....	82
Figure 4-21: Hybrid coupler incident and reflected waves.....	83

Figure 4-22: SIW Hybrid power combiner .....	84
Figure 4-23: SIW Hybrid combiner S parameters simulations results .....	85
Figure 4-24: SIW Hybrid combiner. ....	86
Figure 4-25: SIW Hybrid combiner isolation at ports 2 and 3.....	87
Figure 4-26: SIW Hybrid combiner measurements .....	87
Figure 4-27: Power source using the SIW Hybrid power combiner.....	88
Figure 4-28: Resonant frequency: a) Oscillator 1, b) Oscillator.....	89
Figure 4-29: Hybrid power source without injection locking.....	90
Figure 4-30: Signal cancellation at port 4. ....	91
Figure 4-31: Phase noise measurement without injection locking.....	92
Figure 4-32: Phase noise measurement comparison with and without injection locking.....	92
Figure 4-33: Frequency variation with temperature in the Hybrid power combiner .....	94



## INTRODUCTION

In the design of RF and microwave systems the need often arises for low cost and high power that a single device cannot supply. Substrate Integrated Circuits (SIC) technology [31] is a very promising scheme that offers low cost and easy fabrication, and allows the low-loss integration of planar and non-planar structures within the same substrate [8]. It is known that the output power of solid-state devices is limited; many power-combining approaches [17] were thus proposed. Such combining techniques can be classified into resonant combiners using a waveguide cavity that has been proved very successful for narrow band applications up to 300 GHz, and non-resonant combiners on the basis of couplers or circulators to combine the power.

As part of SIC, Substrate Integrated Waveguide (SIW) makes possible to replace the typical waveguide structures up to a certain point, with the advantage of reducing the circuit's size and the production cost. Chapter 1 reviews the important topics on waveguide components, and how we can replace them by their equivalent SIW components.

A power source is basically the combination of several oscillators; each of them consists of a passive component (in our case a SIW resonant cavity) and an active device (amplifier). The theory, design procedure, simulations, and measurements of the passive circuits are briefly explained in Chapter 2. Chapter 3 discusses the specifications and measurements of an amplifier, as well as the procedure to design an oscillator; we carry on a phase noise and temperature analysis in order to measure the oscillator performance.

Bringing together and synchronizing two or more oscillators with the same framework is not an easy task. The phase, amplitude and resonant frequency of the devices require special care. Achieving the best signal quality requires the use of an injection locking

scheme to synchronize the oscillators in the power combiner, whose construction is based on the T-junction power combiner [12]. An injection locking explanation is presented on chapter 3 and 4.

To improve the performance of the power source, the  $90^\circ$  Hybrid combiner will be studied (using simulations tools such as ADS and HFSS), and then used to build the power source. The theory and analysis on the power source are explained in Chapter 4.

The last section of the thesis contains the final conclusions as well as recommendations for future studies, all of which are based on the results presented throughout this work.

## **CHAPTER 1. SUBSTRATE INTEGRATED WAVEGUIDE TECHNIQUE (SIW)**

### **1.1 Introduction**

In today's Telecommunication world an especial consideration has been given to the development of new technologies to optimize the performance of a communication system. The main efforts are invested in minimizing the size and reducing the production cost, taking into account the trade off between good performance and low cost. At higher frequencies, the rectangular waveguide has been the riding horse to interconnecting devices and to creating different types of circuits, such as filters, resonant cavities, circulators, couplers, etc. Finding a new way to reduce the size, simplify the fabrication process and lower production cost has inspired several researchers to develop a technique that could replace the waveguide to some extent; namely, Substrate Integrated Waveguide could be the response to our needs.

### **1.2 Fundamental theory on traditional waveguide**

Waveguide is a structure that serves to guide the electromagnetic waves. A formal definition could be: a closed metal cylinder, filled with a dielectric, used to transport electromagnetic energy over short or long distances [7]. That structure is shown in Figure 1-1. When filled with low-loss dielectrics (such as air), waveguides typically exhibit lower losses than transmission lines, which makes them useful for transporting RF energy over relatively long distances.

Every type of waveguide has an infinite number of distinct electromagnetic field configurations that can exist inside of it. Each of these configurations is called a waveguide mode. The characteristics of these modes depend upon the cross-sectional

dimensions of the conducting cylinder, the type of dielectric material inside the waveguide, and the frequency of operation.

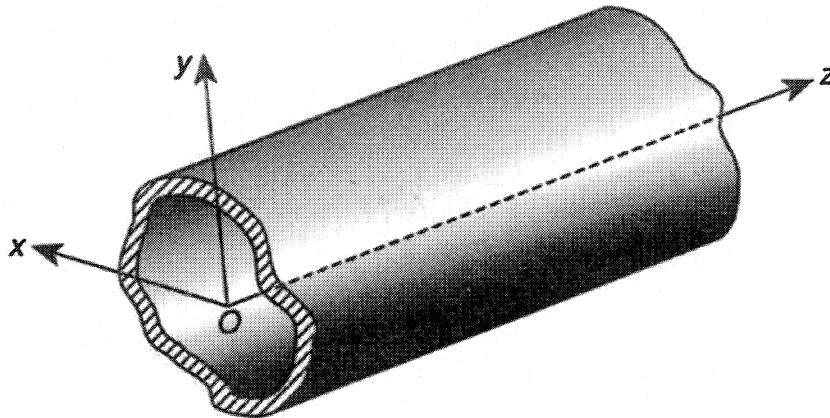


Figure 1-1: A typical waveguide

Waveguide modes are typically classed according to the nature of the electric and magnetic field components  $E_z$  and  $H_z$ . These components are called the longitudinal components of the fields. Several types of modes are possible in waveguides:

**TM modes** (Transverse-Magnetic): As the name implies, the magnetic field for this mode is transverse to the direction of propagation, therefore  $H_z = 0$ . This mode can exist in either a hollow pipe or open-wire system. Sometimes is called E mode.

**TE modes** (Transverse-Electric): The electric field of this mode is transverse to the direction of propagation, therefore  $E_z = 0$ . It also can exist in either a hollow pipe or open-wire system. Sometimes is called H mode.

**TEM modes** (Transverse Electric and Magnetic): This mode, generally encountered in transmission-line work, does not have an electric or magnetic field in the direction of propagation. This mode cannot exist in a hollow pipe with no center conductor, since it

lacks a current for transverse magnetic lines to link to, as required by Ampere's law. This mode is often called transmission line mode.

Waveguide modes are most easily determined by first computing the longitudinal field components,  $E_z$  and  $H_z$ , which can be supported by the waveguide. The transverse components (such as  $E_x$  and  $E_y$ ) can easily be found by taking spatial derivatives of the longitudinal fields [26].

When the waveguide properties are constant along the  $z$  axis,  $E_z$  and  $H_z$  vary in the longitudinal direction as  $E_z, H_z \propto \exp(j\omega t - \gamma z)$ , where  $\omega = 2\pi f$  is the radian frequency of operation and  $\gamma$  is a complex number of the form :

$$\gamma = \alpha + j\beta \quad (1.1)$$

The parameters  $\gamma$ ,  $\alpha$ , and  $\beta$  are called the propagation, attenuation, and phase constants, respectively, and  $j = \sqrt{-1}$

### 1.2.1 Rectangular waveguides

The rectangular waveguide is of considerable practical importance, being perhaps the most common of all different types of waveguides. Figure 1-2 shows a typical rectangular waveguide.

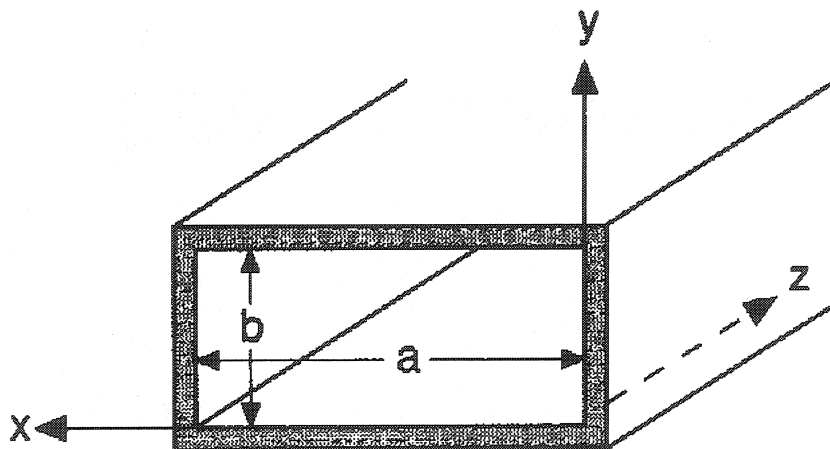


Figure 1-2: Rectangular waveguide

The conducting walls are formed such that the inner surfaces form a rectangular cross section, with dimensions  $a$  and  $b$  along the  $x$  and  $y$  coordinate axes, respectively. If the walls are perfectly conductive and the dielectric material is lossless, then the field components for the  $TE_{mn}$  modes are given by:

$$\begin{aligned}
 H'_z &= H_0 \cos \frac{m\pi x}{a} \cos \frac{n\pi y}{b} \\
 E'_z &= 0 \\
 H'_x &= \frac{\gamma m \pi H_0}{a k_c^2} \sin \frac{m\pi x}{a} \cos \frac{n\pi y}{b} \\
 H'_y &= \frac{\gamma n \pi H_0}{b k_c^2} \cos \frac{m\pi x}{a} \sin \frac{n\pi y}{b} \\
 E'_x &= \frac{j\omega \mu n \pi H_0}{b k_c^2} \cos \frac{m\pi x}{a} \sin \frac{n\pi y}{b} \\
 E'_y &= -\frac{j\omega \mu m \pi H_0}{a k_c^2} \sin \frac{m\pi x}{a} \cos \frac{n\pi y}{b}
 \end{aligned} \tag{1.2}$$

Where,

$$k_c^2 = \gamma^2 + \omega^2 \mu \epsilon = \left( \frac{m\pi}{a} \right)^2 + \left( \frac{n\pi}{b} \right)^2$$

The simplest and most frequently used mode in a rectangular waveguide is the  $TE_{10}$  mode. The field expressions on equation 1.2 can be simplified by letting  $m=1$  and  $n=0$ .

The result is:

$$\begin{aligned}
 E'_z &= E'_x = H'_y = 0 \\
 E'_y &= E_0 \sin \frac{\pi x}{a} \\
 H'_z &= j \frac{E_0}{\eta} \left( \frac{\lambda}{2a} \right) \cos \frac{\pi x}{a} \\
 H'_x &= -\frac{E_0}{Z_{0(TE)}} \sin \frac{\pi x}{a}
 \end{aligned} \tag{1.3}$$

This mode has a cut-off frequency given by:

$$f_{c_{10}} = \frac{1}{2a\sqrt{\mu\epsilon}} = \frac{c}{2a} \quad (1.4)$$

Where  $c$  is the speed of light in the dielectric media.

The field configurations for the TE<sub>10</sub> (dominant) mode of a rectangular waveguide is shown in Figure 1-3, where the solid lines are E and the dashed lines are H.

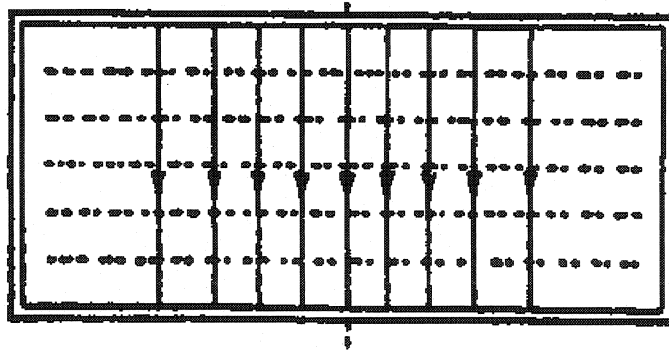


Figure 1-3: TE<sub>10</sub> field configurations (*Source*: [8].)

### 1.3 SIW historic development

Basically, SIW is a waveguide built on the same substrate of the active components and the whole system, reducing the losses due to transitions, and providing an easy way to construct the circuit. Pilote, Flanik and Zaki were the first researchers that referred to the idea of replacing the waveguide walls for a series of metallic vias through the substrate to achieve the same effect of metallic walls [23] and their original work was oriented to the resonant cavity problems. In [29] the authors show the results of passive circuits using SIW. Our research center has extensively used this technique and proposed new solutions and structures that can be built using SIW [8, 9, and 10].

## 1.4 SIW fundamental theory

As previously mentioned, the SIW is a structure that replaces the metallic walls of a rectangular waveguide for a row of via holes that will act as an electric wall from the RF perspective.

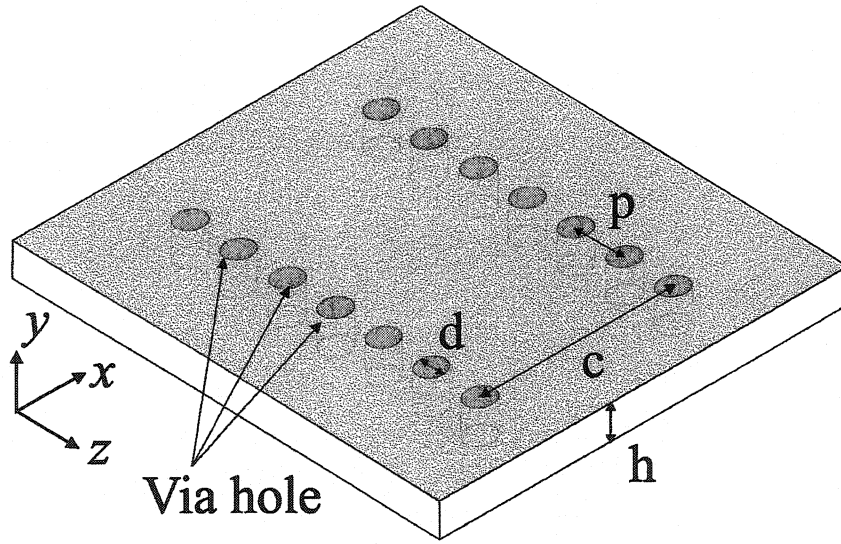


Figure 1-4: Configuration of the on-substrate integrated waveguide synthesized using metallized via-hole arrays. (Source [19])

As explained on [8], obtaining a structure model requires simulating two waveguides of different lengths using HFSS [33]; by doing so the propagation constant is calculated using

$$\beta_{SIW} = \frac{\angle S_{21}^{L2} - \angle S_{21}^{L1}}{L_1 - L_2} \quad (1.5)$$

Once the propagation constant  $\beta_{SIW}$  is obtained, it is possible to calculate the equivalent length using

$$a_{eqv} = \frac{\pi}{\sqrt{w^2 \mu_0 \epsilon_0 \epsilon_r - \beta_{SIW}^2}} \quad (1.6)$$



Figure 1-4 gives an overview of how SIW looks like. As it was shown in [4], the radiation losses of SIW structures are negligible if the via diameter is less than one fifth of the considered wavelength, and the distance between via holes is less than twice the hole diameter. If the conditions presented in Eq. 1.7 are met, the SIW behaves as the rectangular waveguide.

$$\begin{aligned} d &< \lambda_g / 5 \\ p &\leq 2d \end{aligned} \quad (1.7)$$

The via hole diameter has been limited by the minimum diameter of the drill, which is 0.78 mm, so the largest separation between holes could be of 1.56 mm, according to [8].

## 1.5 Substrate considerations

We have chosen the substrate RT / Duroid ® 6002 with a 0.254 mm thickness, a dielectric constant of 2.94 and a dissipation factor of 0.0012. Due to such thickness, it is more suitable to use microstrip lines than coplanar waveguides in order to achieve a characteristic impedance of 50 ohms. For example, at 24.2 GHz, the line width should be equal to 0.63 mm.

RT / Duroid ® 6002	Typical Values (10GHz / 23°)
Dielectric constant	2.94 ±0.04
Dissipation factor	0.0012
Magnetic constant	1
Coefficient of thermal expansion in X and Y	16 ppm/°C
Coefficient of thermal expansion in Z	24 ppm/°C
Thickness	0.254 mm

Table 1-1: Substrate specifications

Using this substrate ensure that the dimensions of our circuit will be made according to the manufacturing resources available in our lab.

Table 1-1 summarizes some of the most relevant specifications of the substrate.

## 1.6 Micro strip transition

The SIW to microstrip transition is the most common method to perform the measurements and interconnect our structure to the rest of the PCB. The development of this particular transition was made on [8]. This paper also points out that the large bandwidth is one of the advantages of the transition.

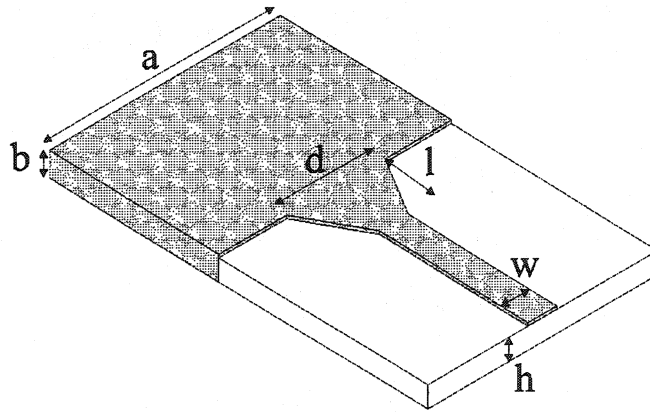
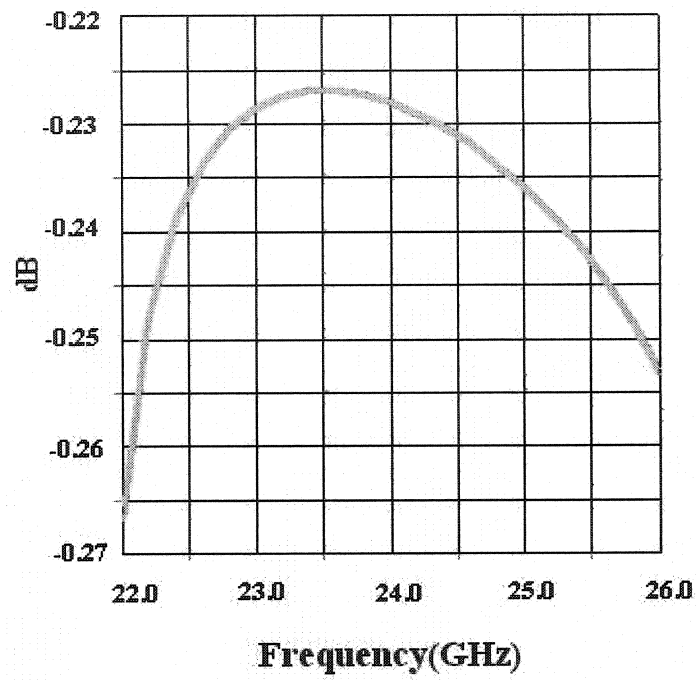
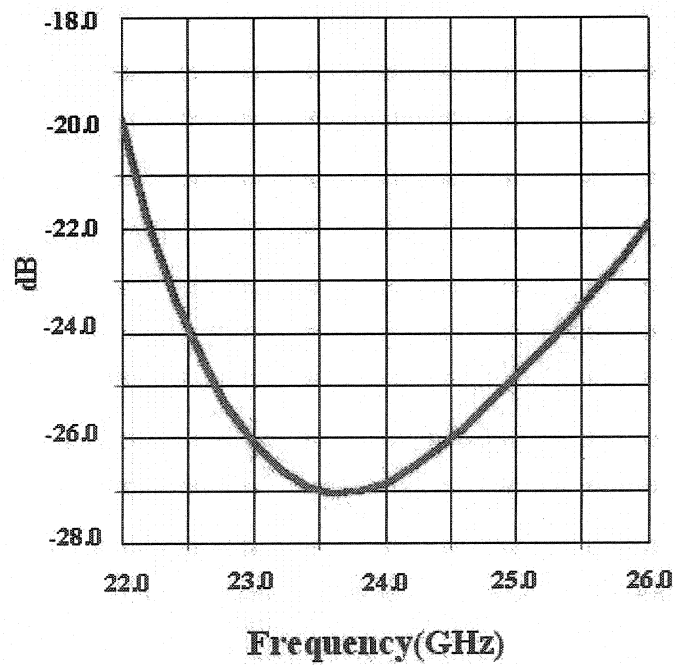


Figure 1-5: Transition of microstrip line to rectangular waveguide on the same substrate. Source [8].

We can optimize the transition by choosing the length  $l$  and width  $d$  according to the frequency; in this case, at 24.2 GHz,  $l$  is roughly a quarter of the wavelength, and  $d$  is obtained using the characteristic impedance of the SIW. An insertion loss better than -0.3 db and a return loss of -25dB are obtained thanks to the optimization process using the HFSS simulator. Figure 1-6 shows the simulated S parameters of the SIW to microstrip transition.



a)



b)

Figure 1-6: Simulated results for a microstrip to SIW transition a) Insertion loss. b) Return loss

## 1.7 Measurements

The HP 8510 network analyzer was used to perform measurements of the circuit; it is worth noting that the system should be calibrated in order to make error-corrected measurements in non-coaxial transmission media. This calibration has been based on a THRU-REFLECT-LINE method, as described in [32].

The lengths of the lines are:

- THRU = 32.25 mm
- REFLECT = 16.13 mm
- LINE = 34.03 mm

These lengths fulfill both the phase (a LINE insertion phase difference between 20 and 160 degrees with respect to the THRU) and length requirements (greater than two wavelengths) of this method in the amplifier-working band (17-40GHz).

## CHAPTER 2. MICROWAVE CAVITIES

This chapter will discuss the theory of microwave cavities and resonant frequencies. It will also explain how the quality factor of a cavity ( $Q$ ) is obtained, and finally, it will present the results of this research on the Substrate Integrated Waveguide.

### Fundamental theory of resonant cavities

It is possible to obtain inductive and capacitive effects at low frequencies using transmission lines. The same result can be obtained in microwave frequencies by introducing pieces of wave-guide that are enclosed by metallic walls. These metallic boxes, almost hermetic, are electromagnetic cavities. Inside the cavities, the electromagnetic energy exists at some particular frequencies, called resonant frequencies. Like a shortcut line or stub, the resonant cavity is a trap for stationary waves.

The geometric form of the cavity may vary, but what matters in most cases is the length, which has to be of a wavelength or a multiple of it. Since the parallelepiped rectangle and the cylindrical form are easy to construct, these are the most used shapes for cavities [27].

Generally speaking, cavities can be filled partially or totally with several dielectric materials, it all depends on the performance and application in a particular case. The internal walls of the cavities are reflective and with low losses, and even though the walls are metallic in most cases, they can also be covered with a specific dielectric material in order to obtain desired properties and effects.

To simplify the analysis of resonant cavities an ideal cavity will be assumed: walls are perfect conductors (zero electrical and magnetic losses), the cavity is hermetic (no leakage), and the filling is of a perfect dielectric material.

Electromagnetic oscillations inside the ideal cavity will also be assumed; since the cavity has perfect conditions, losses are inexistent and, therefore, perpetual oscillations will be present. Those oscillations can be considered as the result of the superposition of an infinite number of harmonic oscillations.

Under the previous conditions Maxwell equations are used to find all the oscillations frequencies (resonant frequencies), and to express the electromagnetic field and electromagnetic energy.

## 2.1 Resonant frequency

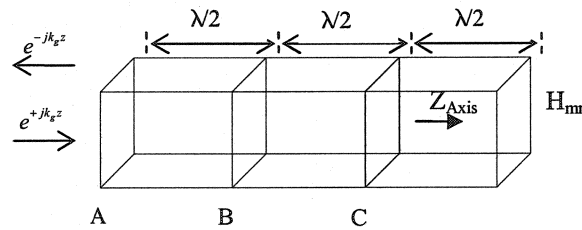


Figure 2-1: Resonant cavities from a waveguide

It will be assumed an H wave in an infinite waveguide. We short-cut the waveguide in a specific position A, with a metallic wall (perfect conductor). The electric and magnetic fields will then be reflected on the wall, with a reflection coefficient,  $\Gamma = \pm 1$ . This means that the waveguide has been converted into a stationary wave trap.

At the reference plans in Figure 2-1 there is a distance  $\lambda_g/2$  in between A, B and C, at which the transversal electric field is zero. Therefore, adding a second metallic wall at position B or C will leave the oscillations unchanged because the boundary conditions are still satisfied.

In the case of an E wave on the waveguide, the electric modes have to be considered as cut off points. The electric field is longitudinal in this case; in other words, at points A, B or C the electric field is perpendicular to the metallic wall. As a result, there is no need to impose a boundary condition along the cavity. Therefore, it is possible to obtain a cavity with  $E_{mn0}$  oscillating mode. The  $H_{mn}$  modes at the cut off point have an E field transverse component, which means it is essential to maintain the cavity length to preserve the boundary conditions.

Having explained how to build a resonant cavity, the resonant frequency will now be discussed. Figure 2-1 shows an incident wave with  $H_{mn}$  or  $E_{mn}$  modes. While the wave propagates in a Z direction with a propagation factor equals to  $e^{-jk_g z}$ , the reflected wave's propagation factor is  $e^{+jk_g z}$ . The reflection coefficient  $\Gamma = \pm 1$ : It is +1 for the electric longitudinal and magnetic transversal components, and -1 for the electric transversal and magnetic longitudinal components.

By using the Method of Reflection the resultant wave will be given by the factor  $(e^{-jk_g z} \pm e^{+jk_g z})$ ;  $2 \cos k_g z$  or  $-2j \sin k_g z$ . Generally speaking, a *sin* or *cos* factor tells us about the existence of stationary waves in a waveguide or a cavity.

It is known that:

$$k_g = 2\pi / \lambda_g \quad (2.1.1)$$

$$\lambda_g = \frac{2l}{p}$$

With  $k_g l = p\pi$ , and  $p = 1, 2, 3, 4, \dots$

Now is possible to find the values of  $\lambda_c$  and  $\lambda_g$ , and by doing so the value of  $\lambda$  is obtained by the following equation:

$$\frac{1}{\lambda} = \left( \frac{1}{\lambda_c^2} \right) + \left( \frac{1}{\lambda_g^2} \right) \quad (2.1.2)$$

with :

$$f = \frac{v}{\lambda} = \frac{1}{\lambda \sqrt{\epsilon_0 \epsilon \mu_0 \mu}}, \lambda \text{ in a free space.} \quad (2.1.3)$$

By using equations 2.1.1 and 2.1.2, it is possible to find an expression that allows for the calculation of the wave length of the possible oscillations in a certain cavity:

$$\lambda_{mnp} = \left[ \left( \frac{1}{\lambda_c^2} \right) + \left( \frac{P}{2L} \right)^2 \right]^{-1/2} \quad (2.1.4)$$

Where  $\lambda_{mnp}$  is medium independent, and not related to  $(\epsilon, \mu)$ , therefore the correspondent frequency is given by:

$$f_{mnp} = \frac{v}{\lambda_{mnp}} = v \left[ \left( \frac{1}{\lambda_c^2} \right) + \left( \frac{P}{2L} \right)^2 \right]^{1/2} \quad (2.1.5)$$

Since  $v = \frac{c}{\sqrt{\epsilon \mu}}$ ,  $f_{mnp}$  is related to the cavity dimension and the medium propagation properties. This derivation can be found and explained in detail in [2].



## 2.2 Energy considerations in a resonant cavity

The solutions to Maxwell's equations for a cavity resonator are often referred to as source free solutions; this is because the fields are supported by the structure even though the sources that established the field have been decreased to zero. The expression of energy conservation generally used for a source free region enclosed by a perfectly conducting surface or metallic walls is:

$$0 = j\omega_r \iiint_v \left( \mu |H|^2 - \epsilon |E|^2 \right) dv \quad (2.2.1)$$

Since the resonant frequency is not zero, the equation 2.2.1 can be transformed into:

$$\iiint_v \left( \mu |H|^2 \right) dv = \iiint_v \left( \epsilon |E|^2 \right) dv \quad (2.2.2)$$

The time-average energy stored in the electric field is equal to the time-average energy stored in the magnetic field, for each resonant mode. This is a characteristic of all cavity resonators. As previously said, the energy oscillates back and forth between the electric and the magnetic fields, a behavior also shown by a circuit made up of lumped-constant elements.

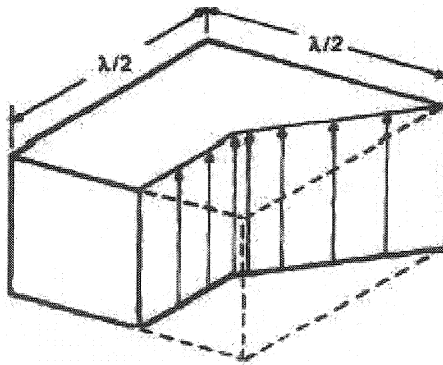


Figure 2-2: Rectangular cavity electric field pattern

In the case of a rectangular cavity, Figure 2-2, the electric and magnetic fields are determined by:

$$\begin{aligned}
 E_x &= E_z = H_y = 0 \\
 E_y &= 2jE_0 \sin \frac{\pi z}{d} \sin \frac{\pi x}{a} \\
 H_x &= \frac{2E_0 \sqrt{1 - \left(\frac{w_c}{w_r}\right)^2}}{\eta} \cos \frac{\pi z}{d} \sin \frac{\pi x}{a} \\
 H_z &= \frac{-2E_0 w_c}{\eta w_r} \sin \frac{\pi z}{d} \cos \frac{\pi x}{a}
 \end{aligned} \tag{2.2.3}$$

The next step is to calculate the total energy stored in the electric field and the total energy stored in the magnetic field to assure and prove that these quantities are indeed equal.

In the case of the electric field the total time-average stored is:

$$\begin{aligned}
 \frac{1}{2} \iiint \frac{1}{2} \epsilon |E|^2 dv &= \int_0^d \int_0^b \int_0^a \frac{\epsilon_0}{4} 4 |E_0|^2 \sin^2 \frac{\pi z}{d} \sin^2 \frac{\pi x}{a} dx dy dz \\
 &= \epsilon_0 \frac{|E_0|^2}{4} abd
 \end{aligned} \tag{2.2.4}$$

In the case of the magnetic field the total time-average stored is:

$$\begin{aligned}
 \frac{1}{2} \iiint \frac{1}{2} \mu |H|^2 dv &= \int_0^d \int_0^b \int_0^a \frac{\mu_0}{4} \frac{4 |E_0|^2}{\eta^2} \left\{ \left[ 1 - \left( \frac{w_c}{w_r} \right)^2 \right] \cos^2 \frac{\pi z}{d} \sin^2 \frac{\pi x}{a} + \left( \frac{w_c}{w_r} \right)^2 \sin^2 \frac{\pi z}{d} \cos^2 \frac{\pi x}{a} \right\} dx dy dz \\
 &= \frac{4\mu_0 |E_0|^2}{4\eta^2} \left[ 1 - \left( \frac{w_c}{w_r} \right)^2 + \left( \frac{w_c}{w_r} \right)^2 \right] \frac{abd}{4} \\
 &= \frac{\mu_0 |E_0|^2}{4\mu_0 / \epsilon_0} abd \\
 &= \epsilon_0 \frac{|E_0|^2}{4} abd
 \end{aligned} \tag{2.2.5}$$

With the results of Eq. 2.2.4 and Eq. 2.2.5, Eq. 2.2.2 has been proved.

### 2.3 Q factor definition

So far, this work has conducted a theoretical review of the cavities based on the fact that we have no losses on the cavity and that it is a perfect trap for electromagnetic waves.

The reality is that there are damped oscillations and losses on the walls, which introduce a challenge to the mathematical solution and requires expressing the behavior of the real cavities in terms of the power losses. However, it can be yet assumed that the losses are small and that the magnetic and electrical fields remain constant compared to the oscillation frequency.

The Q of any resonant circuit may be defined as:

$$Q = 2\pi \frac{\text{maximum energy stored per cycle}}{\text{Energy dissipated per cycle}} \quad (2.3.1)$$

To obtain the peak energy in a rectangular cavity we can integrate  $\frac{1}{2} \epsilon_0 |E|^2$  over the volume. Using Eq. 2.2.3 the follow expression is obtained:

$$W(\text{stored}) = \frac{1}{2} \epsilon_0 \frac{4|E_0|^2 a^3}{4} = \frac{\epsilon_0 |E_0|^2 a^3}{2} \quad (2.3.2)$$

If the rectangular cavity is a cube, the power dissipated on one of the sides is given by:

$$P(\text{side}) = \int_0^a \int_0^a \frac{1}{2} |J_s|^2 R_s a \, dz = \frac{R_s a^2 |E_0|^2}{Z_0^2 (TE)} \quad (2.3.3)$$

Due to symmetry, the power dissipated on the four sides will be four times  $P(\text{side})$ . The power dissipated on the top will be:

$$P(\text{top}) = \int_0^a \int_0^a \frac{1}{2} |J_s|^2 R_s \, dx \, dz = \frac{R_s a^2 |E_0|^2}{Z_0^2 (TE)} \quad (2.3.4)$$

Therefore, the total power lost is:

$$P(\text{total}) = \frac{6R_s a^2 |E_0|^2}{Z_0^2 (TE)} \quad (2.3.5)$$

And Q is:

$$Q = 2\pi f_r \frac{\frac{\epsilon_0 |E_0|^2 a^3}{2}}{\frac{6R_s a^2 |E_0|^2}{Z_{0(TE)}^2}} = \omega_r \frac{\epsilon_0 Z_{0(TE)}^2 a}{12R_s} \quad (2.3.6)$$

Now, for a cubical cavity we have:

$$\begin{aligned} \omega_r &= \frac{1}{\sqrt{\mu_0 \epsilon_0}} \sqrt{2} \frac{\pi}{a} \\ \omega_r &= \sqrt{2} \omega_c \\ Z_{0(TE)} &= \sqrt{2} \eta \end{aligned}$$

The final expression for Q is:

$$Q = \frac{\sqrt{2} \pi \eta}{6R_s} \quad (2.3.7)$$

A different method to obtain the Q factor of a cavity is explained in [2], and it goes as follows:

A method to explain the existence of losses could be developed by introducing a complex frequency:

$$\Omega = \omega + j\alpha \quad (2.3.8)$$

Where  $\omega$  is a real part of the impulse and  $\alpha$  is the imaginary part related directly to the losses.

The electric field in terms of the complex frequency is:

$$\epsilon e^{j\Omega t} = \epsilon e^{-\alpha t} \cdot e^{j\omega t}, \quad (2.3.9)$$

Where  $\alpha$  is the attenuation coefficient (Np/s). It is important to note that on Eq. 2.3.2 the attenuation  $\alpha$  is expressed as a time function.

When the electromagnetic energy stored on the cavity has a dominant mode, it is a time function and it is exponential too:

$$\bar{E}(t) = \bar{E}(0) \cdot e^{-2\alpha t} \quad (2.3.10)$$

Where  $\bar{E}$  is the average energy stored in the cavity.

If we take the derivative of Eq. 2.3.10 in a short period  $T$ , we end up with the following expression:

$$\alpha = \frac{\bar{E}(t) - \bar{E}(t+T)}{2\bar{E}T} = \frac{W_p}{2\bar{E}} \quad (2.3.11)$$

Where  $W_p$  is decrease of energy per unit time (losses).

In a problem like this, in which amplitude changes exponentially with time, it is convenient to introduce the concept of  $Q$ :

$$\alpha = \omega / 2Q \quad (2.3.12)$$

The following equation shows the relation between the attenuation coefficient  $\alpha$  and the  $Q$  factor:

$$Q = \frac{\omega}{2\alpha} = \omega \frac{\bar{E}}{W_p} \quad (2.3.13)$$

In other words,  $Q$  is the ratio between the average energy inside the cavity and the decrease of energy per second.

By analogy, the  $Q$  factor is the same concept used in resonant RLC circuits. The quality factor  $Q$  is a dimensionless number in the order of  $10^3$  or  $10^4$ . The energy stored in a cavity suffers attenuation due to  $e^{-(\omega/Q)t}$ , in the order of  $1/e$  of the initial value, during a period of time  $t_0 = Q/\omega$ .

All energy losses will increase the attenuation coefficient  $\alpha$ , decreasing the cavity quality factor  $Q$ . The losses are classified in three mayor groups, as follows:

$W_{wall}$ , losses related to the cavity walls.

$W_d$ , dielectric losses.

$W_{ext}$ , external losses, generated when coupling the cavity with external devices. If dealing with matched structures, this term can be negligible.

The total loss is expressed as follows:

$$W_{Total} = W_{wall} + W_d + W_{ext} \quad (2.3.14)$$

By using Eq. 2.3.12 and Eq. 2.3.13, a general expression for  $Q$  is obtained:

$$\frac{1}{Q_{Total}} = \frac{1}{Q_{wall}} + \frac{1}{Q_d} + \frac{1}{Q_{ext}} \quad (2.3.15)$$

## 2.4 Cavity design

Several aspects should be considered in order to achieve a good cavity design. Some of the most important are:

- Resonant frequency
- Coupling factor
- Q factor

### 2.4.1 Resonant frequency

So far, the basic and fundamental theory behind a resonant cavity has been explained. Now it is time to design a resonant cavity that will act as a frequency selector in an oscillator design. The frequency of interest is between 24 and 24.5 GHz; since the cavity to be used is built on SIW, it is important to explain the transition between the classic procedure to design a conventional rectangular cavity and the procedure to design a SIW cavity.

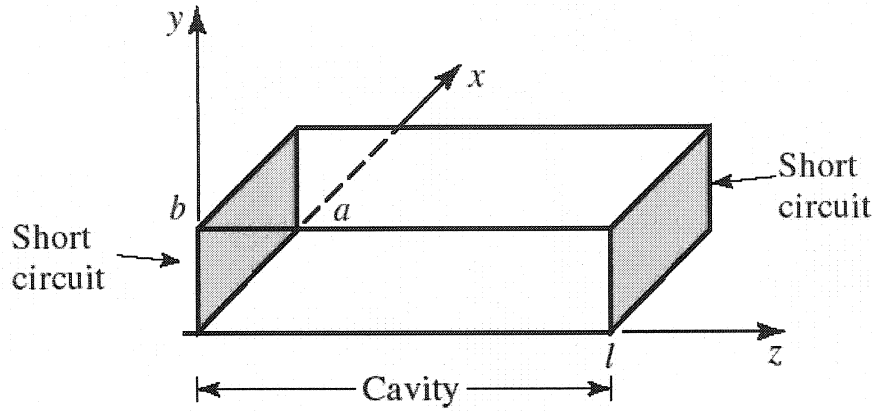


Figure 2-3: Rectangular cavity with short circuit

Figure 2-3 shows the shorting plates that are placed over both ends of a waveguide section. Let us remember that at the shorting plates, the reflection coefficient  $\Gamma$  is -1. It should be assumed that the cavity is hermetic and there is no energy leakage. There are two waves inside the resonator cavity, the incident and the reflected, both of which are equal in magnitude and phase at each end of the structure. If we recall Eq. 2.1.1 to Eq. 2.1.5 it is possible to extract the resonant frequency for this cavity.

Since  $v = \frac{c}{\sqrt{\epsilon\mu}}$ , Eq. 2.1.5 can be rewritten as:

$$f_{mnp} = \frac{c}{\sqrt{\epsilon\mu}} \sqrt{\left(\frac{m}{L_{eff}}\right)^2 + \left(\frac{n}{W_{eff}}\right)^2} \quad (2.4.1)$$

As presented in [3], where:

$$L_{eff} = L - \frac{D^2}{0.95.b}$$

$$W_{eff} = W - \frac{D^2}{0.95.b}$$

$b$  is the distance between holes,  $L$  and  $W$  are the dimensions of the cavity,  $b$  is the space between holes, and  $D$  the via hole diameter. Equation 2.4.1 is valid for  $b \leq \lambda_0 / 2$  and  $b < 4D$ , and allows for high accuracy in SIW cavity design.

The via hole diameter has been limited by the minimum diameter of the drill, which is 0.78 mm, so the larger separation between holes could be of 1.57 mm, according to [4]. There is no physical constrain with these dimensions at 24 GHz.

Figure 2-4 shows the first approximation of the cavity design at 24 GHz, using equation 2.4.1.

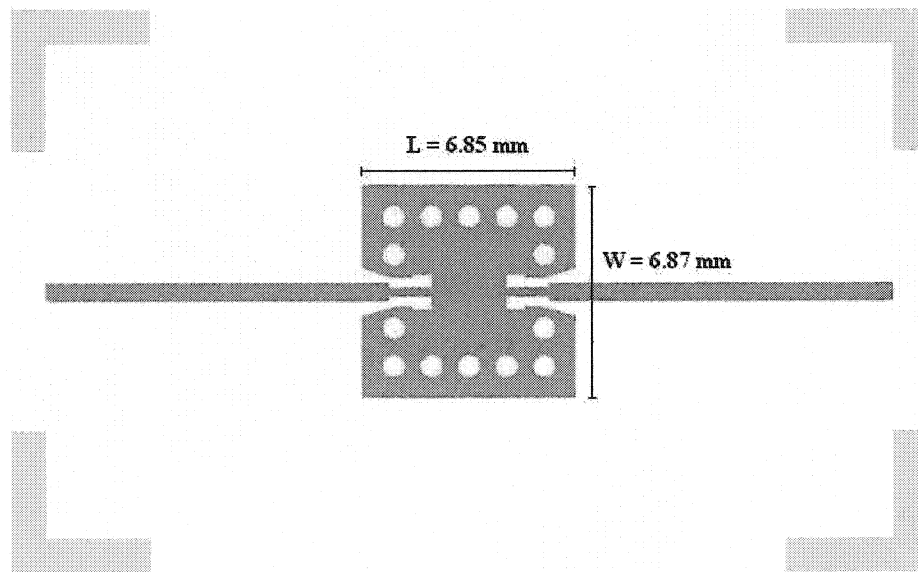


Figure 2-4: Resonant cavity using SIW

The SIW periodic structure is much more complex for analysis than the conventional waveguide. Simulations of the integrated waveguide using the finite element method are required and demand large computer resources. The design of such structure is not straightforward; to improve the design efficiency, the simulation of the equivalent rectangular waveguide structure should be performed; once the system has been developed and optimized, the cavity should be re-analyzed, and the metallic walls should be replaced by vias.



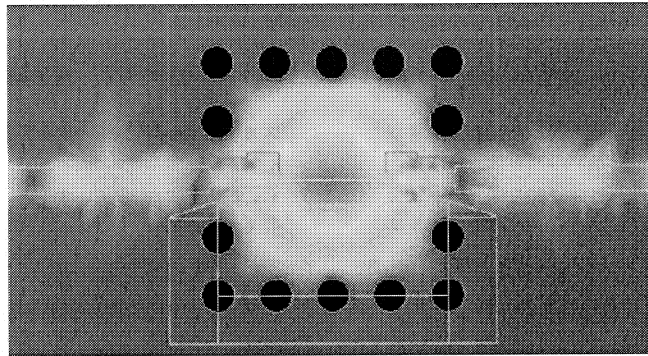


Figure 2-5: Electric field inside a SIW resonant cavity

As it can be seen in Figure 2-5, the SIW cavity successfully behaves as a metal cavity, even with a single row of via holes instead of two or more, as in [3]. The electromagnetic field is enclosed in a surface equivalent to a metallic-wall cavity.

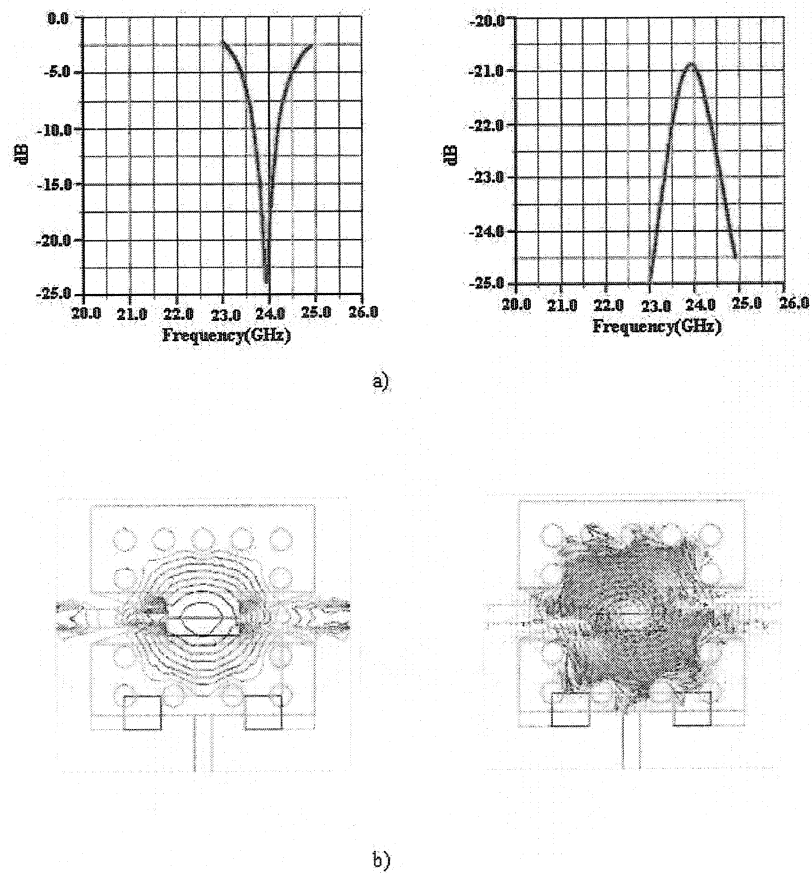


Figure 2-6: a) Plots of  $S_{11}$ ,  $S_{13}$ , b) Electric and magnetic fields inside the cavity

The results of HFSS [33] simulations give an idea of how the cavity will behave. Figure 2-6 shows the S-parameters and a return loss of -23.5 dB at 24 GHz. It is also possible to appreciate the electric and magnetic fields inside the cavity.

### 2.4.2 Coupling factor

Up to this point, the behavior of an ideal rectangular cavity has been analyzed. In the previous section, was not considered the fact that the cavity has to interact with the environment; since we are dealing with an enclosed structure it is very likely to achieve a high Q provided that the structure is connected in some way with the whole circuit.

Resonant cavities are broadly used in many microwave applications. In this particular case, a cavity is used as a frequency selector that combined in a proper manner with a power amplifier will lead us to obtain an oscillator device. To achieve the maximum circuit performance, it is key to make sure that the efficient energy transfer will be maximized. Therefore, the input impedance matching is a relevant issue for our circuit.

As mentioned by Ramo [26], it is essential that the oscillations are excited in an enclosed cavity, requirement that can be fulfilled by coupling electromagnetic energy to the cavity by any of the following methods:

- Introduction of a conducting probe or antenna in the direction of the electric or magnetic field lines.
- Introduction of a pulsating electron beam passing through a small gap in the resonator in the direction of the electric field.
- Introduction of a hole or iris between the cavity and the driving waveguide.

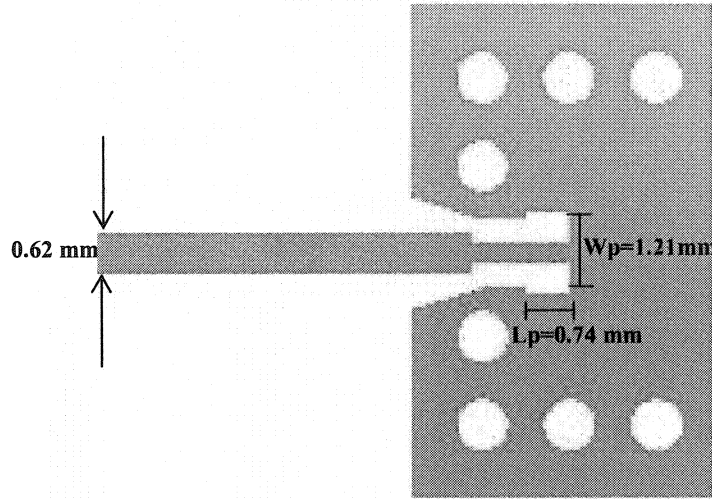


Figure 2-7: Coupling probe

The first method to coupling the cavity is used in this research project, given the physical constraints on the constructions of the other two methods. A small probe is introduced and oriented in the direction of the electric field. In Figure 2-7 the width and length of the probe are considered as degrees of freedom to improve cavity coupling.

There is, however, the challenge of coupling energy from the fields of the cavity resonator to a transmission line that connects the resonator to the rest of the system. The coupling effect introduced by our probe is the same as the one introduced by a coaxial feed line discussed in Pozar [24].

The probe couples to the magnetic field of the cavity ( $TE_{10}$  mode), and acts as a voltage source for which the open circuit voltage can be determined by the application of Maxwell's equation:

$$\oint E \cdot dl = -j\omega\mu \iint H \cdot da \quad (2.4.2)$$

When the magnetic field linking the probe is parallel to the surface vector, the value of  $V_{oc}$  is given by:

$$V_{oc} = -j\omega\mu \iint H da \quad (2.4.3)$$

A current will flow in the probe and the voltage at the input to the transmission line will be lower than the open circuit voltage.

To find the coupling level, the values for the external  $Q_e$  can be used and the unloaded  $Q$  to calculate the coupling coefficient  $g$ , where:

$$g = \frac{Q}{Q_e} \quad (2.4.4)$$

As the probe compares in size with the cavity, the cavity coupling is very sensitive to any changes in value of  $W_p$  and  $L_p$ . Therefore, several simulations are needed to fine tune the cavity resonance frequency and its coupling.

In some cases it is necessary to couple the cavity to another cavity or waveguide, task that requires finding the mathematical model. To obtain the depart values of the mathematical model we have used a sound method derived by [7].

As a matter of fact, our cavity is a pass band filter, and in that sense it is possible to find its equivalent lumped circuit. If a Tchebyscheff response is selected for the filter, the values of inductance (L) and capacitance (C) can be found in the filter itself.

Generally speaking, it is necessary to consider the values of both L and C for this analysis, but to speed up the design procedure it is convenient to use equivalents forms of those inductances or capacitances. Furthermore, introducing the concept of an idealized inverter allow to simplify the analysis procedure.

The impedance inverter or K inverter acts like a quarter-wavelength with an impedance K at all frequencies, so to calculate the impedance at both ends of the inverter the following scheme is used:

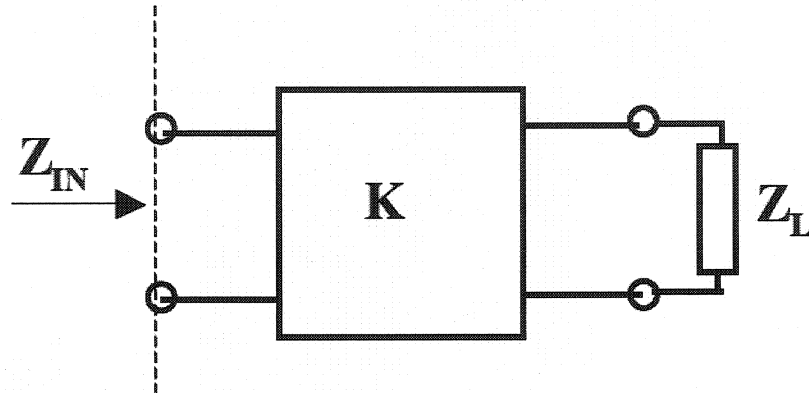


Figure 2-8: K inverter

$$Z_a = \frac{K^2}{Z_b} \quad (2.4.5)$$

The admittance inverter or J inverter has the same characteristic of the K inverter; in this case the admittance is the issued value.

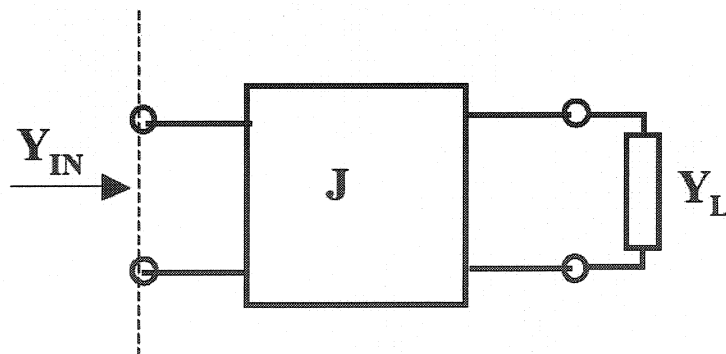


Figure 2-9: J inverter

$$Y_a = \frac{J^2}{Y_b} \quad (2.4.6)$$

We can model our cavity by using an equivalent lumped L, C circuit. As is commented in Matthaei's book [20], circuits in Figure 2-10 and Figure 2-11 are a very good

approximation when dealing with discontinuities on the micro strip or transmission line.

We can find the values for  $K$ ,  $J$ , and  $\phi$  from:

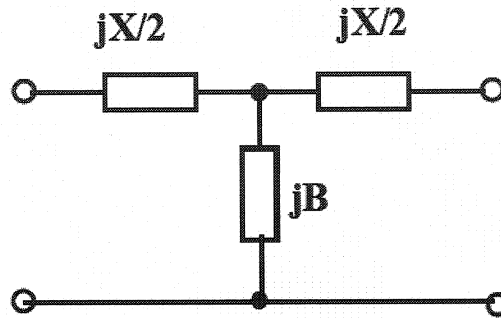


Figure 2-10: T equivalent

$$K = Z_0 \left| \tan \left( \frac{\phi}{2} + \tan^{-1} \frac{X_a}{Z_0} \right) \right| \quad \text{Ohms} \quad (2.4.7)$$

$$\phi = -\tan^{-1} \left( \frac{2X_b}{Z_0} + \frac{X_a}{Z_0} \right) - \tan^{-1} \frac{X_a}{Z_0} \quad \text{radians}$$

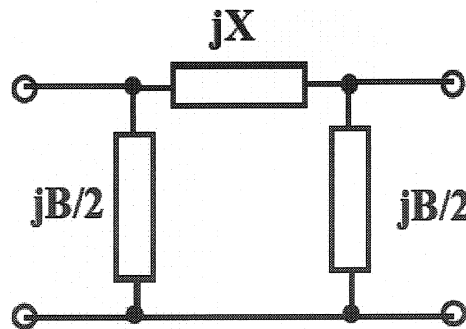


Figure 2-11:  $\pi$  equivalent

$$\begin{aligned}
 J &= Y_0 \left| \tan \left( \frac{\phi}{2} + \tan^{-1} \frac{B_a}{Y_0} \right) \right| && \text{siemens} \\
 \phi &= -\tan^{-1} \left( \frac{2B_b}{Y_0} + \frac{B_a}{Y_0} \right) - \tan^{-1} \frac{B_a}{Y_0} && \text{radians}
 \end{aligned}
 \tag{2.4.8}$$

Now that the impedance value of our cavity is known, the next step is to find the level of excitation of the mode for a given probe. As discussed in Collin [7], the level of excitation can be found by calculating the general expansions for the field, as follows:

$$E = \sum_n e_n E_n + \sum_n f_n F_n \tag{2.4.9}$$

$$H = \sum_n h_n H_n + \sum_n g_n G_n \tag{2.4.10}$$

Where  $e_n$  and  $h_n$  are the expansions coefficients.

After the optimization process using HFSS to simulate the resonant cavity, it can be concluded that the best values for  $W_P$  and  $L_P$  are:  $W_P = 1.21$  mm,  $L_P = 0.74$  mm, as shown in Figure 2-7.

### 2.4.3 Q factor

In section 2.3 a mathematical description of the Q factor was presented; in this section, practical design issues in relation to the Q factor will be discussed

Different types of Q factors encountered in real scenarios can be redefined by saying:

$$Q_u = 2\pi f \text{ (Energy stored in the cavity) / (Power dissipated in the cavity)}$$

$$Q_E = 2\pi f \text{ (Energy stored in the cavity) / (Power dissipated in the load)}$$

$$Q_L = 2\pi f \text{ (Energy stored in the cavity) / (Power dissipated in the load plus cavity)}$$

$Q_L$  is the measured quantity, loaded Q. Considering the fact that the cavity is not alone in the circuit and that it has to be related to an input and an output circuit, the following can be defined:

$Q_u$  = Unloaded Q of cavity

$Q_E$  = External Q of input circuit and output circuit

$Q_L$  = Total loaded Q including cavity, input and output losses

One of the most common methods to measure the Q factor is to use the amplitude of the resonant curve. The loaded Q of the circuit, as shown in Figure 2-12, is obtained by taking the frequency difference between its 3 dB points and dividing it by the resonant frequency  $f_0$  [13].

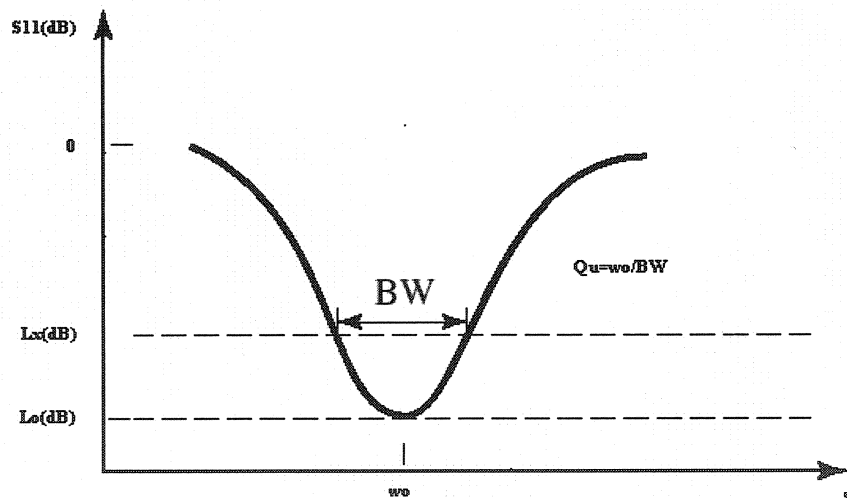


Figure 2-12: Plot of  $S_{11}$  to calculate the Q factor

Other methods to obtain  $Q_L$  use the impedance curve on the Smith chart. To apply those methods it is important to understand that there is a relationship among the resonator transmission, the reflection coefficients and the cavity Q.



The VSWR (Voltage Standing Wave Ratio) is defined as:

$$VSWR = (1 + |\Gamma|) / (1 - |\Gamma|) \quad (2.4.11)$$

Therefore:

$$\Gamma = \frac{\left(1 - \frac{Y}{Y_0}\right)}{\left(1 + \frac{Y}{Y_0}\right)} \quad (2.4.12)$$

So, the required coupling VSWR will determine the  $Q_L$ .

## 2.5 Measurements and results

Measurements are conducted using network analyzers such as the Hewlett Packard HP 8510; it is possible to adjust the analyzer phase control to make  $f_0$  lie on the real axis on the low impedance side of the chart. Using the analyzer's difference frequency mode, the measuring point is rotated along the resonant curve at a frequency  $f_0 + \delta f$ ; the reactance  $X$  has been made equal to the resistance  $R$ . Then, it is possible to calculate  $Q_L$  using:

$$Q_L = f_0 / 2\delta f \quad (2.4.13)$$

This is basically the same equation as the one used by the amplitude method where  $2\delta f$  is the frequency difference between the 3dB points.

### 2.5.1 Single cavity resonator

Until now all the relevant parameters to design a resonant cavity have been underlined. In the beginning, the idea was to design a cavity with three ports: the input port, the output port and the feedback port. Later, it became clear that a better option was to have

a microstrip line as the input port and a SIW structure as the output port, as it is shown on Figure 2-13.

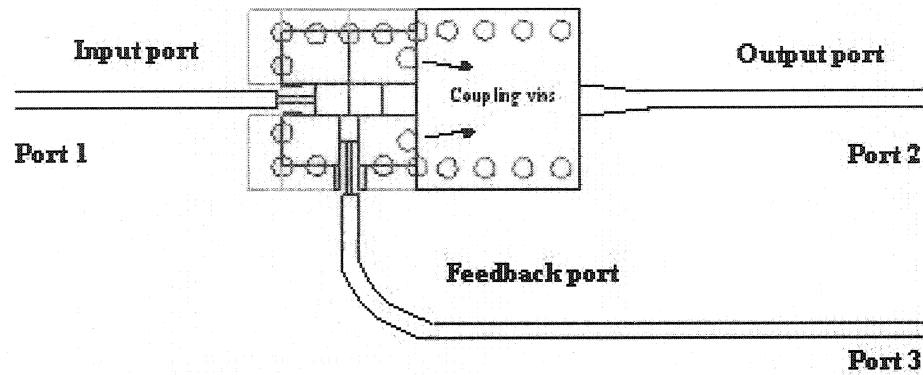
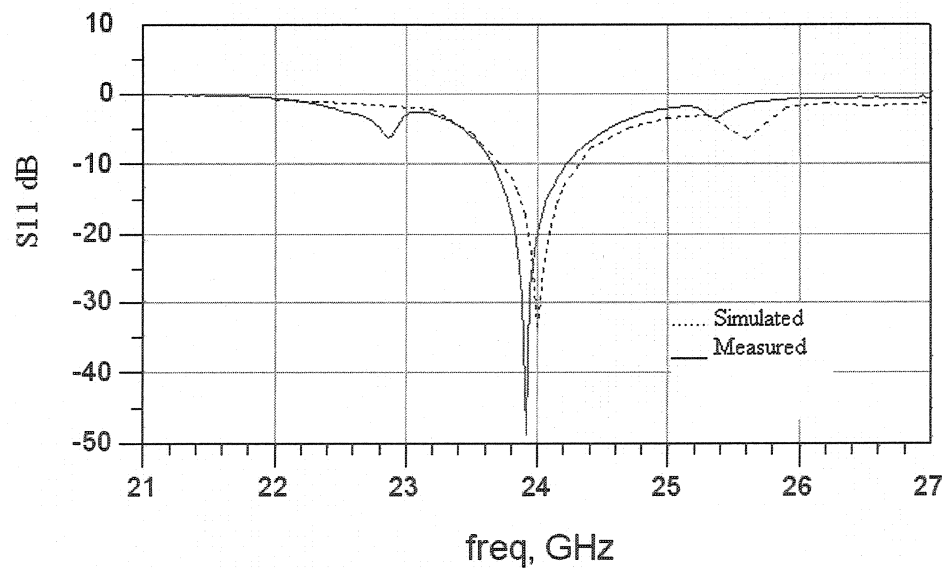


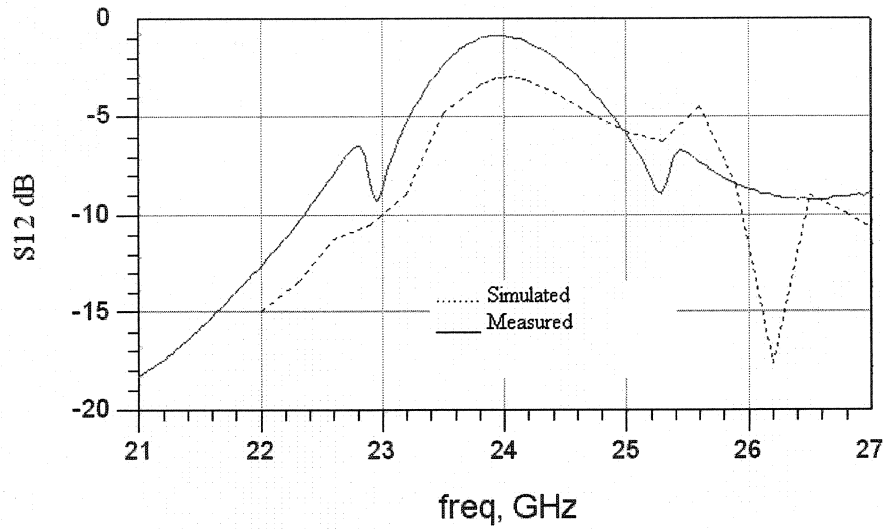
Figure 2-13: SIW resonant cavity with coupling vias

The position of the coupling vias allows the impedance matching between the cavity and the SIW output.

In Figure 2-14, we observe the  $S_{11}$  and  $S_{12}$  correlation between the simulation and the measured results using the HP 8510 Network analyzer.



a)



b)

Figure 2-14: Simulated and measured results a)  $S_{11}$ , b)  $S_{12}$

Given that measured  $S_{11}$  was -45 dB and simulated  $S_{11}$  was -32 dB, a frequency shift of 100 MHz between the simulation and the measurement can be observed. In the case of  $S_{12}$  the measured one was -0.9 dB and the simulated one was -2.9 dB.

As mentioned in section 2.4.3 the Q factor can be calculated using the frequency difference between its two 3 dB points, divided by the resonant frequency  $f_0$ . By applying this rule the following results are obtained:

$$\text{Measured case } Q = \frac{23.91\text{GHz}}{23.915\text{GHz} - 23.905\text{GHz}} = 2391$$

$$\text{Simulated case } Q = \frac{24\text{GHz}}{24.02\text{GHz} - 23.985\text{GHz}} = 700$$

The frequency discrimination was not small enough to see all the details on the plot, which explains the difference in the Q factor. However, if we analyze the shape of the

curves we can see that they are similar. A picture of the device built for testing is shown in Figure 2-15.

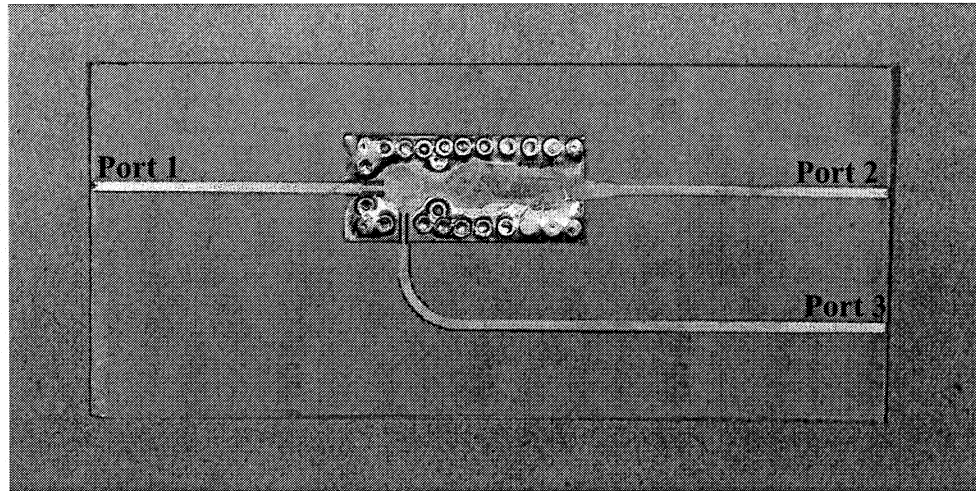


Figure 2-15: Photo of the single cavity resonator

### 2.5.2 Dual cavity resonator

Looking to improve the frequency rejection of the cavity, a change in the design was introduced. Basically, a second cavity was added to obtain a dual cavity resonator.

Figure 2-16 gives an idea of how the dual cavity looks like:

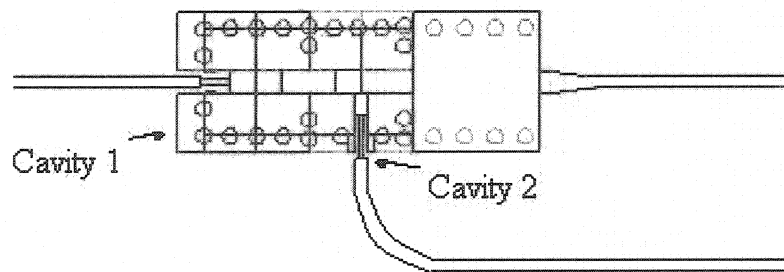


Figure 2-16: Dual cavity

After simulating and testing the dual cavity resonator, it became clear that adding a second cavity increase the complexity of the circuit, and that a second resonant frequency is added when the cavities are not equally liked.

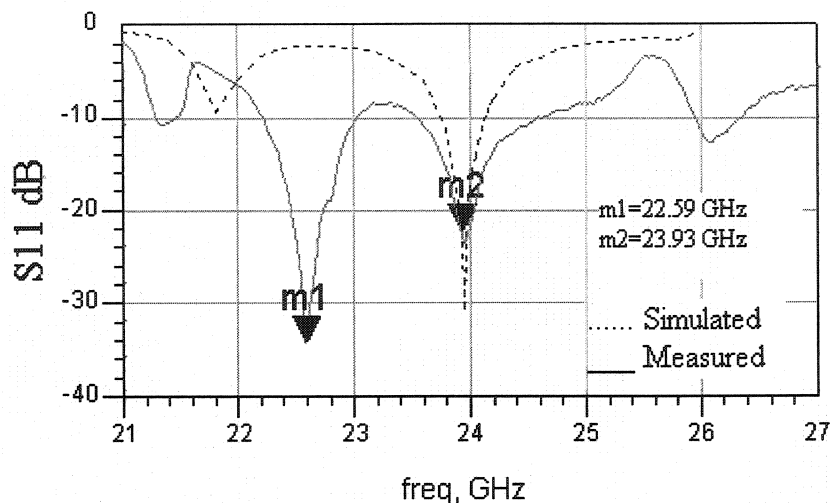


Figure 2-17:  $S_{11}$  performance of the dual cavity resonator

Figure 2-17 shows that, even though the cavities are very similar, two different frequencies were obtained, one at 22.6 GHz and other at 23.9 GHz. Having two different frequencies is not suitable for a cavity design, since the aim is to obtain a very stable resonator and be sure that it works at a particular frequency.

This chapter has covered the fundamentals for designing a resonant cavity. A method to optimize the coupling factor between the microstrip line and the cavity was presented, using a probe in which the values of the length and the width are a key factor to optimize performance. A single cavity was designed and simulated results were compared with measured ones. A dual cavity was also designed to explore the possibility of improving the frequency rejection, but simulated and measured results indicated that fine tuning the dual cavity to work at a single frequency is a hard task, and the trade off between performance and complexity is not worth it. Therefore, it was concluded that a single cavity resonator is the best choice given its lower complexity and higher stability.

## CHAPTER 3. MICROWAVE OSCILLATOR

This chapter will discuss some of the most important topics in oscillator design from a mathematical and practical perspective. The oscillator's components and its basic terminology will be examined, as well as the procedure to obtain a sound design of a microwave oscillator using the SIW technique. A brief explanation of injection locking technique will also be given and, finally, a conclusion on the analysis of the presented data based on the simulations and measured results will be provided.

### 3.1 Fundamental theory

There are many forms of oscillations that are generated by different sources that produce time-varying periodic signals. In each case, an energy source is used to produce a periodic waveform. We can consider a microwave oscillator as a DC to RF energy converter.

The oscillator is conformed by two main parts:

- The non linear active device (diode, transistor), which converts the DC power into RF energy.
- The linear passive device (resonator, and in our case a SIW cavity resonator) that serves three purposes:
  1. It provides the necessary DC bias for the device to operate,
  2. It presents an electromagnetic environment at the device terminals to initiate oscillation, and acts as a frequency selector,
  3. By its Q factor, it influences the stability of the oscillator.

One of the challenges in designing oscillators is finding the appropriate mathematical model to represent its behavior and predict its performance.

A general equation that allows finding the ideal conditions for a steady-state operation is:

$$Z_{device}(f, P_{out}, V_{dc}, I_{dc}, T, \dots) + (f, Geometry) = 0 \quad (3.1.1)$$

Where  $f$  is the operation frequency;  $P_{out}$  is the RF output power;  $V_{dc}$  and  $I_{dc}$  are the DC bias voltage and current; and  $T$  is the temperature. From this equation it can be deduced that the impedance of the device is the negative of the impedance presented by the circuit.

Van der Pol was one of the first authors to talk about non-linear analysis in an oscillator [30]. He used a vacuum tube in an inductive feedback circuit; he then assumed a non-linear relationship between input voltages to the vacuum tube and output current. The current model is:

$$i_c = a_1 i_b + a_2 i_b^2 + a_3 i_b^3 \quad (3.1.2)$$

Where  $i_c$  is the collector current resulting from base current  $i_b$ , and  $a_1$ ,  $a_2$ , and  $a_3$  are the proportionality coefficients. The third-order term  $a_3 i_b^3$  is the amplitude factor that causes amplitude-damping sign reversal at each half cycle. He derived respect to time equation 3.1.2, and assuming that the active element is biased to its inflection point, which sets  $a_2$  to zero, he obtained:

$$\frac{d^2 v}{d\tau^2} - e(1 - v^2) \frac{dv}{d\tau} = 0 \quad (3.1.3)$$

Where  $v$  is the resonant circuit instantaneous voltage and  $\tau$  is normalized time.

A reflection oscillator analysis by Esdale and Howes [11] shows both the growth of oscillations and conditions for optimum performance. The analysis started with Kurokawa's [16] and Keyton's [15] negative resistance approach, using Kurokawa's oscillator model. Esdale and Howes then converted it to a reflection coefficient analysis. They showed that, when converting their results back to the impedance form, the Kurokawa and Keyton results were verified. It is important to mention that the work done by Kurokawa is a milestone in oscillator's analysis and design.

In a practical case, the noise is not at a single frequency  $f_l$ , but at a band of frequencies fluctuating randomly both in frequency and phase.

For the Van der Pol analysis some conclusions can be drawn:

- The oscillations will never begin spontaneously; an initial signal is needed to start it. This signal is the circuit noise.
- The active element contributes the energy needed to initiate steady state oscillations. As a condition, this energy must be greater than the one dissipated in the oscillator's loop.

### 3.2 Active and passive devices considerations

The previous section mentioned that an oscillator is made up of two parts, the linear passive device (Resonator, and in our case a SIW cavity) and the non-linear active device (Diode, transistor). The analysis, design, simulations, and construction of the passive devices were already explained in Chapter 2. In regards to the amplifier (active device), there are some parameters that will facilitate choosing the one that best suits this research requirements. Gunn devices, IMPATT diodes, and tunnel diodes may be used for an oscillator; however, a bipolar transistor would offer the optimum solution given its low noise and high stability [28]. Better noise performance can some times be achieved with a lower-frequency bipolar transistor oscillator multiplied. Field-effect transistor (FET) is a surface device whose  $1/f$  noise will be appreciable higher than that of a bipolar one, even though such effect loses importance at high frequencies. The high electron mobility (HEMT) and MESFET transistor show promised for better noise than FET devices [25].

Since one of this project's goals is to design and construct a low cost RF power source flexible in design, the commercial amplifier HMC283LM1 Hittite has been chosen. This particular model is a medium power amplifier that has a bandwidth between 17 and 40 GHz, and is a surface mount broadband millimeter wave package with low loss and excellent I/O match. In order to characterize the amplifier and carry out the simulations to obtain a sound design, the amplifier was constructed and measured.



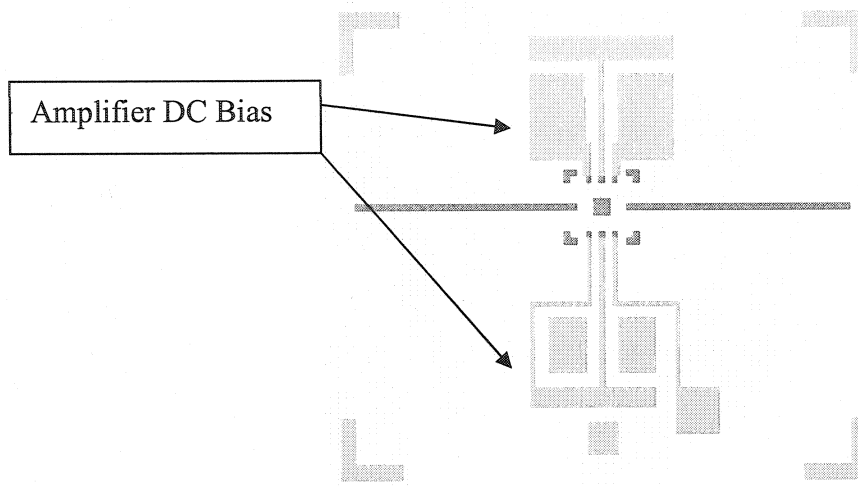


Figure 3-1: Amplifier Layout

We have used the kit TRL explained on Chapter 1, Section 1.7 to calibrate the Network Analyzer HP 8510, which is used to extract the S-parameters of the amplifier; the measurements results shown in Figure 3-2 are in agreement with the manufacturer's specifications. A  $S_{21}$  of 22 dB can be seen in the bandwidth between 20 and 30 GHz, which includes our working frequency (24-24.5 GHz).

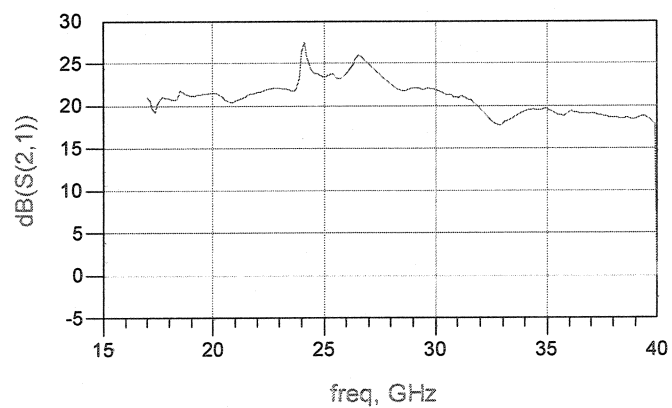


Figure 3-2: Amplifier measured gain

Even though a large bandwidth like this one could contribute to instability and spurious oscillations, it is possible to make a very selective frequency device by carefully choosing the resonator, and the performance of our oscillator can be improved by increasing the Q factor of the cavity.

### 3.3 Design Procedure

Oscillator's design has been a very important topic since Van der Pol conducted a non-linear analysis in 1927. Today, almost 80 years later, the behavior of oscillating devices is not yet fully understood; therefore, several approximations and assumptions are necessary when estimating a model.

The two elements of an oscillator (active device and passive device) must be designed and tested in compliance with the design specifications, and by combining the two elements the oscillator will be completed. However, good design and proper matching calculation are required to obtain a stable and low noise device. Due to close interrelation between the active device and the passive device, the design must be brought forward together.

It is possible to perform an analysis of the oscillator using Harmonic Balance method, which requires a completed model of the amplifier. However, since a commercial amplifier is being used in this project, the completed model is not available. To overcome this problem we have used S-parameters extracted with the network analyzer HP 8510.

As explained in Meskoob and Prasad [21], the oscillation requirement in terms of S-parameters is:

$$S_{21A} \cdot S_{21R} = 1 \quad (3.3.1)$$

Where,  $S_{21A}$  is the amplifier forward transmission S-parameter, and  $S_{21R}$  is the resonator forward transmission S-parameter.

Let us note that Eq. 3.3.1 implies two equations: the product of the two magnitudes at the resonant frequency  $f_0$  is the unity, and the sum of their phase angles is zero.

$$|S_{21A}| \cdot |S_{21R}| = 1 \quad (3.3.2)$$

$$\theta_{21A} + \theta_{21R} = 0 \quad (3.3.3)$$

Provided that coupling between the amplifier and the cavity at the desired frequency was achieved, the total gain in the feedback loop should be equal to 1 at  $f_0$  (the desired free-oscillation frequency); therefore, the amplifier gain  $S_{21A}$  should be attenuated through the feedback loop, which is composed of the resonant cavity and the network. Taking into consideration the gain drop of the amplifier in saturation, and the propagation losses and mismatching problems between the different elements, the resonant cavity parameter  $S_{13R}$  (where port one connects with the amplifier output and port 3 connects with the amplifier input) should be slightly greater than  $1/S_{21A}$  in order to compensate for those effects and start the oscillation. The total phase at the amplifier input in relation to its output should be of zero degrees; if that is not the case, the matching network should be adapted using perpendicular stubs to obtain the zero degrees.

To sum up these considerations, the desired values of the cavity parameters should be:

- $S_{11R} \approx 0 (S_{11R} = -20dB) @ f_0$
- $S_{13R} > 1/S_{21A} @ f_0$

If cavity port two is defined as the output oscillator port, the coupling at this port should be as good as possible, so:

- $S_{22R} \approx 0 (S_{22R} = -20dB)$

Finally, as ports one and two are equivalent coupling ports, the cavity is symmetric so:

- $S_{11R} = S_{22R} \approx 0 (S_{11R} = S_{22R} < -20dB)$

Tools like ADS (Advanced design system) allow us to extract the measured results of the amplifier and the cavity resonator, as well as to perform a simulation that will help us fine-tune our oscillator using the method explained in [21]. Figure 3-3 shows a schematic that is used to conduct the analysis of the oscillator in open loop.

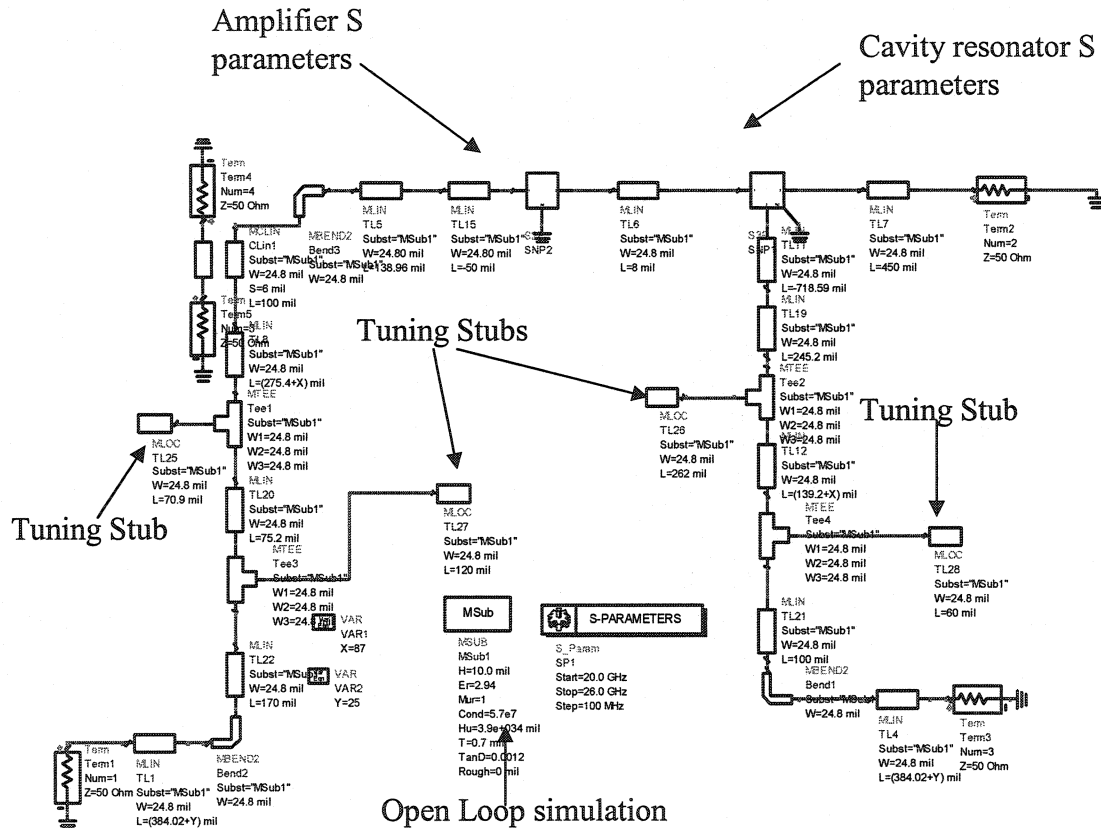


Figure 3-3: Oscillator analysis using an open loop.

To achieve the desired parameters it is necessary to first choose the length of the micro strip line that connects the output of the amplifier to the cavity input. This length must be a multiple or a fraction of the wavelength in order to optimize the RF energy transfer and minimize the reflection between the cavity and the oscillator.

Figure 3-4 shows the open loop simulation results. It is possible to see how the amplitude at  $f_0$  is 1.6 dB and the phase is 0 degrees.

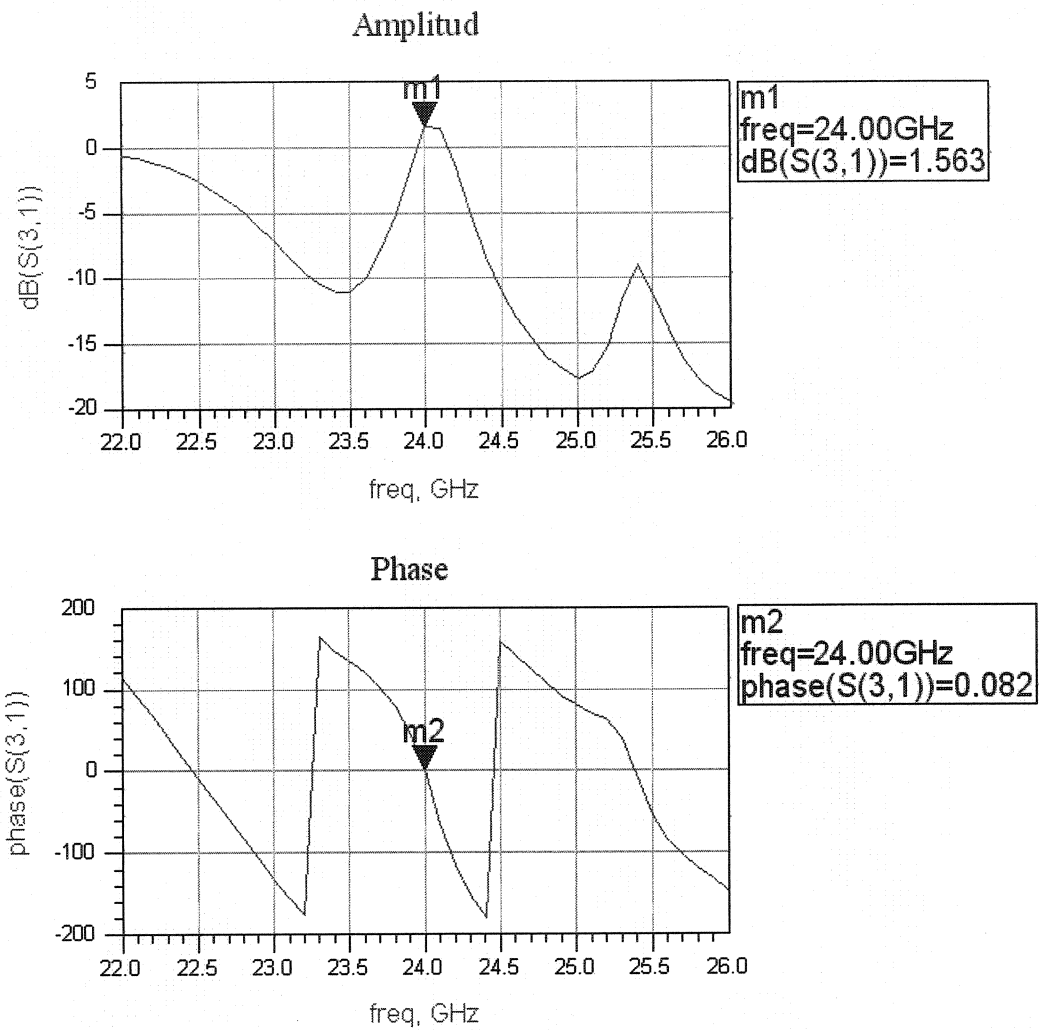


Figure 3-4: Open loop simulation results.

This simulation offers a remarkable approximation for design purposes. To fine-tune our oscillator and achieve the desired frequency, tuning stubs were added to the final layout.

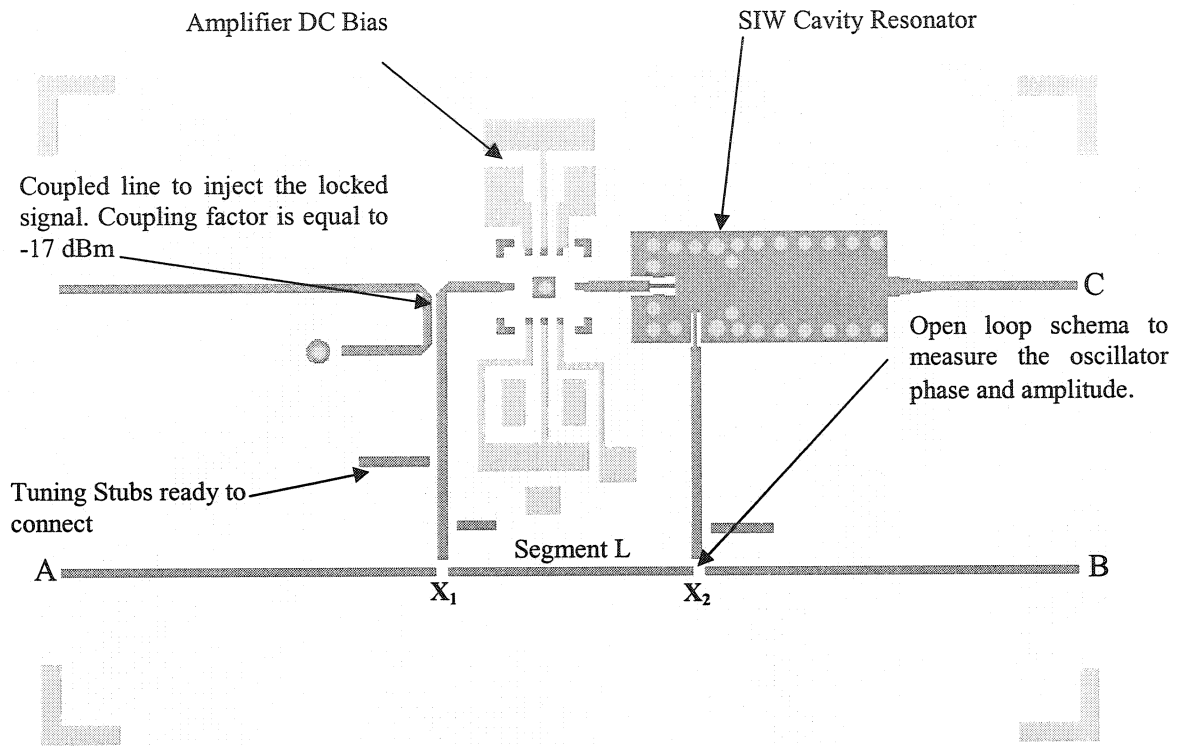


Figure 3-5: Oscillator layout with tuning stubs.

Figure 3-5, shows the presence of the open loop schema to measure the oscillator's phase and amplitude. The phase and amplitude were first measured using HP network analyzer at measure points A and B, by closing the path at  $X_1$  and  $X_2$  excluding segment L. After it was verified that measurements were as expected from the simulations, the loop was closed (through segment L) and the oscillator was connected to the spectrum analyzer to visualize the RF output at port C.

### 3.3.1 Measurement and results

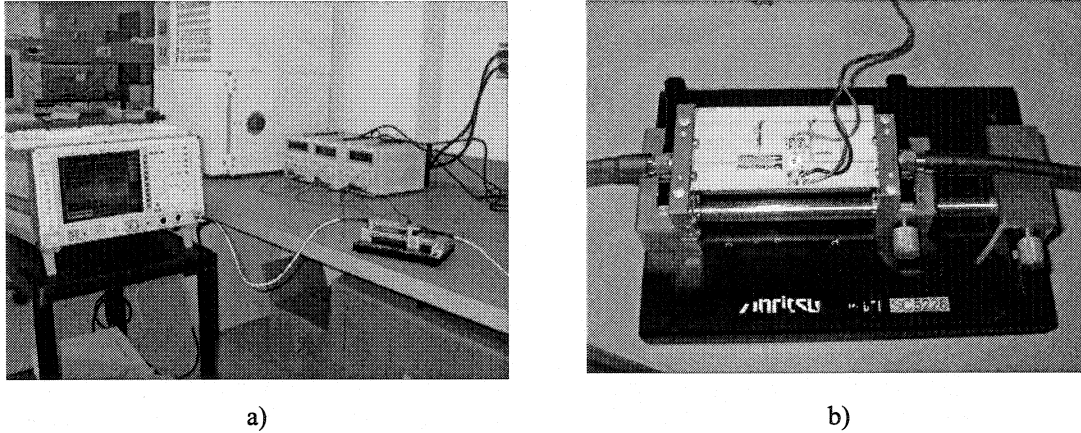


Figure 3-6: Measurements setup: a) General setup. b) Single oscillator on the test

The spectrum analyzer was used to measure the oscillator RF output. Figure 3-6 shows the measurement setup. The cable that interconnects the oscillator to the spectrum analyzer was measured in order consider all losses: the cable loss was  $-1.53$  dBm. Finally, a 20 dB attenuator to the oscillator output was added to protect the measuring equipments.

Figure 3-7 shows that the output is marked at  $-8.22$  dBm at 23.64 GHz. Taking into account the 20 dB attenuator and the 1.53 dBm of cable losses, it can be said that the RF output is 13.31 dB.

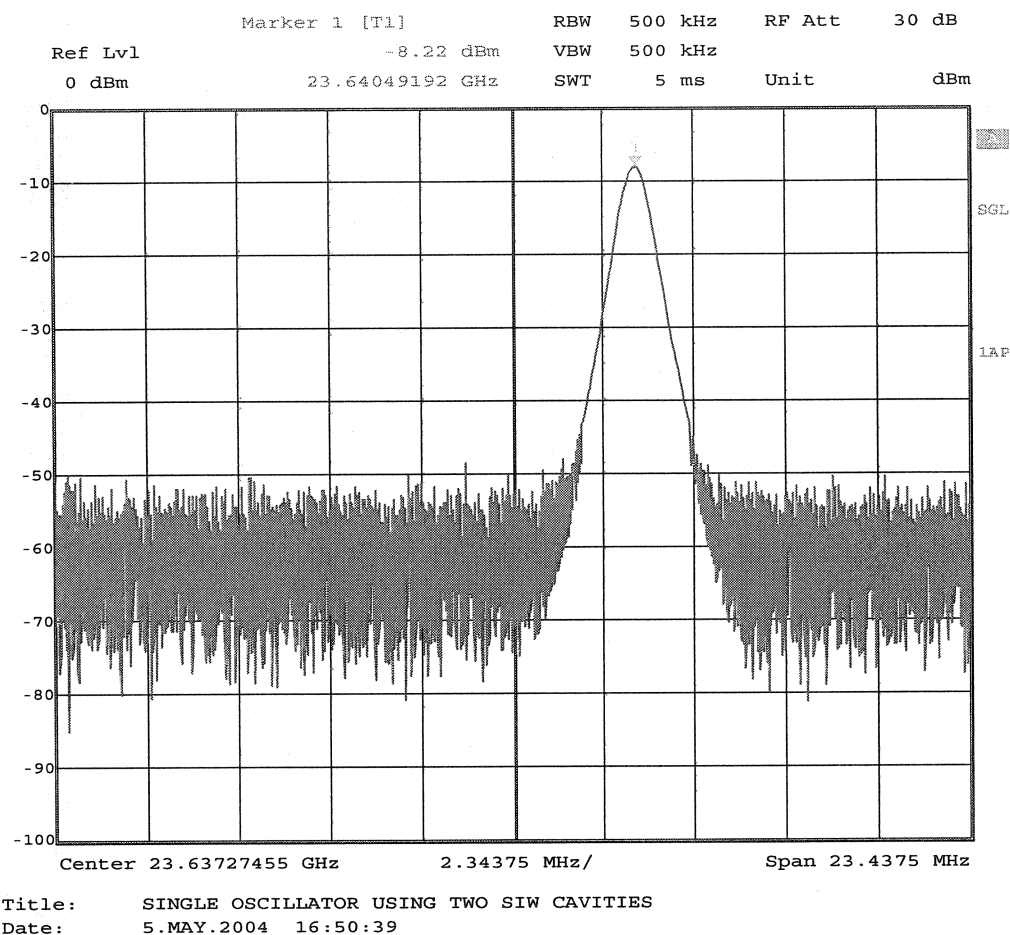


Figure 3-7: RF Oscillator output

### 3.4 Oscillator stability

An accurate and very meticulous design will minimize the spurious oscillations, the frequency pushing, the phase noise and the temperature effects. As discussed in Chapter 2, the Q factor of our cavity has a direct influence on the oscillator's stability: as the Q factor increases, the external perturbations will reduce its impact on the oscillator's performance.



### 3.4.1 Spurious oscillations

All oscillators can produce spurious signals, which are defined as oscillations at one or more undesired frequencies. They can occur at any frequency where Eq. 3.3.2 and Eq. 3.3.3 are satisfied by the microwave and bias circuit inductance and coupling capacitors. A high Q factor guarantees that the magnitude and phase conditions occur at a desired resonant frequency.

### 3.4.2 Frequency pushing

It is possible to introduce a frequency change of the oscillator by making a variation on the DC bias point of the amplifier; this phenomenon is known as Frequency Pushing. In this case, a frequency change of 131 MHz was achieved, but the output power of the device was affected as well. For research purposes, the DC polarization point of the amplifier was manually changed to better illustrate the effect, but frequency pushing can be minimized by the use of a regulator in the dc bias supply.

### 3.4.3 Temperature

Temperature is a key factor for oscillator's stability, since it affects the coefficient of thermal expansion and the thermal coefficient of the material. Temperature affects the junction of the active devices and modifies the amplifier performance; according to the manufacture data sheet, the average gain is 22 dB between - 40°C and +25°C. At our operating bandwidth the behavior of the Hittite amplifier HMC283LM1 can be consider linear.

The cavity resonator itself is the major cause of frequency drift with temperature [5]. As temperature varies, the cavity dimension changes, and so does its resonant frequency.

Given that RT/Duroid 6002 is being used as a substrate, it is worth noting that the data sheet specifications explains that the dimensions in the X and Y axis will change 16 ppm/°C and the dimension in the Z axis will change 24 ppm/°C. Since the resonant cavity Q is high, the thermal expansion will be the cause of frequency shift.

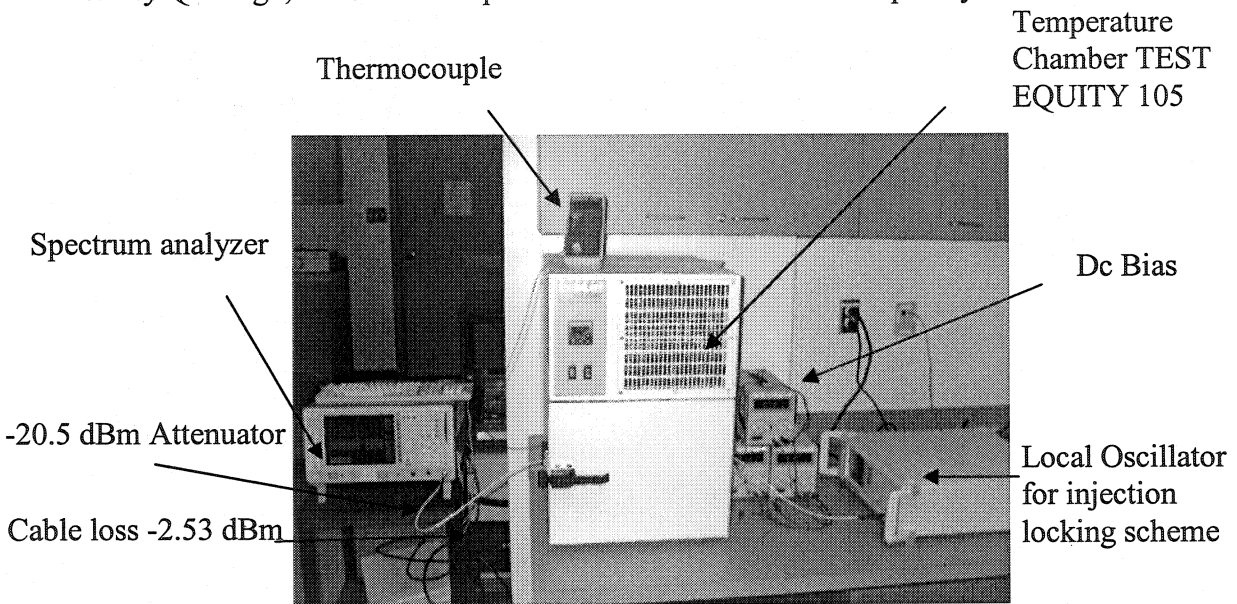


Figure 3-8: Temperature measurements setup

Temperature	I <sub>dd</sub> mA	V <sub>dd</sub> V	V <sub>gg</sub> V	Freq(Ghz)	Ampl(dBm)
-30°C	250	2.6	4.3	23.64448	-7.5
-20°C	250	2.6	4.3	23.64169	-7.8
-10°C	240	2.6	4.3	23.64120	-8.0
0°C	230	2.6	4.3	23.64105	-8.7
10°C	220	2.6	4.3	23.64095	-8.8
20°C	210	2.6	4.3	23.64028	-9.0
30°C	210	2.5	4.3	23.63780	-9.0
40°C	210	2.5	4.3	23.63570	-9.0
50°C	200	2.5	4.3	23.63293	-9.2

Table 3-1: Temperature performance of the oscillator.

Data on table 3-1 we can be better appreciated in Figure 3-9, which shows frequency variation with temperature.

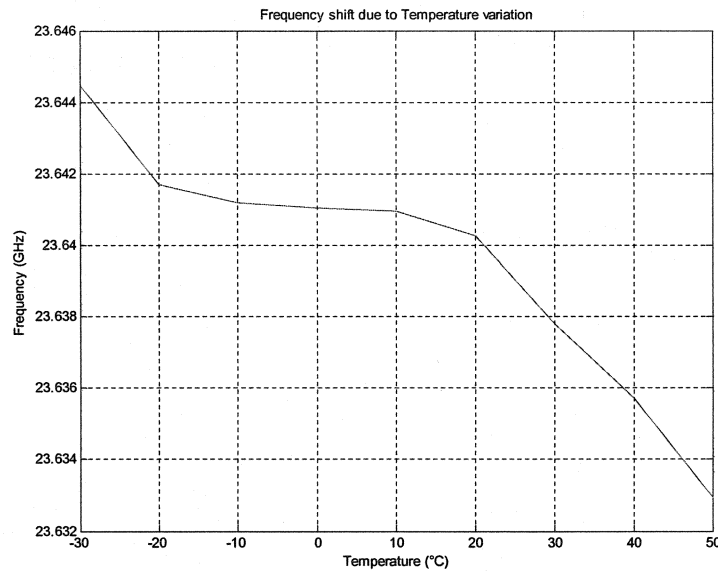
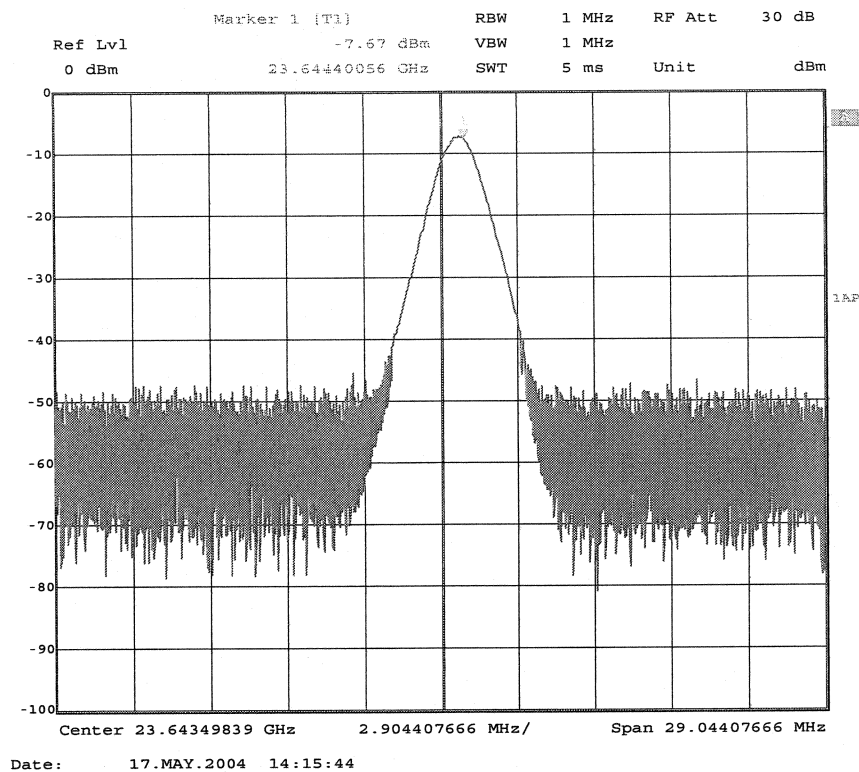


Figure 3-9: Frequency variation with temperature on a single oscillator

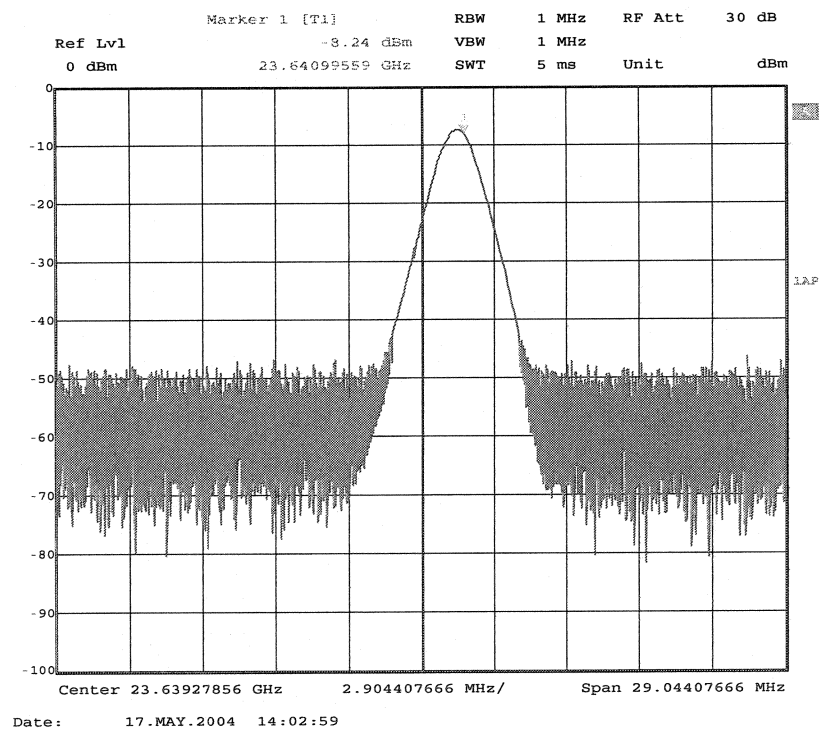
Several tests were conducted using the Temperature Chamber TEST EQUITY 105 to obtain the temperature behavior of our oscillator.

To guarantee its accuracy, the temperature measurements were conducted only when the temperature displayed by the thermocouple (real temperature of our device) and the temperature of the chamber were the same. By analyzing the data on Table 3-1 some conclusions were obtained:

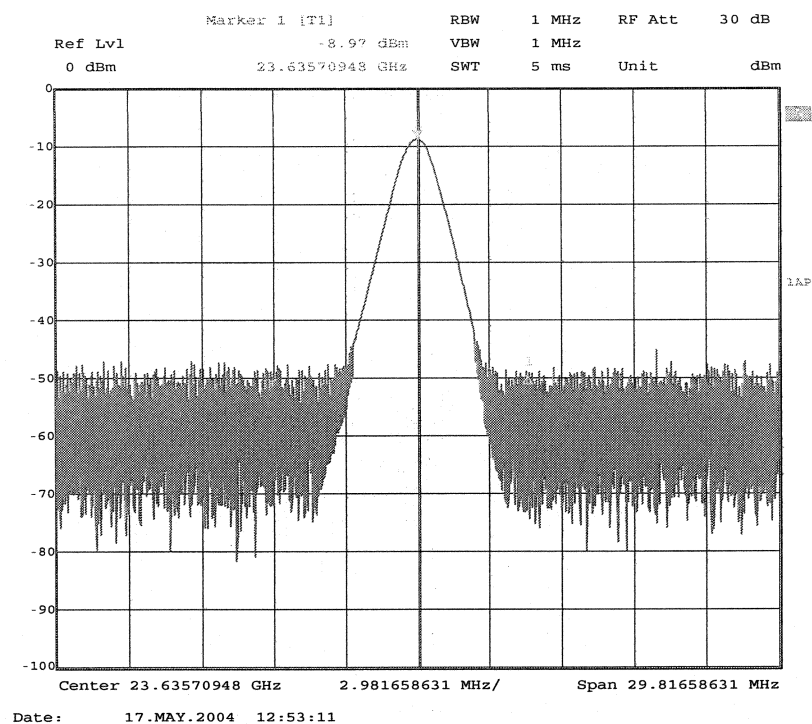
- There is a frequency shift due to temperature. At  $-30^{\circ}\text{C}$  the frequency is 23.64448 GHz and at  $50^{\circ}\text{C}$  the frequency is 23.63293 GHz. The frequency change is 11.55 MHz or 4.048%.
- By observing the drain current ( $I_{dd}$ ) it is possible to appreciate that the current consumption decreases as temperature increases. This phenomenon can be explained by the reduction of the resistance with temperature.



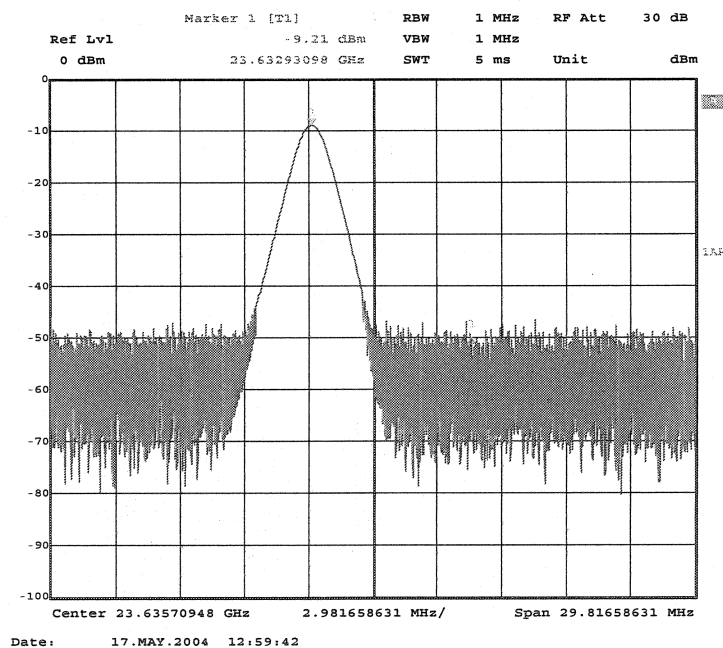
a)  $f_o = 23.64448$  GHz at  $-30^\circ\text{C}$



b)  $f_o = 23.641694$  GHz at  $-20^\circ\text{C}$



c)  $f_o = 23.63570$  GHz at 40°C



d)  $f_o = 23.63293$  GHz at 50°C

Figure 3-10: Temperature measurements results

Frequency stability requirements of 10 ppm/°C are not uncommon on the market. As an example, the VCO oscillator VPLD6, fabricated by Industrial Newsroom, was built to suit extreme temperature applications and its specifications are between 100 ppm/°C and 20 ppm/°C. To calculate the temperature performance of our oscillator, the following equation should be applied:

$$\text{ppm}/^{\circ}\text{C} = \frac{1}{\Delta T} \left( \frac{f_1 - f_2}{\frac{f_1 + f_2}{2}} \right) * 10^6 \quad (3.4.1)$$

Where,  $\Delta T$  is 80°C, and  $f_1$  and  $f_2$  are the frequencies at extreme temperatures.

Therefore, in our case the temperature performance is:

$$\begin{aligned} \text{ppm}/^{\circ}\text{C} &= \frac{1}{80^{\circ}\text{C}} \left( \frac{23.64448\text{GHz} - 23.63293\text{GHz}}{\frac{23.64448\text{GHz} + 23.63293\text{GHz}}{2}} \right) * 10^6 \\ \text{ppm}/^{\circ}\text{C} &= 6.1075 \end{aligned} \quad (3.4.2)$$

The measured results of the shift frequency with temperature are displayed on Figures 3-9 and 3-10.

#### 3.4.4 Phase noise

Phase noise is also an important factor for the oscillator's stability. A formal definition of the phase noise is the modulation of the phase of the oscillator's electromagnetic field. The noise is often measured in units of dBc/Hz, dB below the carrier per Hz away in frequency from the carrier. The measurement software used is the FSE-K4 (Phase Noise Measurement Software), which extends the measurement capabilities of the Rohde Schwarz Spectrum Analyzer used to conduct the measurements.

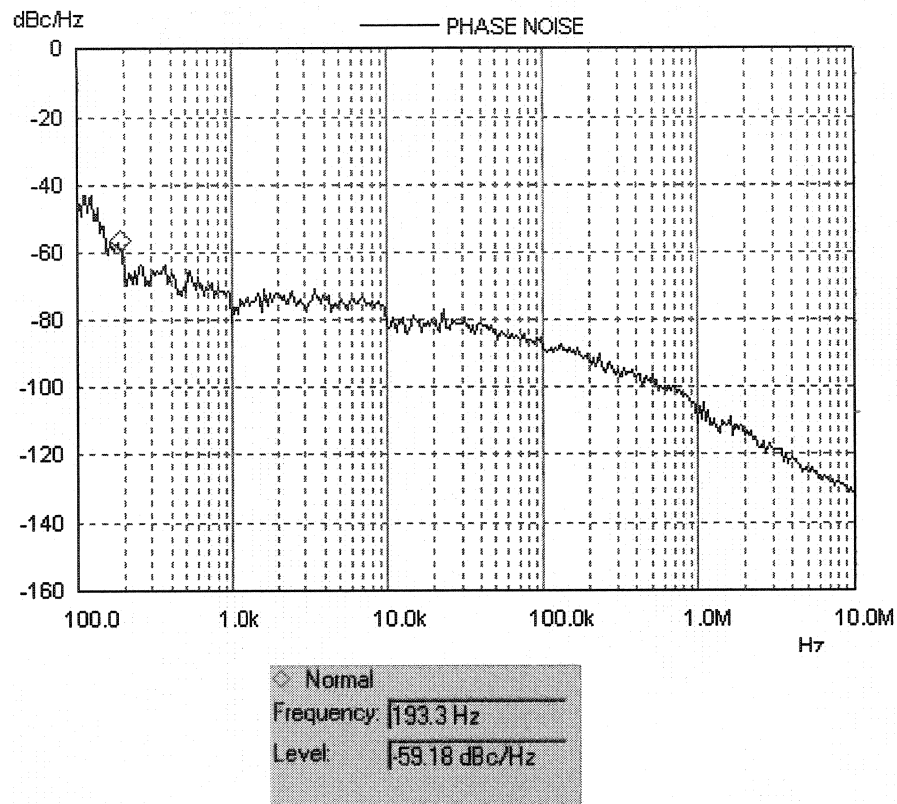


Figure 3-11: Phase noise oscillator's performance

As shown in Figure 3-11, we have a level of -59 dBc/Hz was obtained at 193.3 Hz from the carrier.

### 3.5 Injection Locking

Injection locking is the result of applying an external RF signal to the input of a free running oscillator to obtain a frequency change of the original signal; in other words, it is a shift or lock to the frequency of the injected signal. The purpose of such procedure is to obtain a more stable oscillator at a particular frequency, and to contribute to reducing the spurious oscillations and the phase noise.

Van del Pol [30] made some of the most relevant contributions to this field, in the 1920s. In 1946 Adler [1] developed the theory of injection locking in electrical

oscillators, and in 1973 Kurokawa [18] developed the theory of negative resistance injection locked oscillators.

The decision of using the Injection locking technique in this research was taken because it provides a straightforward procedure to reduce the phase noise and improve the stability of our oscillator. Even though the free running frequency of our oscillator is the desired one, injection locking allows to shift the frequency and, more importantly, to reduce the levels of AM, FM and PM noise.

The concept of the Injection locking technique is actually very simple: an external signal is injected into the oscillator by coupling or mixing devices. The external source must be a very clean and stable signal, 10 dB lower in power than the output power of the oscillator. The injected signal will command the oscillator in the sense that it will control its resonant frequency and phase.

One of the parameters that can measure the performance of the injection locking scheme is the injection locking bandwidth, as the frequency range in which the injection locking will not break. In other words, the output signal is free of spurious frequency and noisy spectrum. In our case the Locking bandwidth is around 4 MHz with an injected signal of -15 dBm; increasing the injected signal power will result in better injection bandwidth, but more energy will be needed from the local oscillator.

As shown in Figure 3-5, a coupled line with a coupled factor of -17dB terminated in a 50  $\Omega$  resistance was used to inject the locking signal in our circuit.



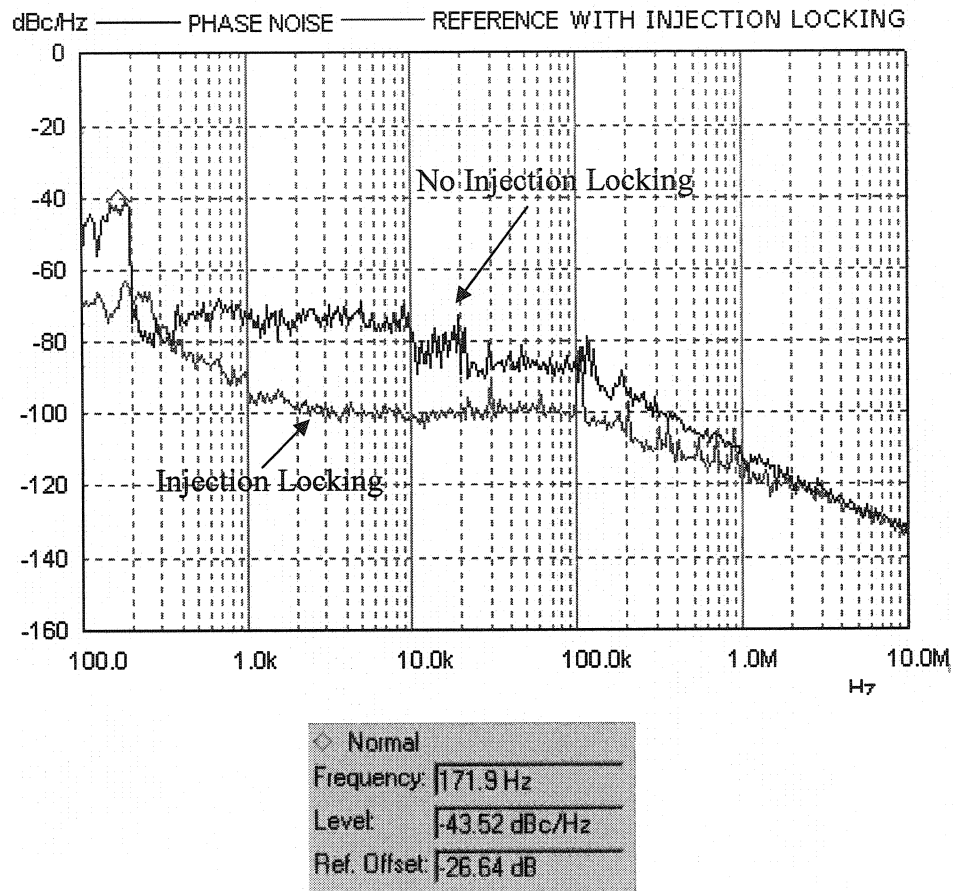


Figure 3-12: Phase noise performance using Injection locking

Figure 3-12 shows how the phase noise of our oscillator is improved by using the injection locking scheme. At first, a level of -43.52 dBc/Hz was obtained at 171.9 Hz from the carrier, and with injection locking a level of -70.16 dBc/Hz was gotten at the same frequency point. This means an improvement of 26.6 dB.

So far, some key concepts in oscillator design have been explained, as well as the procedure to develop an oscillator using SIW technology. Simulations results and measurements performed to our prototypes have also been presented. Finally, this Chapter showed how to obtain a low phase noise oscillator with a RF output power of 15 dB, and with temperature stability of 6 ppm/°C.

## CHAPTER 4. POWER SOURCE

In today's world the use of solid-state amplifiers is very common among communication and RADAR systems. In some applications the need for medium and high power sources constrains the design process. To overcome this challenge, power combiners are used to increase the power generation capabilities.

### 4.1 Fundamental theory

The idea of combining two or more devices and obtaining a high power output looks simple at first sight. One can assume that a power combination will be obtained by interconnecting the output of each device, but several considerations have to be taken into account in order to achieve an optimal performance without endangering each one of the devices. Some of the most important factors in power combining techniques are the isolation between devices, the frequency stability, the phase of each signal, and the amplitude.

Gonzales [13] clearly explains that paralleling several amplifiers to achieve high power output is not an optimal method to use, and his analysis can be extended to the case of several oscillators. Some of the reasons that sustain this statement are:

- The input and output impedance levels can be of the same order as the losses in the input and output matching networks. For this reason, the total output power that can be obtained from several paralleled oscillators is lower than the theoretical total output power, because the efficiency decreases as the number of oscillators increases.
- If one of the oscillators fails, the complete network fails.
- All oscillators must be perfectly matched to obtain good load sharing and maximize the output power.

As a possible solution to some of the problems above, Gonzalez suggests using a Hybrid divider and a Hybrid combiner to equally divide the input power among several amplifiers and then combine the output power of each amplifier. Using this technique assures that the network will continue to work with reduced power output in case of failure of one of the amplifiers. Another advantage is that the amplifiers are in a way isolated from one to another, so that the impedance matching of each device is not an issue anymore.

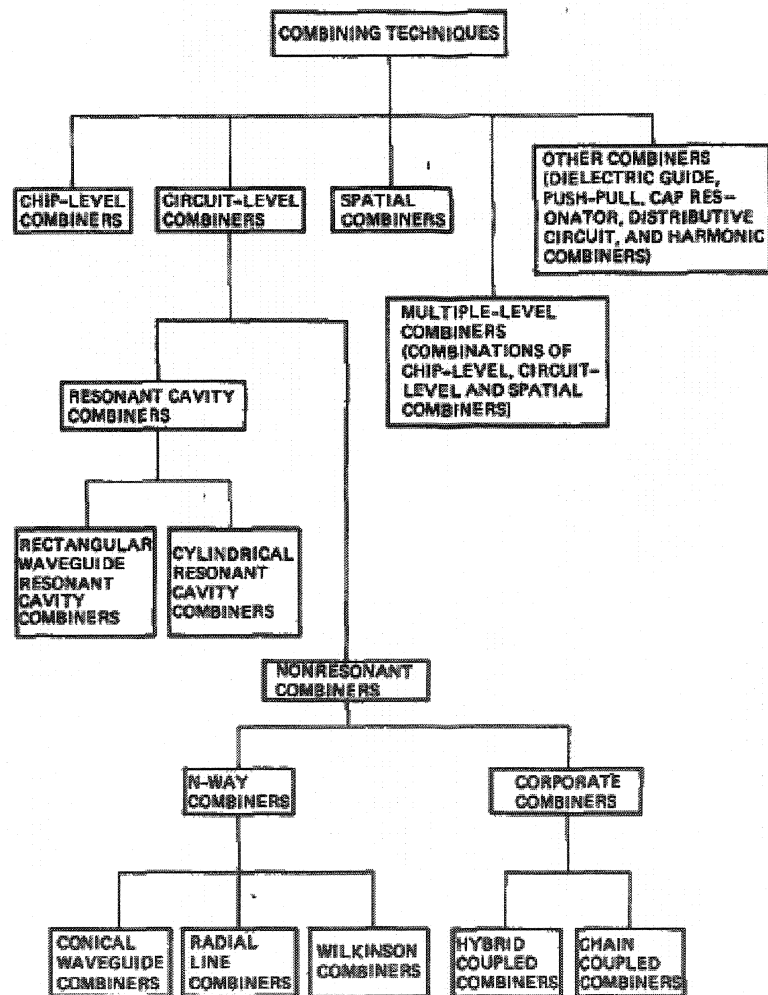


Figure 4-1: Different combining techniques (Source: [6])

There are different levels in the output power combination of several devices:

- Chip level: The outputs from two or more device chips are combined in a compact manner.
- Circuit level: Device outputs are combined using microwave circuits elements like waveguides or planar transmission lines. These combiners can be subdivided into resonant combiners, which house the devices in a waveguide cavity, and non-resonant combiners, which use couplers or circulators to make the power combination.
- Spatial: Combine the output of several oscillators in free space.
- Multi-level: Uses two or more of the above combining techniques to combine the outputs of others combiners.

Our interest is focused on the circuit level power combiners. The advantages and disadvantages of the resonant cavity combiners and non resonant combiners are:

Resonant cavity combiner's advantages:

- High combining efficiency, because the outputs of the devices combine in a relative small region, reducing the transmission line losses.
- Compact size.
- The devices tend to injection lock each other during the operation, making a stable operation.

Resonant cavity combiner disadvantages:

- Narrow bandwidth.
- Electrical tuning is complex.

Non-resonant combiner's advantages:

- Operate over a wider bandwidth than resonant combiners.
- Are very convenient when it comes to combine working oscillators, since the devices are isolated.

Non-resonant combiner's disadvantages:

- The devices must be identical in their electrical characteristics to achieve a single frequency of operation.
- They tend to have transmission losses due to the physical construction of the devices.

## 4.2 Power combiner using a T junction based on SIW technology

The SIW power combiner used in this project can be classified as a resonant power combiner since it has almost the same propagation properties of a typical waveguide. Furthermore, the fact that the isolation at ports 2 and 3 is low, as will be proven in later analysis, suggests that there is injection locking between the two oscillators. At the same time, the structure can be classified as non-resonant because the T-junction has some of the characteristics of a Wilkinson combiner.

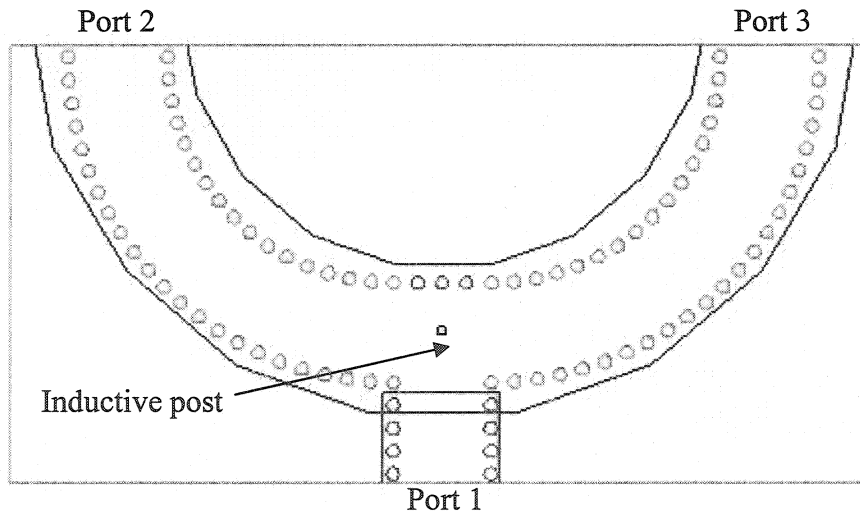


Figure 4-2: Power combiner using a T-junction structure

As explained by Germain in [12], the use of SIW power dividers reduces the constructions problems due to transitions between waveguide and micro strip lines, and

simplifies the design process by using the same substrate. According to Germain, the performance of a SIW power combiner is comparable with its counterpart using the traditional waveguide.

In our case the structure chosen is a T-junction. The addition of the inductive post allows to achieve low return losses at the input port. The T-junction structure has been proposed by Hirokawa [14] and has been studied over the last 15 years. As commented in [12] the position and the diameter of the inductive matching post affect the return loss at the fundamental frequency and are subject to optimization.

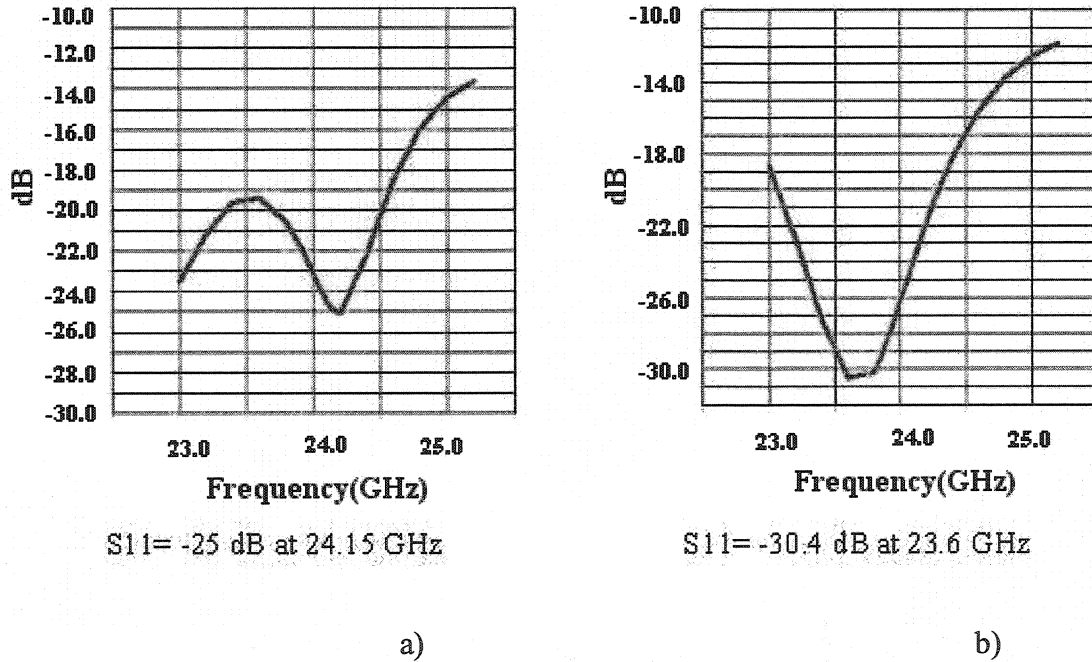


Figure 4-3: Insertion loss of the T power combiner. a) The inductive post diameter is 0.58 mm, and is located in the center of the T junction  $(x,y)=(0,0)$ ; b) The inductive post diameter is 0.78 mm, and is located at  $(x,y)=(0,9)$ .

The position and the diameter of the inductive post is a key factor to improve the performance of the power combiner, as shown on Figure 4-3. After an optimization process using the simulations tool HFSS [33], a suitable configuration was obtained. Figure 4-4 shows,  $S_{11} = -35$  dB;  $S_{13} = -3.4$ ;  $S_{22} = S_{33} = -6.7$  dB at 24.2 GHz.

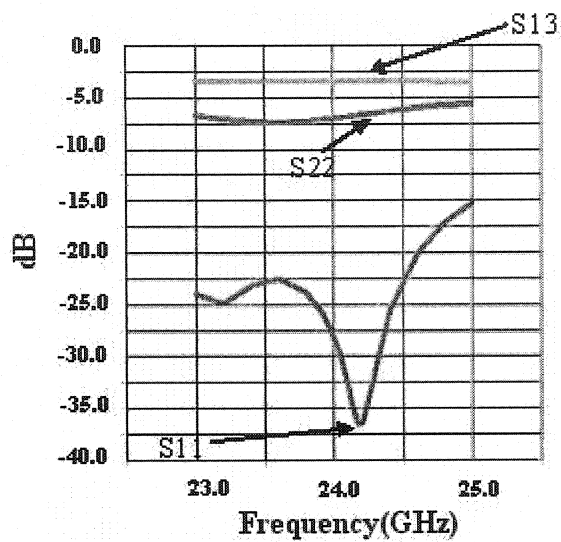


Figure 4-4: T junction power combiner S parameters.

### 4.3 Power source design

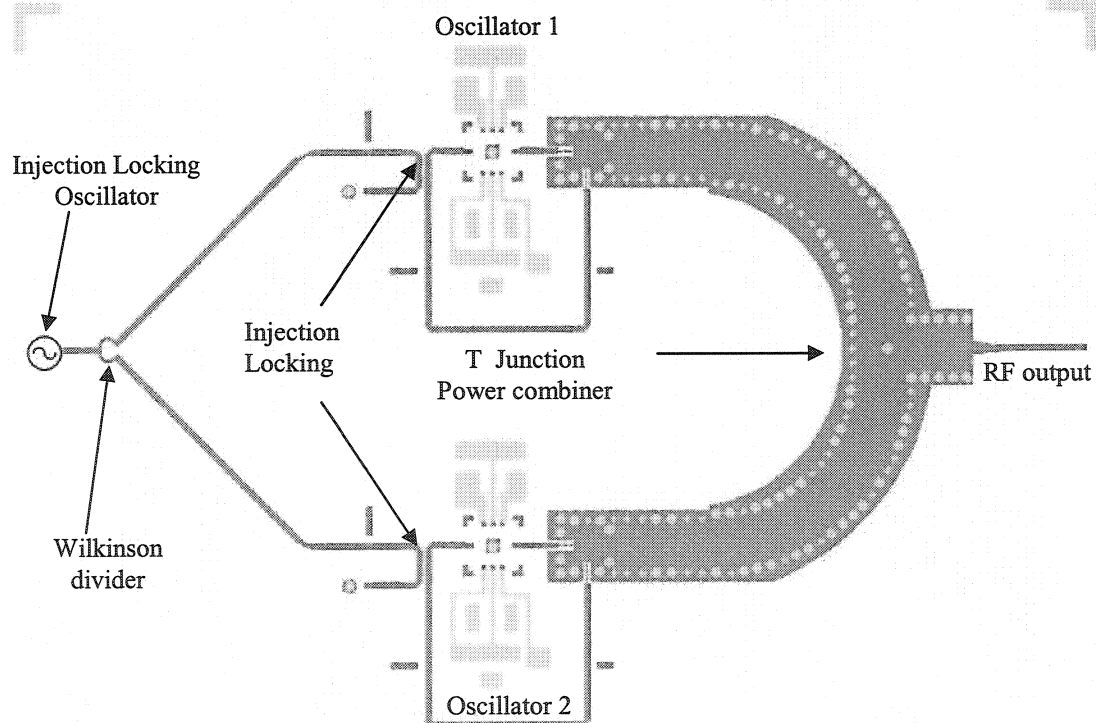


Figure 4-5: Power source layout

So far, the design and performance of a T junction power combiner have been explained; the next step is to bring together the power combiner and the oscillators to create a RF power source.

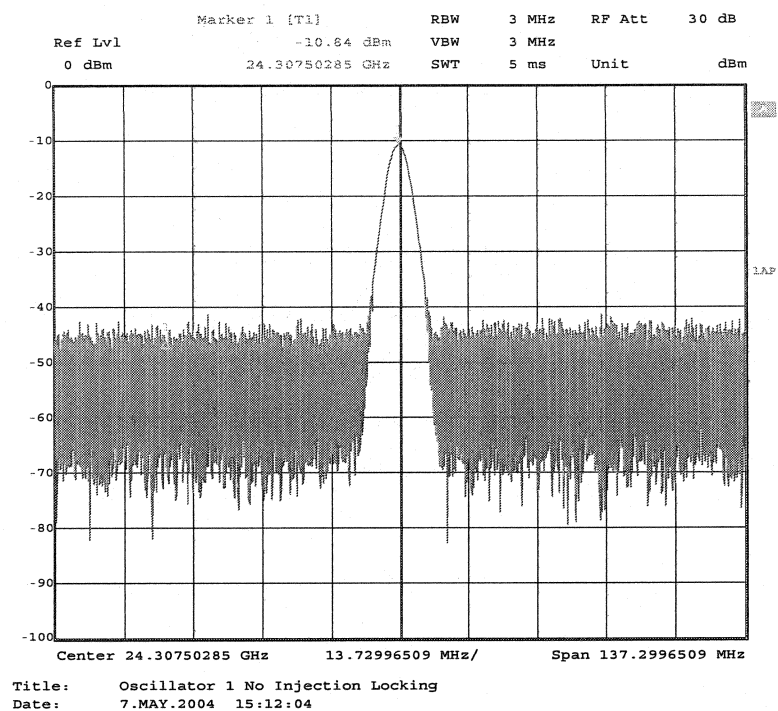
Figure 4-5 presents the power source layout, where two identical oscillators were used to generate the same frequency. Both oscillators are synchronized using the injection locking scheme. The injection locking signal has a coupling factor of -17 dB and a Wilkinson divider is used to equally split the signal. By doing so we are forcing the RF output of each oscillator to be as similar as possible.

A phase mismatch on one of the oscillators will be reflected on the quality of the output signal and will introduce standing waves on the power combiner that spoil the RF output and degrade the signal.

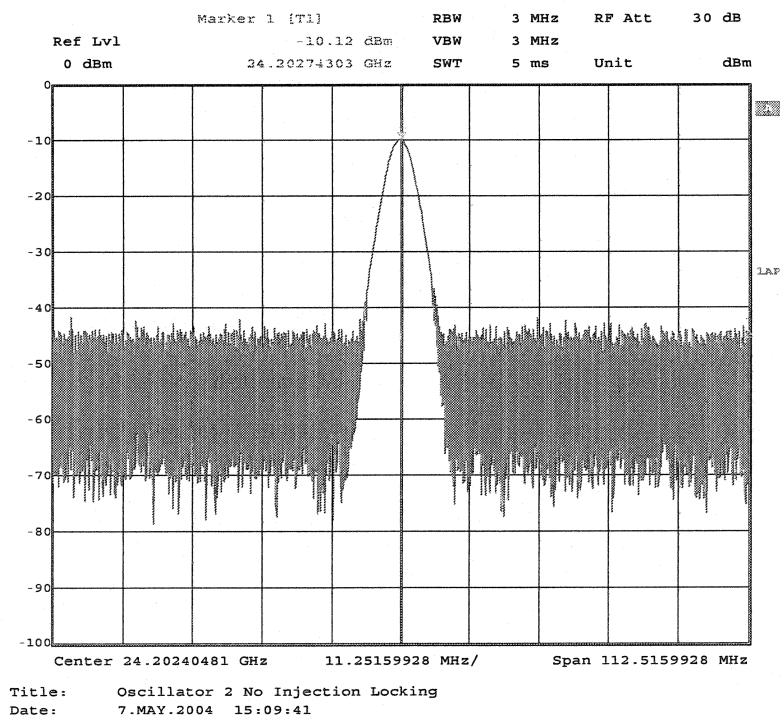
#### **4.3.1 Measurement results**

Figure 4-6 shows the performance of oscillator 1 when oscillator 2 is not polarized, and vice versa. It can be noted that the resonant frequency  $f_0$  of both oscillators is slightly different in the order of few MHz due to fabrication errors. The output signal is in the range of -10.2 dBm, it must not be forgotten that -20.5 dB attenuator is used at the source output to protect the spectrum analyzer. It should also be considered that the loss due to the interconnection cable is -2.5dB, so the real output of each oscillator is 12.8 dBm.





a)  $f_o = 24.3075$  GHz



b)  $f_o = 24.2027$  GHz

Figure 4-6: Resonant frequency: a) Oscillator 1, b) Oscillator 2

As shown in Figure 4.7, when combined together the output is -7.29 dBm, and by adding the attenuator and the cable losses the real output becomes 15.71 dBm. Therefore, the gain of the power combiner is 2.9 dBm, as expected according to the theory.

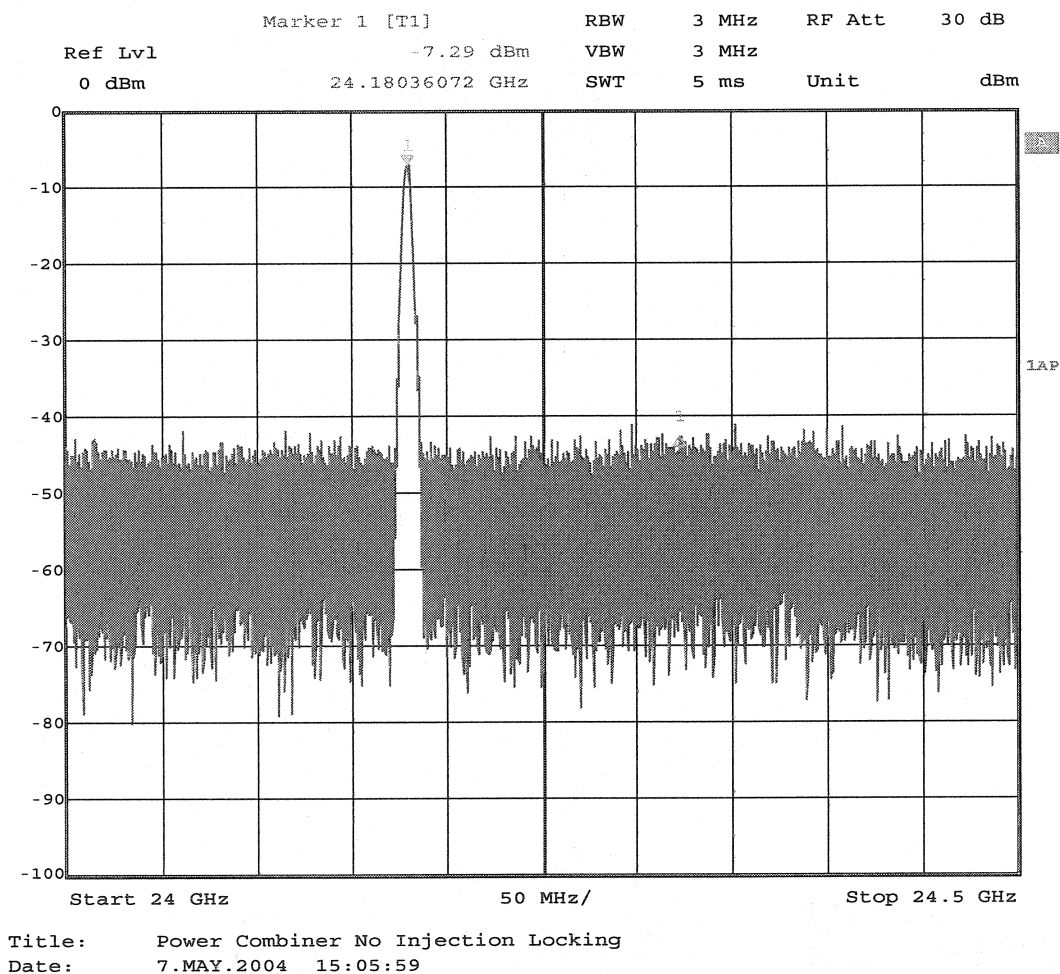


Figure 4-7: Output power combiner

### 4.3.2 Power combiner phase noise

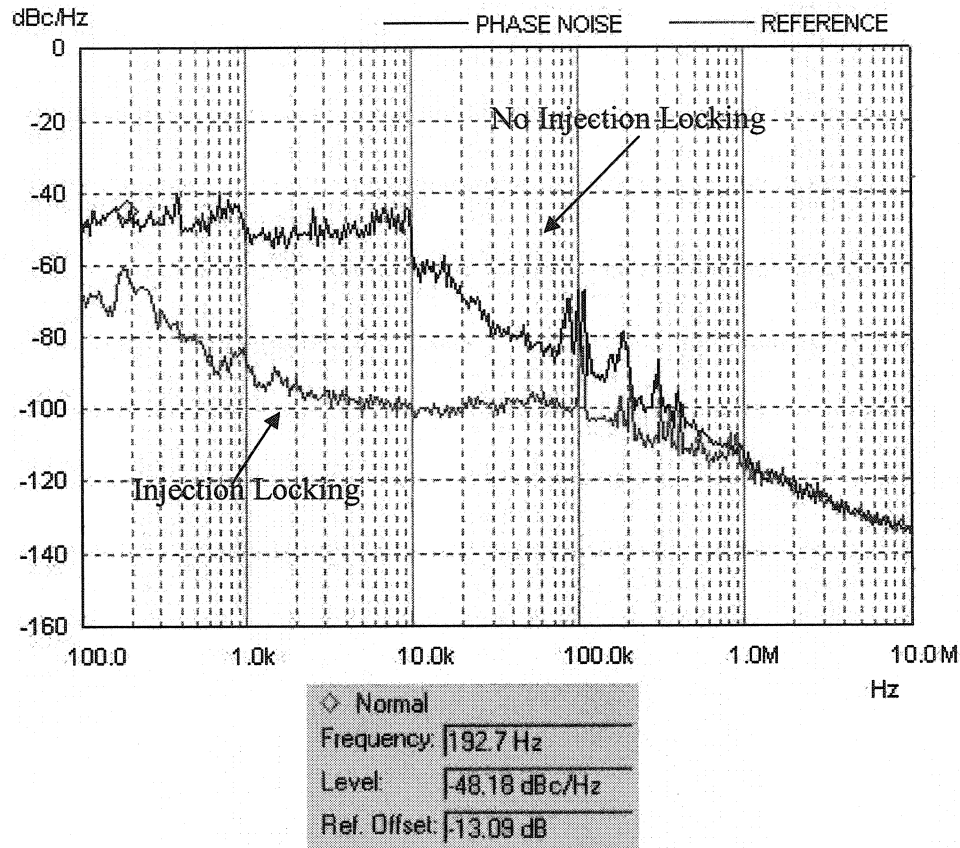


Figure 4-8: Power source phase noise

Figure 4-8 shows how the power combiner phase noise has improved by using the injection locking scheme. A level of -48.18 dBc/Hz was obtained at 192.7 Hz from the carrier. By using injection locking, a level of -61.67 dBc/Hz was achieved at the same frequency point, a result that shows an improvement of 13.09 dB. The injection locking signal was obtained from a stable microwave signal generator ARINTSU M6394A. An additional benefit of using injection locking is having the capacity to control the resonant frequency without affecting either the output power or the phase noise over a bandwidth of 4 MHz.

### 4.3.3 Temperature performance

As discussed in Chapter 3, Section 3.4.3, the temperature is a very important factor that helps measure an oscillator's performance and, allows the measurement of the power combiner's performance, as in this case.

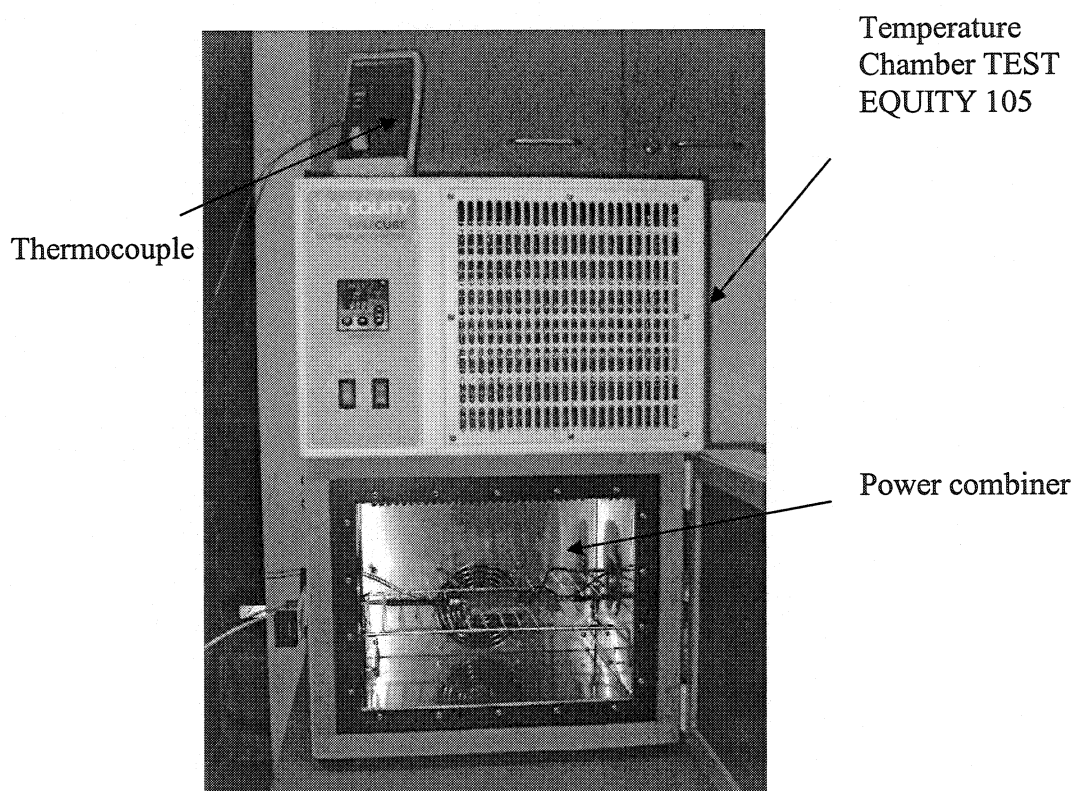


Figure 4-9: Temperature set up for the power combiner

Table 4-1 summarizes the measures under different conditions of the power source, such as the amplifier's polarization point, the resonant frequency, and the output power amplitude. Due to physical constraints the local oscillator can not be fitted inside the temperature chamber. It is assumed that the local oscillator is very stable with temperature changes; therefore, the measurement results reflect only the behavior of the power combiner with temperature, discarding the influence over the local oscillator.

Thermocouple	Chamber Temperature	I dd mA		Freq(Ghz)	Amp(dBm)
		Osc1	Osc2		
-30.0°C	-30°C *	140	340	24.190420	-6.7
-19.4°C	-20°C	120	336	24.189795	-6.8
-10.0°C	-10°C	120	319	24.185968	-6.5
-0.6 °C	0 °C	120	330	24.184343	-6.5
10.3°C	10°C *	120	327	24.183512	-6.5
22.0°C	20°C	120	318	24.182356	-6.2
32.2°C	30°C	120	312	24.181059	-7.43
41.4°C	40°C	120	305	24.179039	-6.97
51.0°C	50°C *	120	299	24.177690	-7.02

Table 4-1: T-junction Power combiner temperature performance.

*Note:* On the ones marked with \* the injection locking bandwidth has been verified and the results are as follows:

- With Injection locking at 50°C  $f_0 = 24.17769$  GHz, level of injection -12.5 dBm  
Displacement to the right  $f_0 = 24.179639$  GHz  
Displacement to the left  $f_0 = 24.17544206$  GHz  
The injection locking bandwidth is 4.19 MHz
- With Injection locking at 25.3°C  $f_0 = 24.179639$  GHz level of injection -12.5 dBm  
Displacement to the right  $f_0 = 24.181738$  GHz  
Displacement to the left  $f_0 = 24.177840$  GHz  
The injection locking bandwidth is 3.89 MHz
- With Injection locking at 10°C  $f_0 = 24.183510$  GHz, level of injection -12.5 dBm  
Displacement to the right  $f_0 = 24.18055$  GHz  
Displacement to the left  $f_0 = 24.177308$  GHz  
The injection locking bandwidth is 3.24 MHz

- With Injection locking at  $-30^{\circ}\text{C}$   $f_0 = 24.190289$  GHz, level of injection  $-12.5$  dBm  
 Displacement to the right  $f_0 = 24.19191$  GHz  
 Displacement to the left  $f_0 = 24.18826$  GHz  
 The injection locking bandwidth is  $3.65$  MHz

Figure 4-10 represents the frequency variation with temperature.

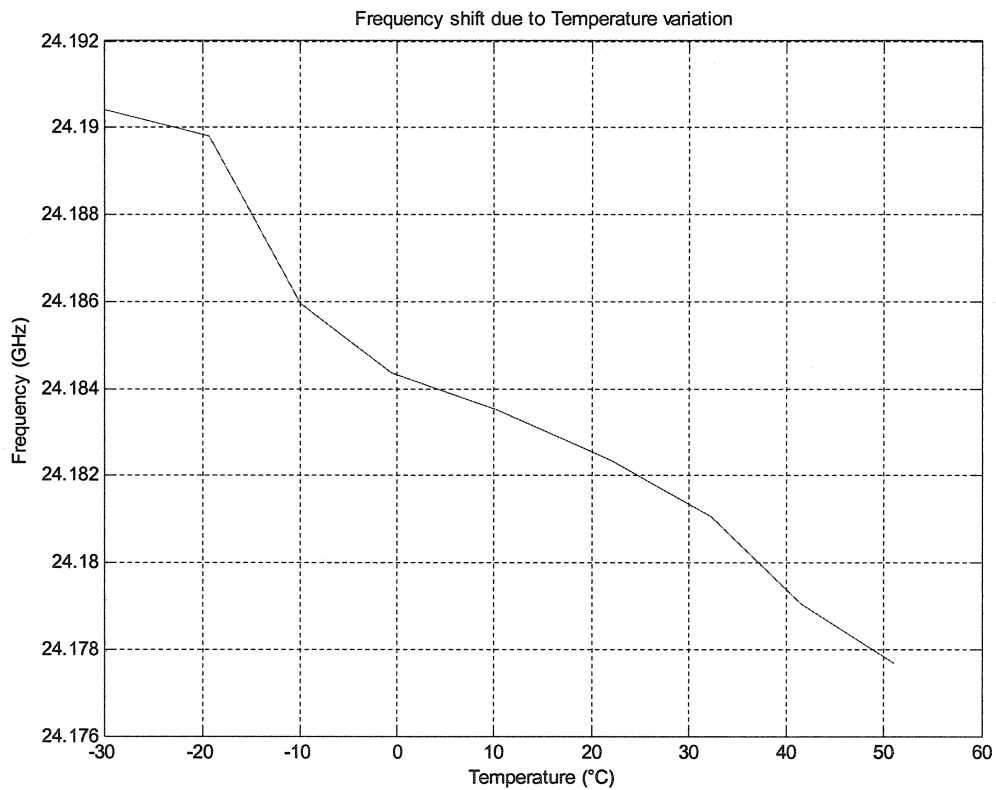
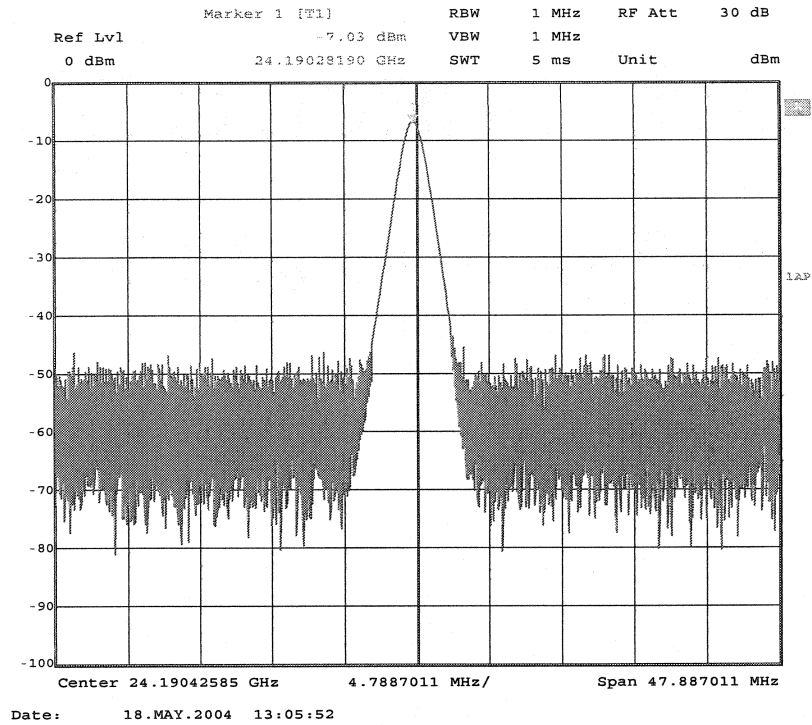
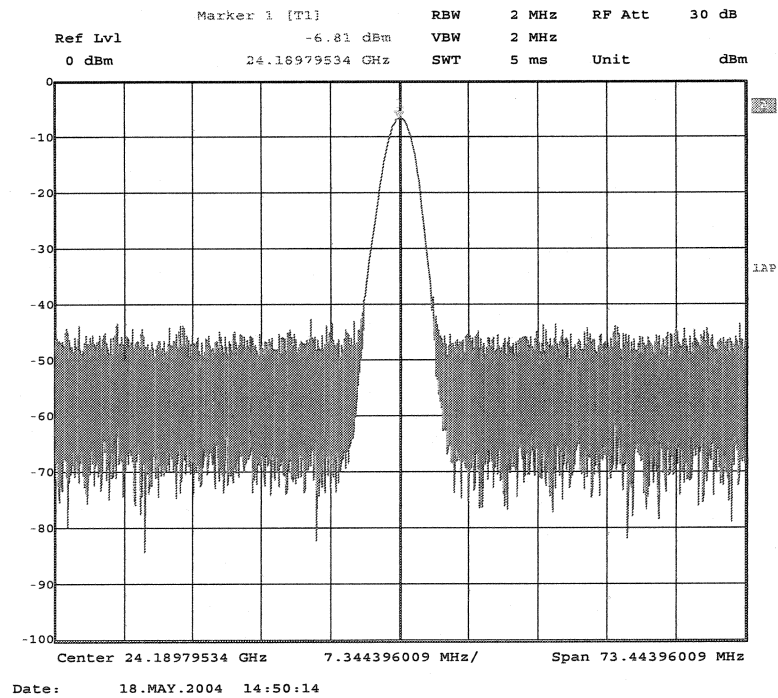


Figure 4-10: Frequency variation with temperature on the T-junction power combiner

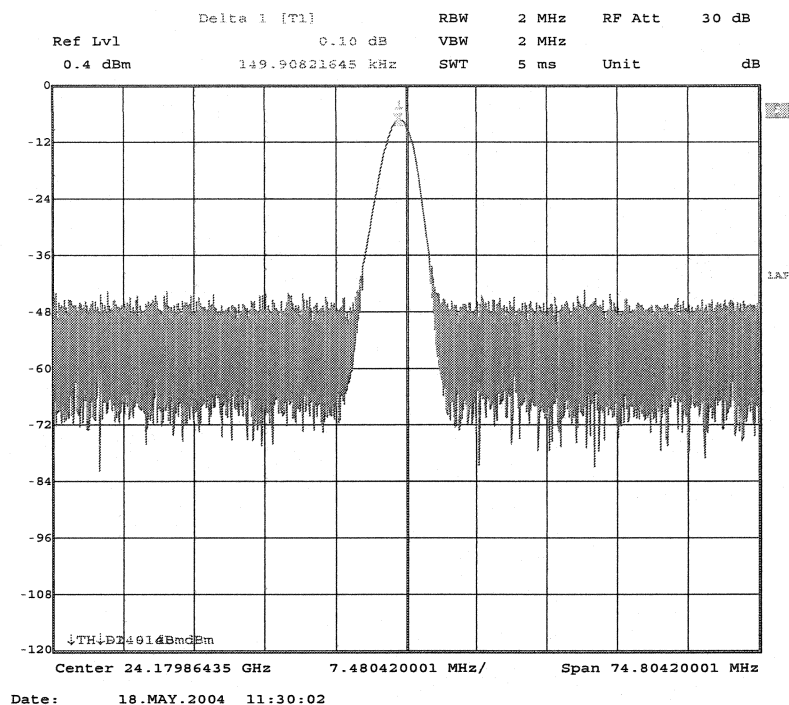
Based on the obtained data one can conclude that the injection locking bandwidth is not affected by temperature.



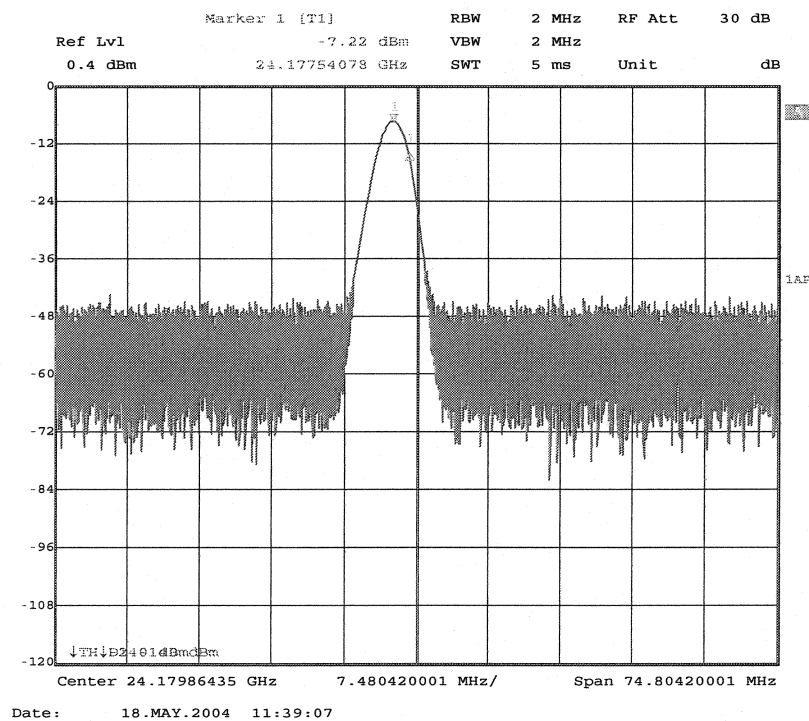
a)  $f_o = 24.19042$  GHz at  $-30^\circ\text{C}$



b)  $f_o = 24.18979$  GHz at  $-20^\circ\text{C}$



c)  $f_o = 24.17903$  GHz at 40°C



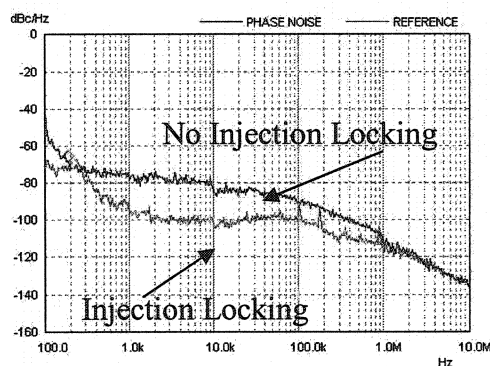
d)  $f_o = 24.17769$  GHz at 50°C

Figure 4-11: Power combiner temperature measurements results.

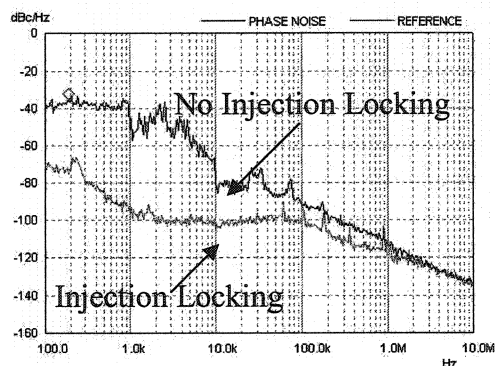


Figures 4-10 and 4-11 show the power combiner frequency response at different temperatures. As temperature increases, the resonant frequency decreases as expected, because the heating tends to dilate the cavity.

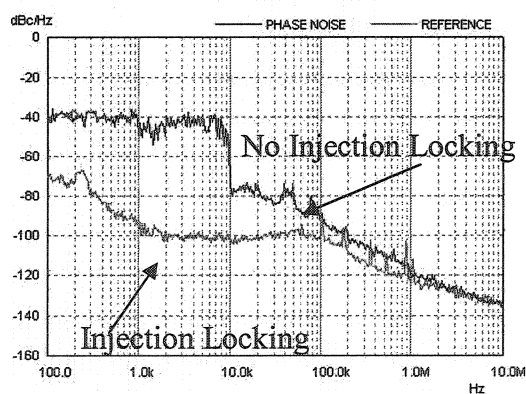
Figure 4-12 shows the phase noise performance under different temperature conditions: with no injection locking signal, at 100 Hz from the carrier a phase noise level of -40 dBc/Hz was obtained. A small difference between 1 KHz and 100 KHz from the carrier can also be perceived. The phase noise signal remains almost constant as temperature varies.



Phase noise at -30°C



Phase noise at 10°C



Phase noise at 50°C

Figure 4-12: Phase noise behavior with temperature variation

To calculate the temperature stability in ppm/°C equation 3.4.1 was used along with data from Table 4-1. The result, 6.57 ppm/°C, reveals that our oscillator is very stable and temperature changes do not affect its performance.

#### 4.4 Coupling effects over power combiner performance

Even though the S-parameters of the power combiner shown in Section 4.2 are remarkable in terms of return loss and insertion loss, the isolation at ports 2 and 3 is a key factor on the performance of the power combiner. Since there is a low isolation at ports 2 and 3,  $S_{22} = S_{33} = -6.7\text{dB}$ , and the oscillators are not equally liked, there will be a dynamic interrelation between the devices. Such factor will lead to make the stability of the circuit unpredictable because each oscillator introduces an impedance change on the output of its counterpart.

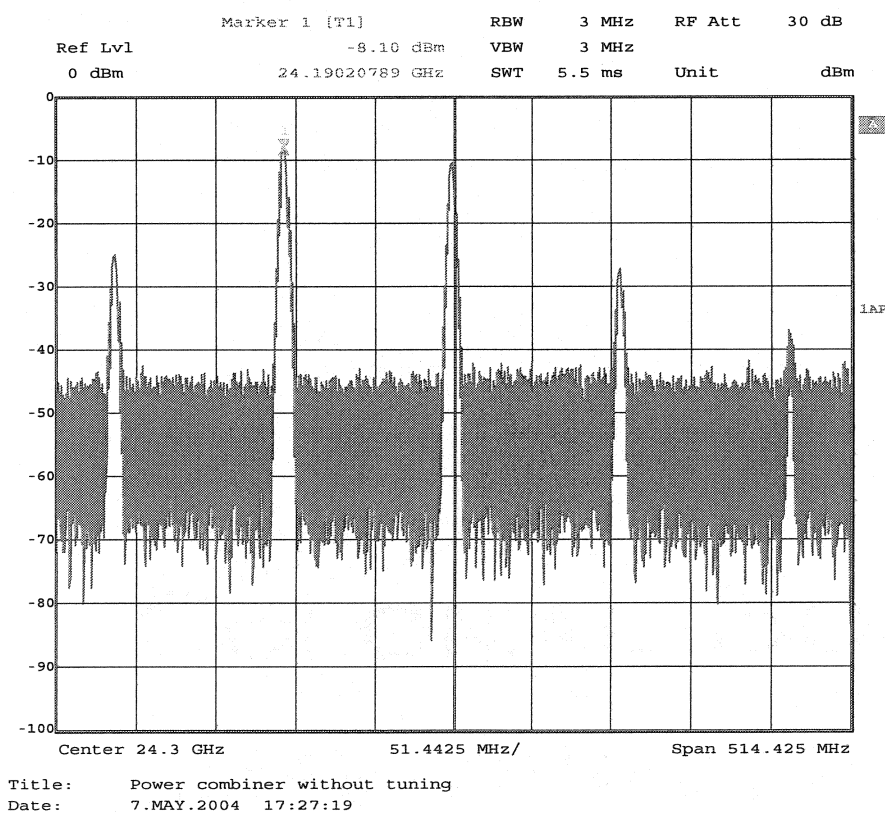


Figure 4-13: Power source without tuning

Figure 4-13 shows five different resonant frequencies, suggesting that there is an interrelation between oscillators. This phenomenon occurs during the polarization process due to the impedance changes on the circuit. Just after arriving to the optimal polarization parameters for each oscillator, a perfect power combination was obtained. Using a T-junction to combine the output of two oscillators suggests the need of a resistance. Such is the case of the Wilkinson combiner, where the resistance absorbs the reflecting RF energy generated by the adaptation mismatch on ports 2 and 3.

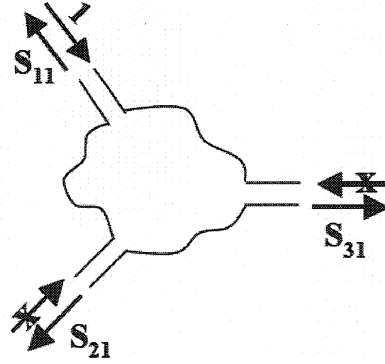


Figure 4-14: Adaptation of a 3-ports device

To better explain this phenomena let us assume a 3-ports device, as in figure 4-14. To adapt all 3 ports at the same time without losses, the following condition should be fulfilled:

$$S \cdot S^{*T} = I \quad (4.4.1)$$

The matrix multiplication of Eq. 4.4.1 is:

$$\begin{pmatrix} 0 & S_{12} & S_{13} \\ S_{12} & 0 & S_{23} \\ S_{13} & S_{23} & 0 \end{pmatrix} \cdot \begin{pmatrix} 0 & S_{12}^* & S_{13}^* \\ S_{12}^* & 0 & S_{23}^* \\ S_{13}^* & S_{23}^* & 0 \end{pmatrix} = \begin{pmatrix} 1 & 0 & 0 \\ 0 & 1 & 0 \\ 0 & 0 & 1 \end{pmatrix} \quad (4.4.2)$$

Eq. 4.4.2 suggests that

$$|S_{12}|^2 + |S_{13}|^2 = 1 \quad (4.4.3)$$

$$|S_{12}|^2 + |S_{23}|^2 = 1 \quad (4.4.4)$$

$$|S_{13}|^2 + |S_{23}|^2 = 1 \quad (4.4.5)$$

As it is known  $|S_{13}| \cdot |S_{23}|^* = 0$  and that means that either  $S_{13} = 0$  or  $S_{23} = 1$  so, if the first statement is added to Eq. 4.4.3,  $|S_{12}| = 1$  and if this result is applied in Eq. 4.4.4 the following inconsistency is obtained:

$$\begin{aligned} 1^2 + 1^2 &= 1 \\ 2 &= 1 \end{aligned} \quad (4.4.6)$$

Eq. 4.4.6 proves that a 3-ports device can not be adapted at the same time without losses.

The results obtained with the T-junction power combiner encouraged the research for a better solution. The possibility of building the power combiner using a 90° Hybrid coupler was then considered.

#### 4.5 Power combiner using a 90° Hybrid coupler

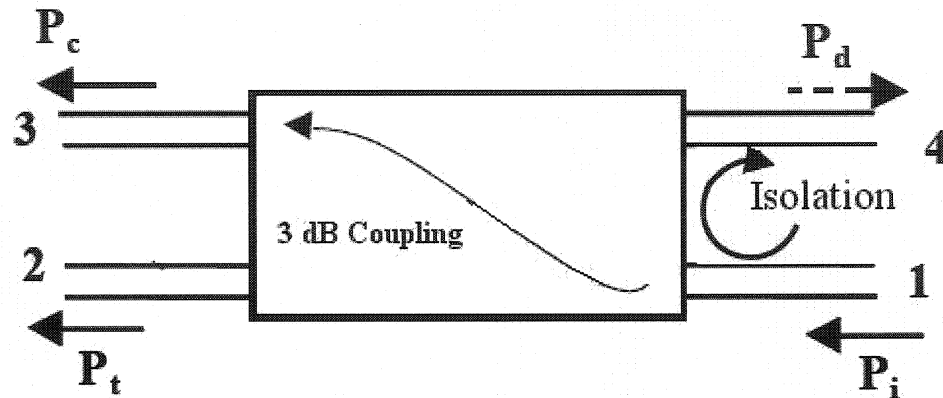


Figure 4-15: 90° Hybrid coupler.

The classic model for the 90° hybrid coupler is shown in figure 4-15, where  $P_c$  is the coupled power,  $P_t$  is the transmitted power,  $P_i$  is the input power and  $P_d$  is the dissipated power. This structure is a 3dB coupler that provides an excellent isolation between port 1 and 4.

##### 4.5.1 The 90° Hybrid coupler as a combiner

As proposed by Chang and Sun [6], it is possible to use the hybrid coupler as a power combiner and, at the same time, use the injection locking technique to obtain a stable power source. To better understand the behavior of the 90° Hybrid coupler as a combiner Figure 4-15 is redrawn into Figure 4-16.

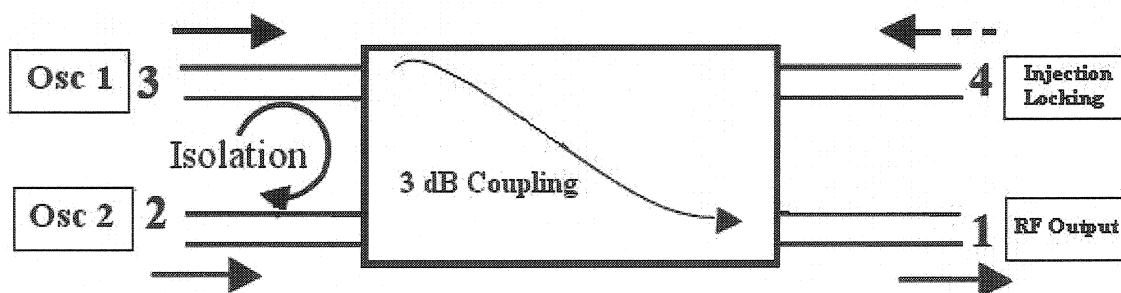


Figure 4-16: 90° Hybrid power combiner.

If the locking signal is applied to port 4, the output is received at port 1. The hybrid coupler is designed so that the port 4 signal power will be evenly split between ports 2 and 3. The distance from port 1 to port 3 is chosen so that the signal received at port 3 is  $90^\circ$  behind in phase from the signal received at port 2. The coupler is designed so that port 1 receives no power from port 4. The coupler behaves identically when power is applied at any of the others ports. For instance, if a signal is applied at port 2, it is evenly split between ports 1 and 4 with no power received at port 3.

Ports 2 and 3 are terminated with identical oscillators. Each oscillator amplifies and reflects its half of the locking signal. The signal reflected from the oscillator at port 2 splits evenly between ports 1 and 4, but the phase of the signal at port 1 is  $90^\circ$  behind in phase of the signal at port 4.

Consider the locking signal at port 4 to have  $0^\circ$  phase, then the signals received at ports 2 and 3 have phases  $\theta-90$ . Assuming that these signals are reflected without phase change, then two signals are received at port 1 and at port 4. The phase angles of the signals received at port 1 are both  $2\theta-90$ , so that the oscillator signals add at port 1. The phase angles of the signals received at port 4 are  $2\theta$  and  $2\theta-180$ ; the signals at port 4 cancel.

To prove the theory above explained an ADS simulation was conducted using ideal components.

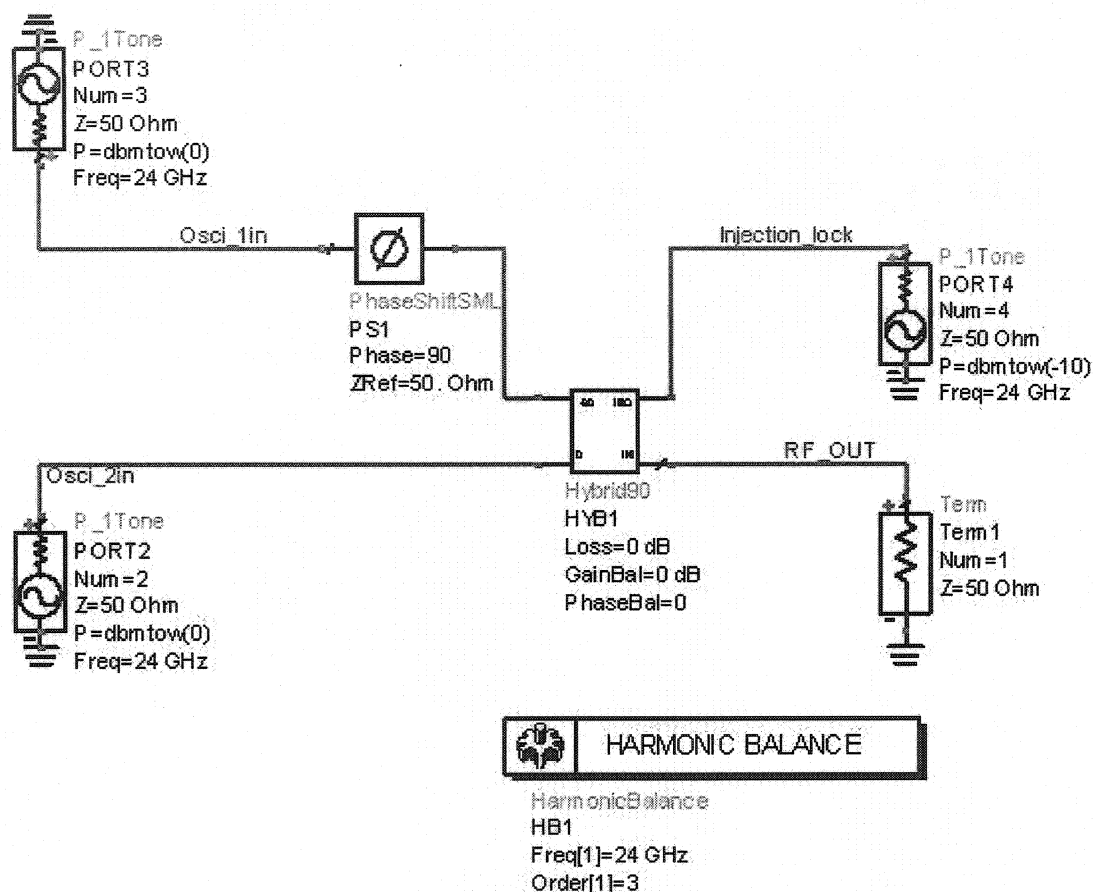


Figure 4-17: ADS schematic of the 90° Hybrid power combiner

On Figure 4-17 two ideal oscillators with an output power of 0 dB have been connected at ports 2 and 3. It is possible to see that oscillator 1, located on port 3, has a 90° phase shift to assure the in phase with the signal of oscillator 2 at port 1. At port 4 an ideal oscillator was added to provide the injection locking signal with an output power of -10 dB.

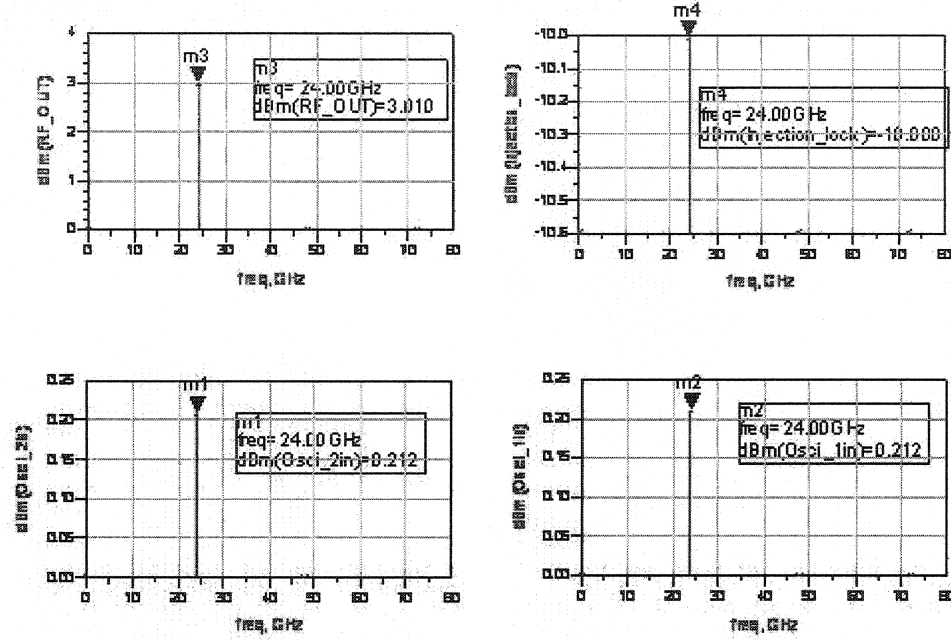


Figure 4-18: 90° Hybrid power combiner simulation results

Figure 4-18 shows a RF output of 3 dBm at port 1. The oscillator's signals are 0.212 dBm because a signal equal to -10dBm has been injected at port 4 and divided between ports 2 and 3. From the simulation results it can be concluded that the Hybrid power combiner behaves as predicted by the previous theoretical analysis.

Nervarez and Herkowitz [22] demonstrated that the output power and phase of a hybrid combiner are given by:

$$P_r = \frac{1 + 10^{D/10} + (2 \cos \theta) 10^{D/10}}{2} \quad (4.5.1)$$

$$\theta_r = \tan^{-1} \frac{10^{D/10} \sin \theta}{1 + 10^{D/10} \cos \theta} \quad (4.5.2)$$

Where D is the difference in insertion loss (in dB) for the two paths of the hybrid.



The signals at ports 2 and 3 are equal in amplitude when the condition of a 3 dB power split is fulfilled; so  $D = 0\text{dB}$ ;  $\theta$  is the phase deviation from the correct  $90^\circ$  phase difference between the two paths. In a real combiner, amplitude and phase deviation are caused by the different characteristics of the oscillators in addition to the non-ideal characteristics of the 3-dB hybrid coupler. The combining efficiency of the combiner is given by:

$$\eta_c = \frac{P_T}{P_{in}} = \frac{1 + 10^{D/10} + (2 \cos \theta) 10^{D/20}}{2(1 + 10^{D/10})} \quad (4.5.3)$$

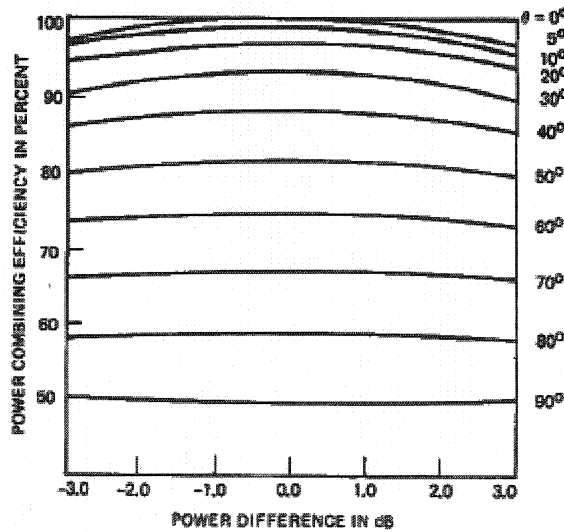


Figure 4-19: Power combiner efficiency of Hybrid-coupler combiner. *Source:* [6]

The phase error has the primary effect on the combining efficiency. Figure 4-19 shows that a combining efficiency greater than 90% can be maintained for a 6 dB variation in amplitude error, as long as the phase deviation does not exceed  $30^\circ$ .

To quantify the output signal degradation due to the phase mismatch several ADS simulation were conducted using the same schematic on Figure 4-17, but this time a  $70^\circ$  phase shift was introduced instead of a  $90^\circ$ , which means we have a  $20^\circ$  mismatch.

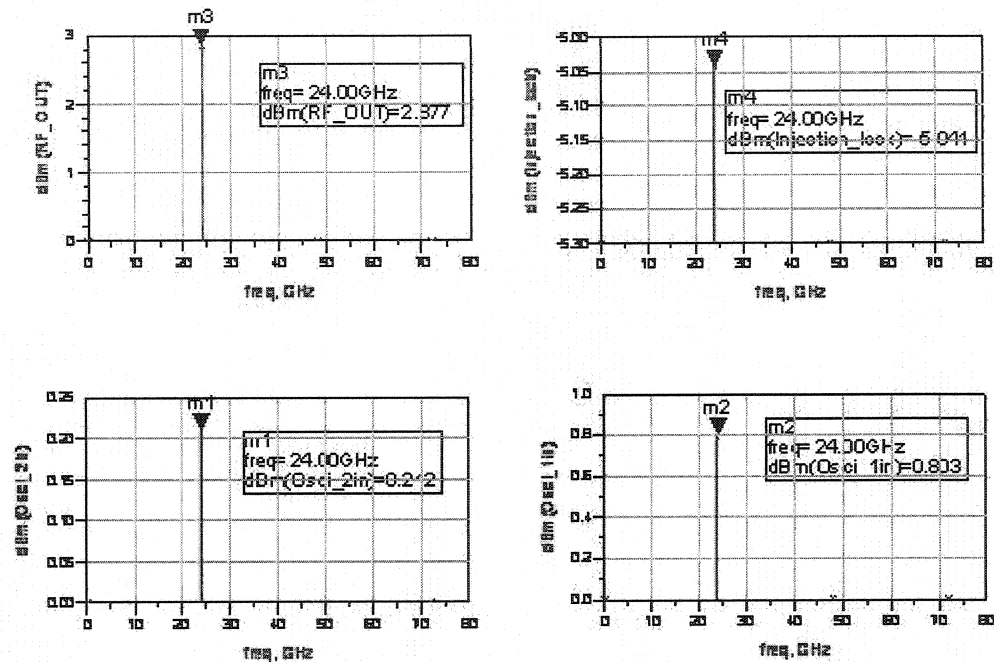


Figure 4-20: 90° Hybrid power combiner simulation results with 20° mismatch between oscillators.

As the phase mismatch is introduced, Figure 4-20 shows an RF output signal of 2.87 dBm. It can also be seen that the oscillator signals are not longer in balance, and the power level at the injection locking port has changed from -10 dBm to -5.011 dBm, which implies a reflected signal at port 4. Results previously presented confirm that a phase mismatch will deteriorated the output signal quality.

### 4.5.2 Mathematical derivation

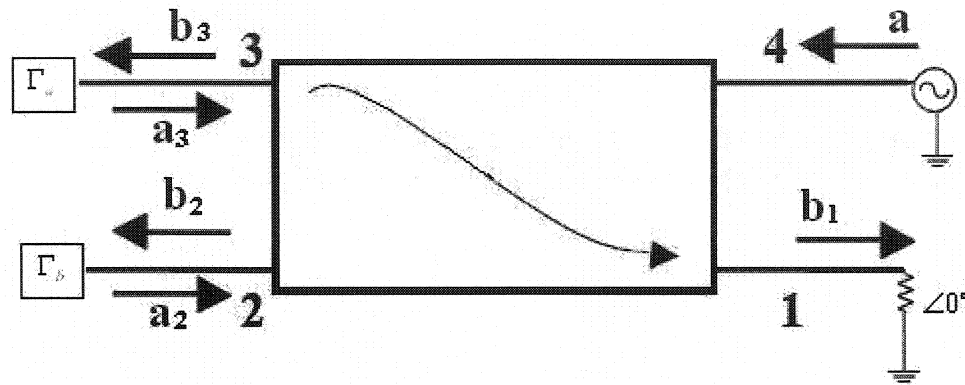


Figure 4-21: Hybrid coupler incident and reflected waves.

The hybrid combiner can be analyzed using the incident and the reflected waves that travel along the device, to find an expression that shows the contribution of each oscillator at port 1. The oscillators at port 2 and port 3 can be replaced by its reflection coefficient  $\Gamma$  in order to simplify the analysis.

We know that:

$$b_3 = \frac{-j}{\sqrt{2}} a \text{ and } a_3 = \frac{-j}{\sqrt{2}} a \Gamma_a \quad (4.5.4)$$

$$b_2 = \frac{-j}{\sqrt{2}} a \text{ and } a_2 = \frac{-j}{\sqrt{2}} a \Gamma_b \quad (4.5.5)$$

Finally:

$$b_1 = -\frac{1}{\sqrt{2}} a_3 - j \frac{1}{\sqrt{2}} a_2 \quad (4.5.6)$$

Rearranging Eq. 4.5.4, Eq. 4.5.5, and Eq. 4.5.6 we obtain:

$$\begin{aligned} b_1 &= -\frac{1}{\sqrt{2}} \left( -\frac{j}{\sqrt{2}} a \Gamma_a \right) - j \frac{1}{\sqrt{2}} \left( -\frac{1}{\sqrt{2}} a \Gamma_b \right) \\ b_1 &= \frac{j}{2} a \Gamma_a + \frac{j}{2} a \Gamma_b, \text{ therefore,} \\ b_1 &= j \frac{1}{2} a (\Gamma_a + \Gamma_b) \end{aligned} \quad (4.5.7)$$

To calculate the gain:

$$G = \frac{b_1}{a} = j \frac{1}{2} (\Gamma_a + \Gamma_b) \quad (4.5.8)$$

It is clear that  $\Gamma_a \equiv \Gamma_b > 1$  to have a perfect power combination. Under real conditions  $\Gamma_a \neq \Gamma_b$  therefore, the output will be a signal with more than one resonant frequency, one close to each other, due to the interaction between oscillators. To minimize this effect, the hybrid coupler should be designed in a way to obtain the best possible isolation at ports 2 and 3.

### 4.5.3 SIW Hybrid combiner design and simulations results

Let us remember that the aim of this project is to design a power source using SIW technology. Cassivi in [5] proved that it is possible to build a  $90^\circ$  Hybrid combiner using SIW. As explained in Chapter 1, building a SIW Hybrid combiner requires constructing a Hybrid combiner using waveguide and, after meeting the design specifications for our particular frequency, replacing the waveguide metallic walls for vias to obtain the SIW Hybrid combiner. Since a  $90^\circ$  phase shift is needed for the power combiner, as explained in Section 4.5.1, a  $\lambda/4$  SIW line was added to port 3 to meet the phase requirement, as shown in Figure 4.22.

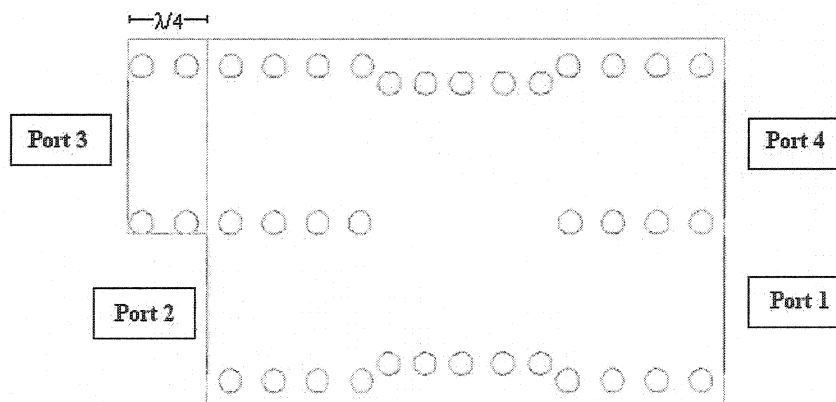


Figure 4-22: SIW Hybrid power combiner

Having performed the S-parameters simulation using HFSS, it is possible to observe an insertion loss of -22 dB at 24 GHz, and a coupling factor of  $S_{12} = -3$  dB and  $S_{13} = -3.11$  dB. Furthermore, the phase difference of port 2 and 3 in relation to port 4 ( $\angle S_{42}, \angle S_{43}$ ) is  $0^\circ$ . The phase difference of port 2 and port 3 in relation to port 1 ( $\angle S_{12}, \angle S_{13}$ ) is  $180^\circ$ , which means that the signals arriving to port 4 are added while the signals arriving to port 1 are subtracted due to the phase mismatch.

Figure 4-23 shows the simulations results.

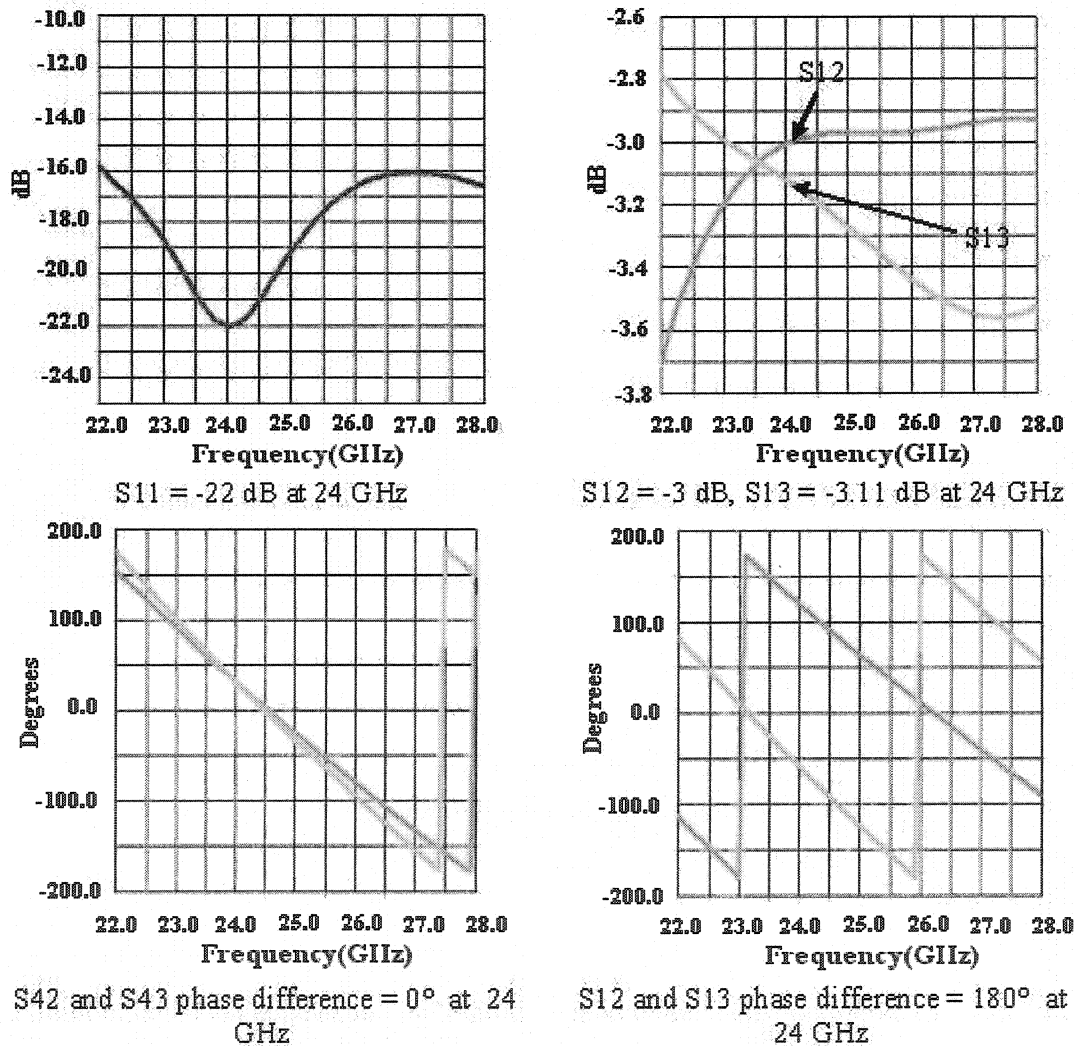


Figure 4-23: SIW Hybrid combiner S parameters simulations results

#### 4.5.4 SIW Hybrid combiner measured results

Figure 4-24 shows a picture of the SIW hybrid power combiner built to measure the S parameters and confirm the simulations.

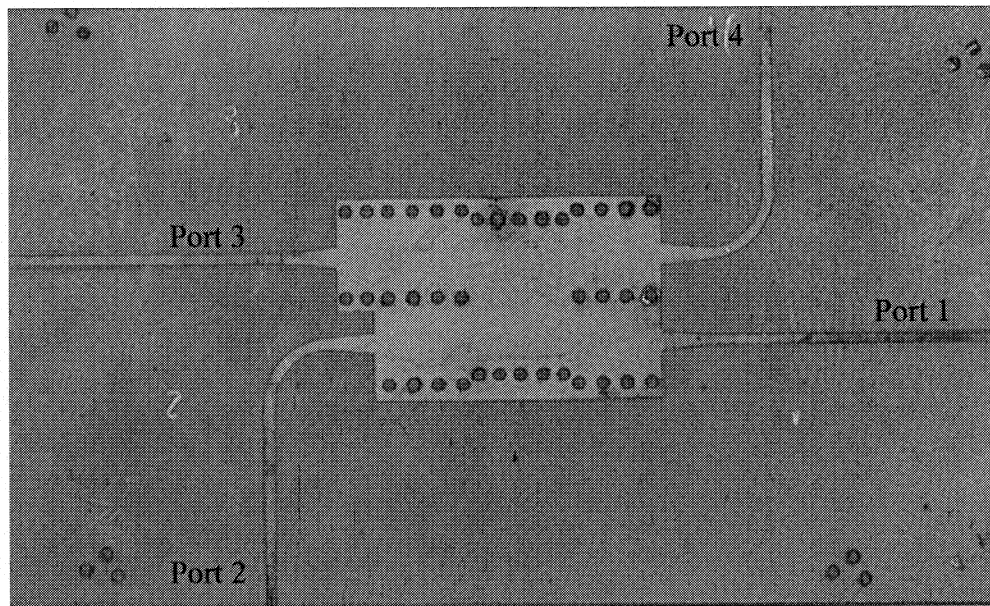


Figure 4-24: SIW Hybrid combiner.

Figure 4-25, shows that the isolation between ports 2 and 3  $S_{23}$  is -20 dB at 24 GHz simulated and -15 dB measured. This suggests that there will be no coupling between the oscillators connected to ports 2 and 3.

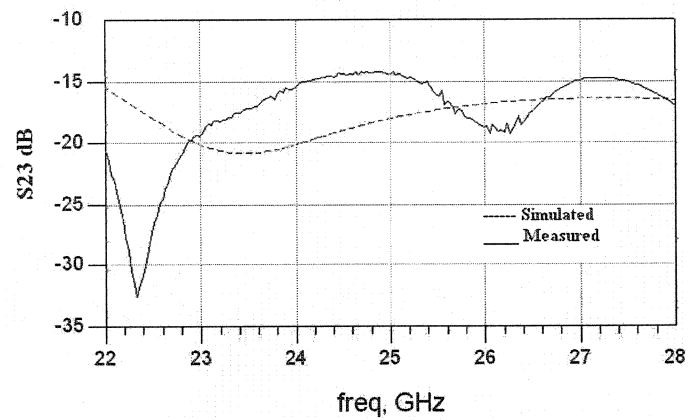


Figure 4-25: SIW Hybrid combiner isolation at ports 2 and 3

Having performed an S-parameters measurements, an insertion loss of -26 dB can be observed at 24 GHz, as well as a coupling factor of  $S_{12} = -3.5$  dB and  $S_{13} = -3.11$  dB. The phase difference of port 2 and 3 in relation to port 4 is  $0^\circ$ , and the phase difference of port 2 and port 3 in relation to port 1 is  $165^\circ$ .

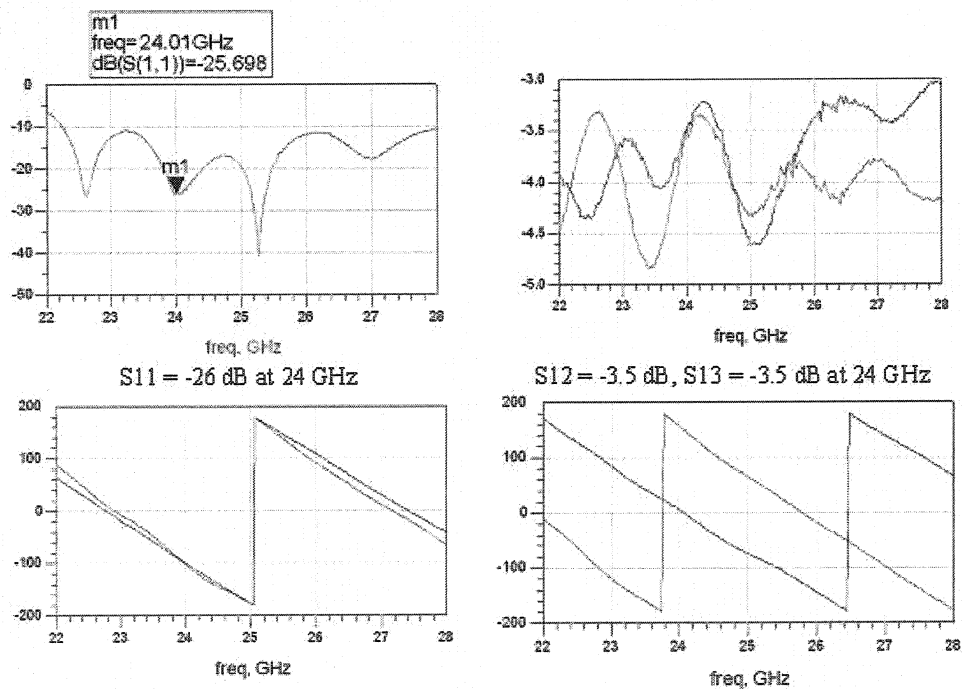


Figure 4-26: SIW Hybrid combiner measurements

Measurements displayed in Figure 4-26 are consistent with the simulations results shown in Figure 4-23.

#### 4.5.5 Power source using the SIW Hybrid combiner

Figure 4-27 shows the power source designed on the base of the measured results of the Hybrid combiner. Since the Wilkinson divider used in the T-junction power combiner to split the injection locking signal to the oscillators is not longer necessary, such part was eliminated from the circuit.

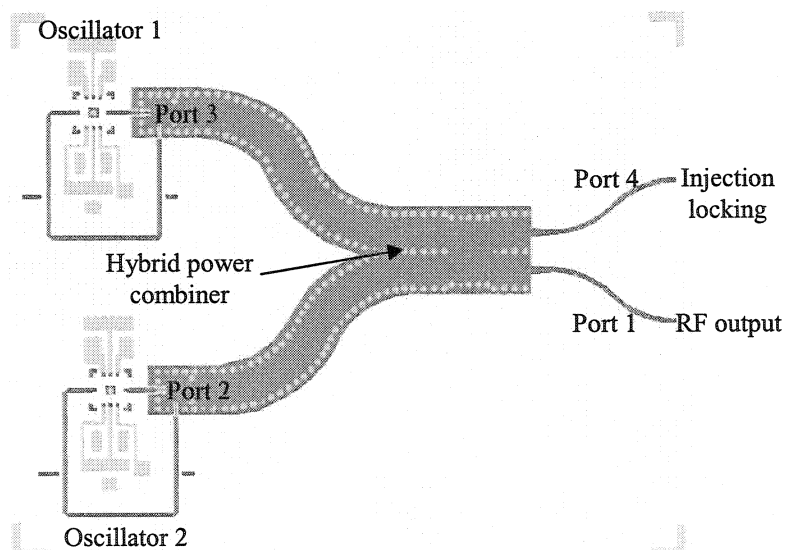
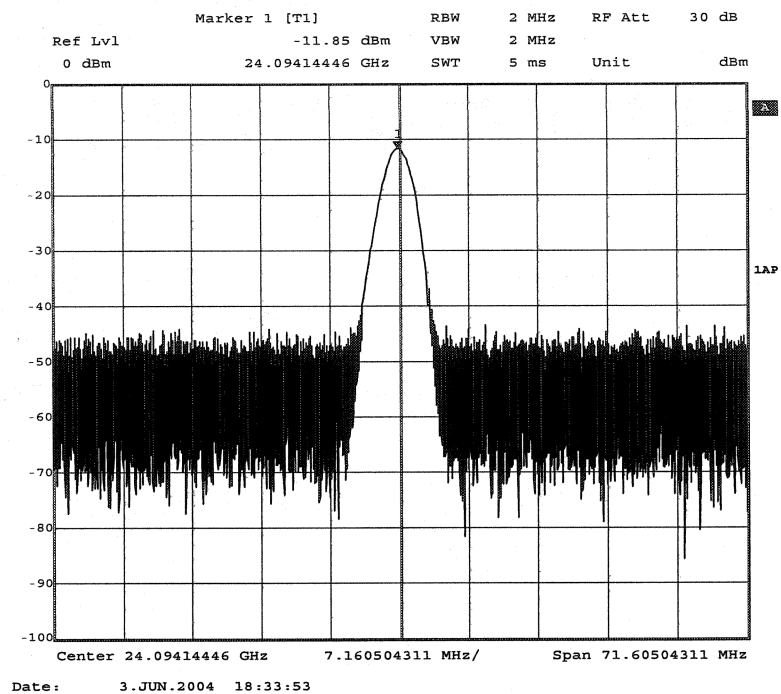


Figure 4-27: Power source using the SIW Hybrid power combiner

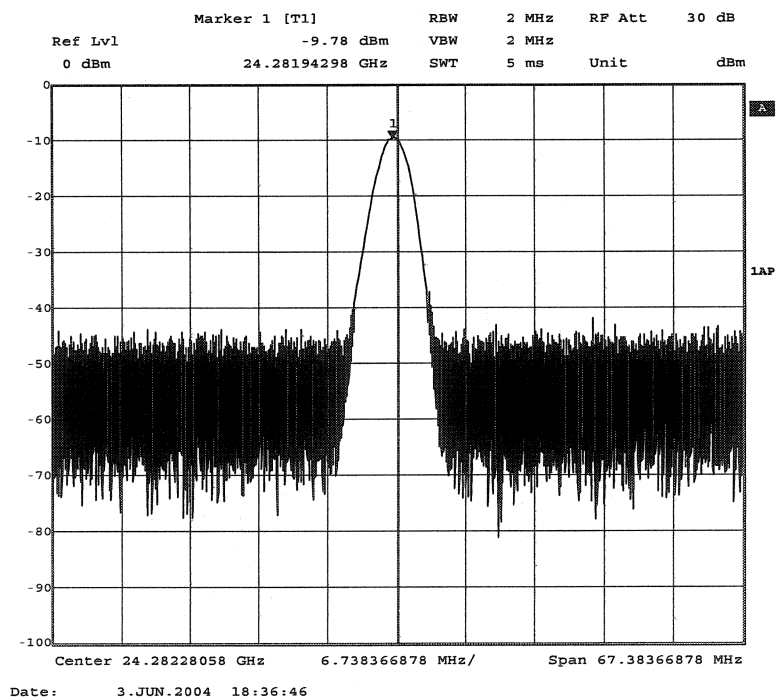
#### 4.5.6 Measurements results

Using the same setup and equipment used in the T-junction power source, measurements on the Hybrid power source were taken to conduct performance comparison under the same environmental conditions.





a)  $f_0=24.09\text{GHz}$



b)  $f_0=24.26\text{GHz}$

Figure 4-28: Resonant frequency: a) Oscillator 1, b) Oscillator

Figure 4-28 shows the frequency response of each oscillator when the other one is not polarized. Even though there is a frequency difference of 200 MHz due to fabrication errors, the performance of the Hybrid power source is not affected as can be seen in Figure 4-29, where a 3dB RF output power combination is obtained. The source is operating without injection locking, terminated on port 4 with a  $50\Omega$  load. The output power is 15.7 dBm at 24.28 GHz

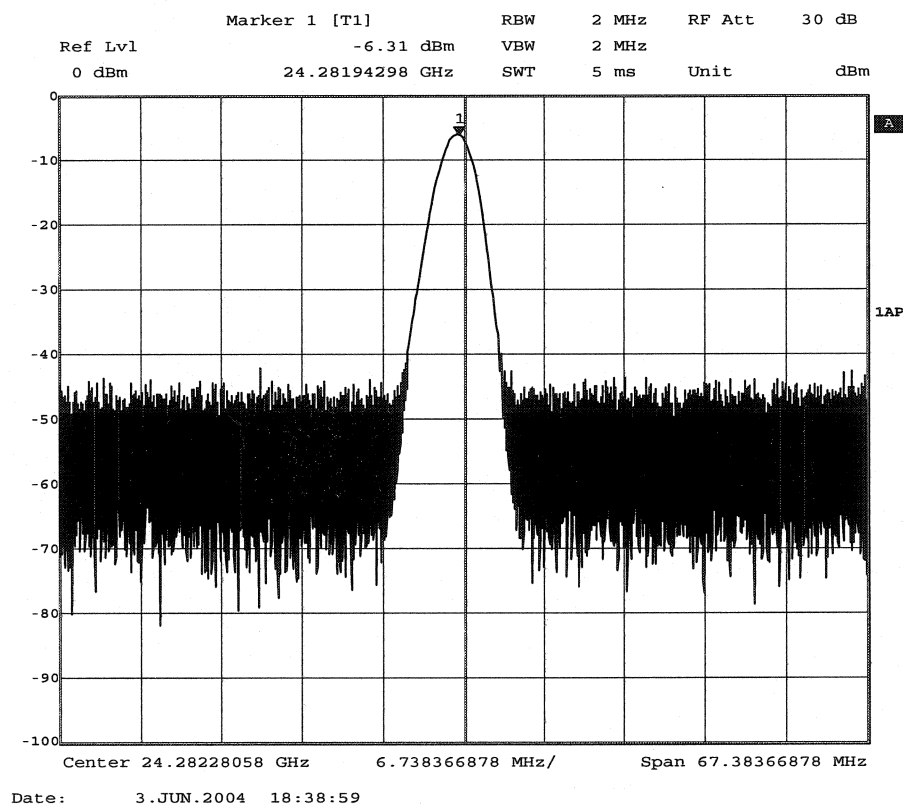


Figure 4-29: Hybrid power source without injection locking

To confirm the phase cancellation at port 4 due to a  $90^\circ$  phase mismatch added on port 3, the  $50\Omega$  load has been connected to port 1 and the RF output was connected to port 4.

Figure 4-30 shows how the RF oscillator signals are cancelled out at port 4, as expected. A RF output of -1.32 dB instead of 15.7 dB was obtained. The amplitude measurements take into account the -20.5 dB attenuator and the -1.53 dB cable loss.

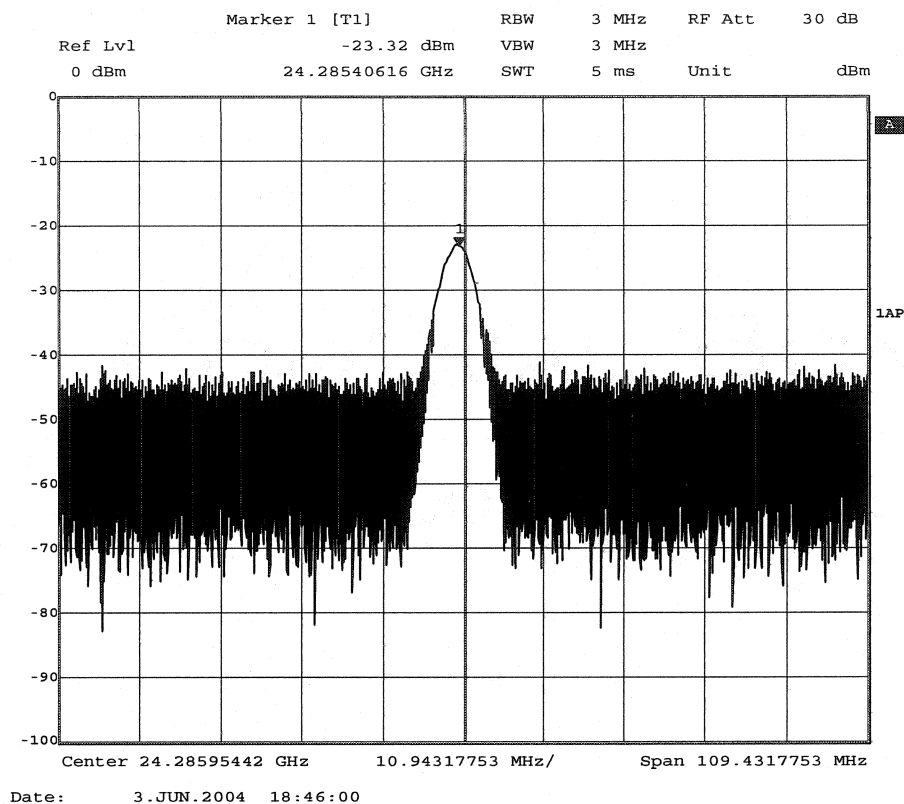


Figure 4-30: Signal cancellation at port 4.

The phase noise measurement without injection locking has a level of -86.71 dBc/Hz at 107.6 Hz away from the carrier. This suggests an improvement if compared with the 48.18 dBc/Hz obtained using the T-junction power source. Phase noise results are presented in Figure 4-31.

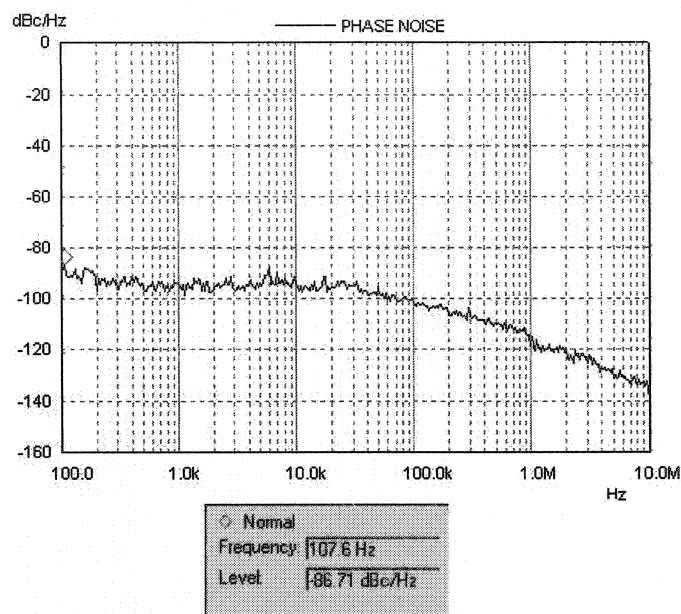


Figure 4-31: Phase noise measurement without injection locking

Figure 4-32 indicates that when the injection locking signal is applied to port 4, the phase noise measurements are very close to those obtained without injection locking.

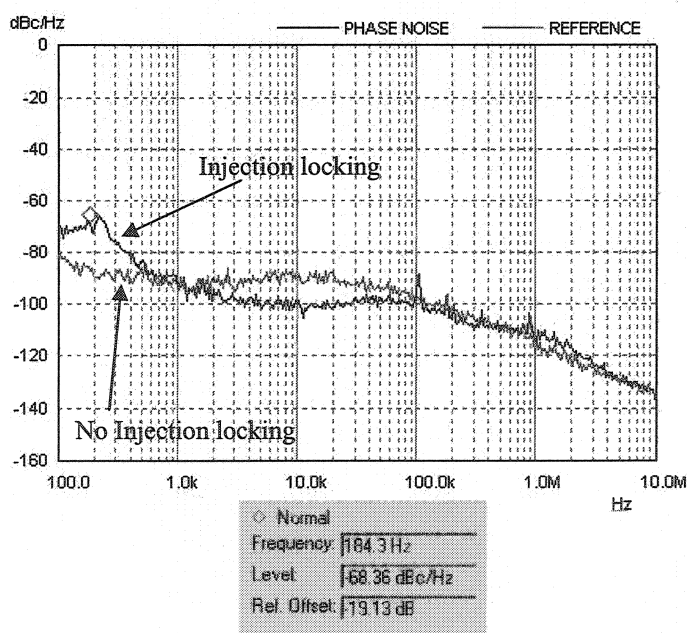


Figure 4-32: Phase noise measurement comparison with and without injection locking

Temperature performance was measured using the same setup of Section 4.3.3.

Thermocouple	Chamber Temperature	I dd mA		Freq(Ghz)	Amp(dBm)
		Osc1	Osc2		
-32.0°C	-30°C	301	321	24.30055	-6.7
-20.8°C	-20°C	295	321	24.29943	-6.8
-10.0°C	-10°C	290	321	24.29755	-6.5
-2.6 °C	0 °C	286	321	24.29542	-6.5
11.1°C	10°C	279	321	24.29098	-6.5
25.0°C	20°C	267	318	24.28369	-6.2
30.0°C	30°C	264	321	24.28155	-7.43
40.0°C	40°C	258	321	24.28108	-6.97
50.0°C	50°C	250	316	24.28079	-7.02

Table 4-2: Hybrid power source temperature performance.

To calculate temperature stability in ppm/°C equation 3.4.1 was used along with data from Table 4-2. The 9.97 ppm/°C result is very close to the 6.54 ppm/°C result obtained with the T-junction power combiner. It can then be concluded that in terms of temperature performance the Hybrid power source is also very stable compared with commercial specifications

Figure 4-33 presents the frequency variation with temperature on the Hybrid power combiner.

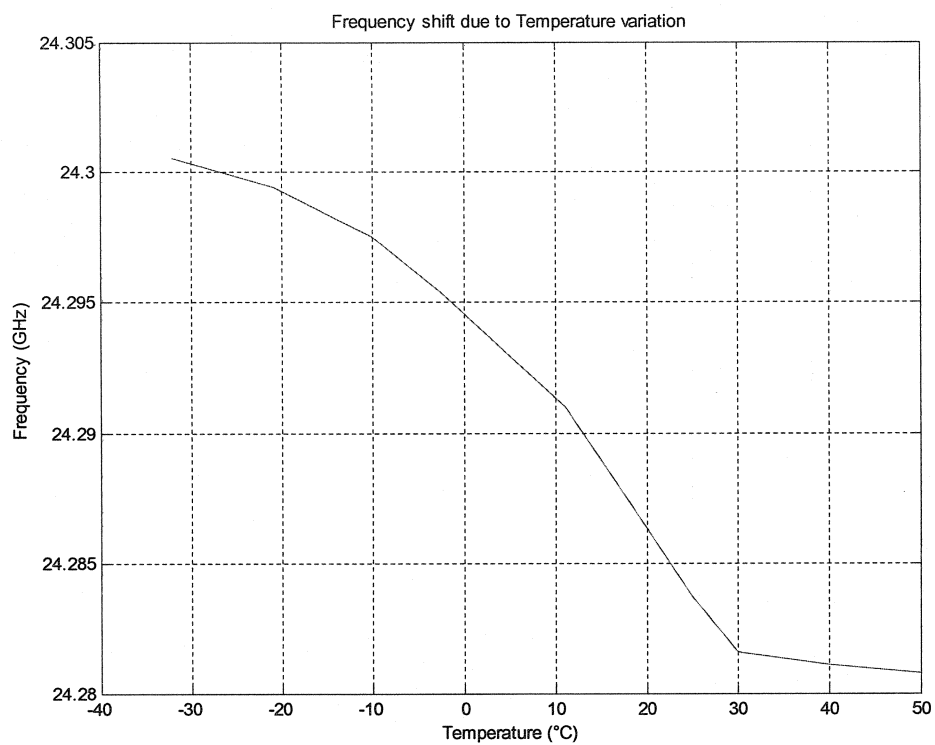


Figure 4-33: Frequency variation with temperature in the Hybrid power combiner

## CONCLUSION

The SIW technology has been proved very promising in the design, construction and integration of RF and microwave sources. This scheme can reduce problems due to transitions between planar and non-planar structures such as loss and manufacturing cost as well as thermal problems.

This project has presented the basic concepts that support the Substrate Integrated Waveguide SIW circuits, focused mainly on resonant cavity design, oscillator design, and power combiner design. A method to optimize the coupling factor between the microstrip line and the cavity was explained, using a probe in which the values of the length and the width are degrees of freedom to optimize the impedance matching. A single cavity and a dual cavity were designed to compare their performance; it was concluded that, the single cavity offers more stability and simplicity to the circuit, therefore, being more suitable for the oscillator design; the improvement and results for the dual cavity do not justify the difficulty and the time invested in the design. A measured Q factor of 2300 was achieved in the single cavity, which reflects the oscillator stability.

Several temperature and phase noise measurement allow to conclude that our oscillator presents a phase noise level as low as -70.16 dBc/Hz at 171.9 Hz from the carrier. The temperature stability is as low as 6 ppm/°C, which falls within the market's standards where a temperature stability of 20 ppm/°C is excellent for commercial applications.

To combine the out power of two or more oscillators a T-junction was used as a vehicle to combine the power. Based on the measured results the performance of the T-junction power combiner was good from a general point of view. A 2.9 dB power combination at the resonant frequency was achieved as expected. The fact that the power combiner inputs present an isolation factor as low as -6.7 dB, suggests a coupling between

oscillators; if the oscillator's resonant frequency and phase are identical the oscillator's coupling will improve the overall performance, and the need for the injection locking scheme will be reduced; but if their phase and resonant frequency are different, one oscillator will lead the other, forcing the second one to oscillate at the first oscillator's frequency; this dynamic is known as inter-injection locking. In this case to achieve a good performance it is imperative to use an injection locking signal.

A good isolation between oscillators in power combiner will solve the oscillator's coupling problem. A 90° Hybrid coupler was used to improve the isolation factor. A -15 dB isolation between ports 2 and 3 was achieved, if compared with -6.5 dB obtained with the T-junction power combiner a 9 dB improvement is obtained.

When the power source is built using the 90° Hybrid coupler as a combiner, a phase noise improvement of 40 dBc/Hz is obtained. The injection locking bandwidth is increased from 4 MHz in the T-junction power source to 8 MHz using the 90° Hybrid power source. Another advantage is the simplification of the circuit, since the Wilkinson divider used to inject the locking signal was eliminated.

This project faced two main challenges: one was to achieve a high Q cavity resonator at the design frequency. The conclusion was that a single cavity was a reliable method to obtain a very stable oscillator with a high Q factor.

A second challenge was a fabrication constrain. Having to place and solder the vias manually to build the SIW cavity is time consuming and could lead to frequency shifting; if a single via is not properly soldered, the cavity's resonant frequency will change. The possible solution of plating the vias by a chemistry process (electrolytically), did not offer the needed results since the circuit's area to be plated is too big for the resources available at the laboratory. Therefore, it was decided to build the circuit carefully using the manual process.



This project included the design of a power source for two oscillators that is flexible and can be extended to several devices by cascading as many  $90^\circ$  hybrid combiners as needed.

It is worth noting that the use of a smaller commercial amplifier will considerably reduce the size of the circuit. It is also possible to obtain combinations of power at different frequencies by adjusting the cavity dimensions and the feedback loop.

## REFERENCES

- [1] Adler, R., "Study of Locking Phenomena in Oscillators," Proc IRE, Vol. 34, No. 6, Jun. 1946, pp. 351-357.
- [2] Boudouris, G. 1971 Cavités Électromagnétiques.
- [3] Y. Cassivi and K. Wu. "Low-cost Microwave Oscillator using SIW cavity", Submitted to Microwave and wireless components letters, 2002.
- [4] Y. Cassivi, L. Perregrini, K. Wu et al., "Dispersion Characteristics of SIW" accepted for publication, IEEE Microwave and Wireless Components Letters, 2002.
- [5] Y. Cassivi, D. Deslandes, K. Wu "Substrate Integrated waveguide Directional Couplers", Asia-Pacific Microwave Conference, 2002.
- [6] Chang, k., and C. Sun, "Millimeter-Wave Power Combining" IEEE Trans, Microwave Theory Tech., Vol. MTT-31, No. 2, pp. 91-107, Feb. 1983.
- [7] R. Collin. 1992. Foundations for Microwave Engineering. 924 p.
- [8] D. Deslandes and K. Wu, "Integrated Microstrip and Rectangular Waveguide in Planar form", IEEE Microwave and wireless Components Letters, Vol. 11 Feb. 2001, pp. 68-70.
- [9] D. Deslandes and K. Wu "Design considerations and performance Analysis of Substrate Integrated Waveguide components" European Microwave Conference, 23-27 Sept. 2002, pp.881-884.

- [10] D. Deslandes and K. Wu, "Single-Substrate Integration Technique of Planar Circuits and Waveguide Filters" IEEE Trans. On Microwave Theory and Techniques, Vol. 51, No. 2, Feb. 2003.
- [11] Esdale, D., and H. Howes, "A Reflection Coefficient Approach to the design of One-Port Negative Impedance Oscillators," IEEE Trans. On MTT, Vol MTT-29 Aug. 1981, pp. 770-776.
- [12] S. Germain, D. Deslandes and K. Wu, "Development of substrate integrated waveguide power dividers". CCECE 2003 – CCGEI 2003, Montréal, May. 2003.
- [13] Gonzales, G. 1997. Microwave Transistor Amplifiers Analysis and Design 506 p.
- [14] J. Hirokawa, K. Sakurai, M. Ando and N. Goto, "An analysis of a waveguide T junction with an inductive post," IEEE Transactions on Microwave Theory and Techniques, vol. 39, no. 3, pp. 563-566, Mar. 1991.
- [15] Keyton, N., "A Lumped Circuit Study of Basic Oscillator Behavior," BSTJ, Vol.49, February 1970, pp.255-272.
- [16] Kurokawa, S., "Some Basic Characteristics of Broadband Negative Resistance Oscillators Circuits." BSJT, Vol. 48, Jul. 1969, pp.1937-1955.
- [17] K. Kurokawa, and F. Magalhaes "An X-band 10-Watt Multiple-IMPATT Oscillator"Proc. IEEE, vol. 59, No 1, pp 102-103, Oct. 1971.
- [18] Kurokawa, K., "Injection Locking for Microwave Solid-State Oscillators," Proc. IEEE, Vol. 61, No. 10, Oct. 1973, pp.1383-1410.

- [19] N. Marcuvitz, Waveguide Handbook, 2nd ed., London: Peter Peregrinus Ltd., and New York: McGraw-Hill, 1986, p. 63.
- [20] G. Matthaei L. Young and E.M.T. Jones 1980 Microwave filters, Impedance-matching networks, and coupling structures 1096p.
- [21] B. Meskoob and S. Prasad, "Loop-gain measurement and feedback oscillator design," IEEE Microwave Guided Wave Lett., vol. 2, no. 9, pp. 375–377, Sept. 1992.
- [22] J. R. Nevarez and G. J. Herokowitz, "Output power and loss analysis of 2 Injection-locked oscillator combined through an Ideal and symmetric hybrid combiner," IEEE Trans. Microwave Theory Tech. Vol. MTT-17, pp. 2-10, Jan. 1969.
- [23] A. J. Pilote, K. A. Leahy, B. A. Flanik, K. A. Zaki, "Waveguide filters Having a Layered Dielectric Structure," U.A. Patent, No. 5 382 931, Jan 17 1995.
- [24] D. Pozar 1998, Microwave Engineering. 716 p.
- [25] Pouysugur, M., G. Graffeuil, J. Sauterau, and J. Fortera, "Comparative Study of Phase Noise in HEMT and MESTFET Microwave Oscillators," IEEE Microwave Symp. 1988, Vol. 2, pp. 557-560.
- [26] Ramo, Whinnery, and Duzer 1967 Fields and Waves in Communication Electronics 596p.
- [27] Slater, J.C. 1950. Microwave Electronic 405p.
- [28] Tsironis, C., "High Stability Dielectric Resonator FET Oscillator," IEEE Trans. MTT, Vol. MTT-33, Apr. 1985, pp. 310-314.

- [29] H. Uchimura, T. Takenoshita, M. Fuji, "development of a laminated Waveguide", IEEE Trans. Microwave Theory and Techniques, Vol. 46. Dec. 1998, pp. 2438-2443.
- [30] Van der Pol, B., "The Nonlinear Theory of Electrical Oscillators," Proc IRE., Vol 22 Sep 1934, pp. 1051-1086.
- [31] K. Wu, D. Deslandes, Y. Cassivi, "The substrate integrated circuits - a new concept for high-frequency electronics and optoelectronics," TELSIKS'03, pp. P-III – P-X, Nis, Yugoslavia, Oct. 1-3, 2003.
- [32] Product Note 8510-8A "Applying the HP 8510 TRL calibration for non-coaxial measurements" HP.
- [33] HFSS, version 5.3, Agilent.